Electrokinetic flow : characterization, control and application in microfluidic systems

Yan, Deguang

2007

Yan, D. G. (2007). Electrokinetic flow : characterization, control and application in microfluidic systems. Doctoral thesis, Nanyang Technological University, Singapore.

https://hdl.handle.net/10356/5282

https://doi.org/10.32657/10356/5282

Nanyang Technological University

ELECTROKINETIC FLOW: CHARACTERIZATION, CONTROL, AND APPLICATION IN MICROFLUIDIC SYSTEMS

YAN DEGUANG

SCHOOL OF MECHANICAL & AEROSPACE ENGINEERING

NANYANG TECHNOLOGICAL UNIVERSITY

2007

Electrokinetic Flow: Characterization, Control, and Application in Microfluidic Systems

Yan Deguang

School of Mechanical & Aerospace Engineering

A thesis submitted to the Nanyang Technological University in fulfillment of the requirement for the degree of Doctor of Philosophy

2007

Abstract

Advanced microfluidic devices can perform complete biochemical analysis in a single fabricated chip. One of the crucial issues in developing these microfluidic devices is to transport reagents and electrolytes to specified destinations without external intervention. The electrokinetic (EK) pumping can provide a kinetic source to route the liquid through microchannel networks. The EK pumping has numerous advantages including ease of fabrication, no need for moving parts, high reliability, and no noise, so that it has been extensively implemented in many microfluidic systems. The present study focuses on the characterization, control and manipulation of electrokinetic flows in microchannel network in order to optimally design and effectively control microfluidic devices. Specifically, due to strong relevance to the development of novel microfluidic devices such as millisecond capillary electrophoretic separation systems, AC pumps, advective chaotic micromixers *etc.*, the time-dependent and frequency-dependent electroosmotic flows (EOF) are thoroughly investigated.

Having advantages of obtaining the whole-field information of fluid flow in microfluidic channels, the micro-PIV technique is used to characterize the EOF in microfluidic channels. Since the tracer particles used in micro-PIV measurements and channel wall are charged in liquids, electrokinetic mobilities and zeta potentials of the tracer particles and the channel surfaces are crucial to the design, control, and characterization of microfluidic devices. A new method, which combines the electrokinetic flow theory and the micro-PIV experiment, is developed to simultaneously determine the zeta potentials of both the channel wall and the tracer particles. With the known zeta potentials, the EOF velocity field can be obtained by subtracting the electrophoretic effects on the tracer particles, and hence the theoretical model can be validated using the micro-PIV technique.

A micro-PIV based phase locking technique is developed to measure the transient electrokinetic flow in microchannels. With the transient micro-PIV technique, a method is further proposed to decouple the particle electrophoretic velocity from the micro-PIV measured velocity and to determine the zeta potential of the channel wall.

Then for the first time the time evolution of the full-field, electroosmotic velocity distributions in both open- and closed-end rectangular microchannels is obtained. Using the slip velocity approach and the measured channel zeta potential, theoretical predictions of the transient electroosmotic flow in the open- and closed-end microchannels are obtained, and they are found in accordance with the experimental results.

Using the micro-PIV technique together with appropriate synchronization design, the frequency-dependent EOFs are measured in both open-end and closed-end rectangular microchannels. The theoretical modeling of the frequency-dependent EOF is revisited by using the Laplace transform based Frequency Domain Analysis. A comparison of the experimental results with the simulation data shows reasonable agreement.

As the AC-driven EOF can be modulated by adjusting amplitude and frequency of the electric field, the periodically-oscillating feature of the AC EOF is utilized for the development of electrokinetic micromixers. Theoretical modeling of the mixing process in electrokinetic T-mixers is presented, and the model is solved numerically. PDMS based T-mixers are fabricated using the Softlithography method. Thorough experiments are carried out to examine the performance of the mixing under the effects of the frequency and amplitude of the external AC electric field, and the geometry of the microchannels. The micro-PIV technique is employed to measure the EOF velocity field in the mixing process. Based on the experimental data and simulation results, it is found that the use of AC electric field together with a DC offset has limited improvement in mixing quality, while the design of patterned structure in microchannels can enhance the mixing effectively. In addition, a novel design of the electrokinetic micromixer using fabricated electrodes is proposed, in which the transverse flow is induced by the metal surface effect. The numerical simulations show that the new design significantly improves the mixing performance.

Acknowledgements

It is a great pleasure to express my sincere gratitude of the support and help of numerous people during my PhD study.

First and foremost, I owe it to my supervisor, Dr Yang Chun, Charles, who introduced me to microfluidics and has been a supportive supervisor and a great teacher. It is he who directed me with insightful guidance, helped me build up my confidence, and encouraged me to overcome difficulties. Other than that, I also appreciated very much the care extended to my daily lives by Dr Yang and his wife, Mdm Xu Li.

The achievement of this work is also owed to my co-supervisor Dr Huang Xiaoyang and Dr Nguyen Nam-Trung. It is their continuous support and deep concern that helped me overcome one difficulty after another in my research work.

This work would not have been completed without the enthusiastic support of my fellow students and friends from past and present. Particularly, my sincere gratitude should be extended to Dr Tang Gongyue, Dr Xing Xiuqing, Dr Kang Yuejun, Dr Jin Liwen, Dr Zhang Junmei, Dr Yap Yit Fatt, Mr Wang Cheng, Mr Gan Hiong Yap, Mr Marcos, Mr Gao Yandong, Mr Sohel Murshed, Mrs Zhang Yali, and the final year project student Miss Huang Jintao. Over the years, they have provided advice, continuous assistance, and friendship.

I would also like to thank the technician of Thermal and Fluids Lab, Mr Yuan Kee Hock for offering kind help to my research work, and Dr Wang Weilong for his technical support in my project.

Three-years scholarship from Nanyang Technological University is greatly acknowledged.

Finally, I would like to thank my father, mother, sister and sister-in-law for their endless love and support. None of this would be possible without their continuous encouragement and deep concern. My very special thanks go to my wife, Mrs An Ping, for her love, support, and confidence on me.

Contents

Nomenclature

a	radii of tracer particles or cylindrical capillary [m]
c	concentration of sample species [M]
C	characteristic parameter for finite reservoir size effect on EOF [s^{-1}]
D	Diffusion coefficient [m^2 s^{-1}]
D_h	channel's hydraulic diameter [m]
$\boldsymbol{E}$	externally applied electric field vector [V m^{-1}]
e_0	elementary charge, 1.602×10^{-19} [C]
$\boldsymbol{F}$	force vector [N]
f	frequency of the applied sinusoidally alternating electric field [Hz]
g	acceleration of gravity [m s^{-2}]
I	Intensity of image
j	unit imaginary number ($\sqrt{-1}$)
k_b	Boltzmann constant, 1.381×10^{-23} [J K^{-1}]
l, L	length of the microchannel [m]
$\mathcal{L}$	operator of Laplace transformation
n_0	ionic number concentration in the bulk fluid [m^{-3}]
$\mathcal{O}$	order of magnitude
p	pressure [Pa]
P_0	characteristic pressure or reference pressure [Pa]
Pe	Peclet number
q	volumetric flow rate [m^3 s^{-1}]
Q	total volumetric net flow quantity [m^3]

r	radial coordinate in cylindrical coordinate system
R	radius of cylindrical reservoir [m]
Re	Reynolds number
St	Strouhal number
s	variable in Laplace space
t	time [s]
T	absolute temperature [K]
u	velocity z-component in Cartesian coordinate system [m s^{-1}]
u_s	slip velocity [m s^{-1}]
w, h	width and height of a rectangular channel [m]
W	width of the mixing channel downstream from T-junction [m]
U	reference velocity [m s^{-1}]
$\boldsymbol{V}$	velocity vector in Navier-Stokes equation [m s^{-1}]
x, y, z	coordinate in Cartesian coordinate system [m]
X, Y, Z	dimensionless coordinate in Cartesian coordinate system

Greek Symbols

ε	permittivity of the electrolyte solution [C V^{-1} m^{-1}]
ε_0	permittivity of vacuum, 8.854×10^{-12} [C V^{-1} m^{-1}]
ε_r	dielectric constant of the electrolyte
ζ	zeta potential [V]
Φ	electric field potential [V]
κ	Debye-Hückel parameter [m^{-1}]
λ_D	Debye length [m]
δ_s	Stokes penetration depth [m]
μ	dynamic viscosity [N s m^{-2}];
	electroosmotic or electrophoretic mobility [m^2 V^{-1} s^{-1}]
ν	kinematic viscosity [m^2 s^{-1}]

ρ	mass density [kg m^{-3}]
ρ_e	net charge density [C m^{-3}]
ω	angle frequency of the sinusoidally alternating electric field [rad s^{-1}]
ψ	phase angle [rad]
τ	dummy time variable
σ	mixing efficiency

Subscripts

e	with reference to electrical charge;
	with reference to electrostatic body force
eo	with reference to electroosmosis
ep	with reference to electrophoresis
mob	with reference to electroosmotic or electrophoretic mobility
p	with reference to particle;
	with reference to pressure-driven flow
w	with reference to channel wall

Superscripts

$-$	non-dimensionalized or normalized parameter
$\wedge$	Laplace transform of a term

Abbreviations

AC	Alternating Current
DC	Direct Current
DI	Deionized
EDL	Electric Double Layer

EK	Electrokinetic
EOF	Electroosmotic Flow
EP	Electrophoresis
PIV	Particle Image Velocimetry
PDMS	Polydimethylsiloxane
PMMA	Polymethylmethacrylate

List of Figures

List of Tables

Chapter 1

Introduction

1.1 Background and Motivation

During the past two decades, the rapid development in micro fabrication technologies has enabled a variety of microfluidic systems consisting of ducts, valves, pumps, and mixers to be utilized effectively for medical, pharmaceutical, defense, and environmental monitoring applications. Moreover, the advent of microfabricated chemical analysis systems has led to a growing interest in microfabricated fluidic systems with characteristic scales in the range of microns to one millimeters, which are called *integrated microfluidic devices* (Erickson and Li, 2004). For example, the device shown in Figure 1.1 is a microfluidic cytological tool, which is used for cell counting and separation. It consists of an integrated microfabricated chip with a PDMS cover and molded fluidic connections.

Microfluidics refers to devices and methods for controlling and manipulating fluid flows with length scales less than a millimeter. Several reviews on microfluidics are provided by Gravesen *et al.* (1993), Ho *et al.* (1998), Stone *et al.* (2004), and Whitesides (2006). Microfluidic devices have found their wide applications in many scientific and industrial contexts, for example, in the area of micro total analysis systems (μTAS), also called "lab on a chip". Some detailed reviews on μTAS have been given by Reyes *et al.* (2002), Auroux *et al.* (2002) and Vilkner *et al.* (2004).

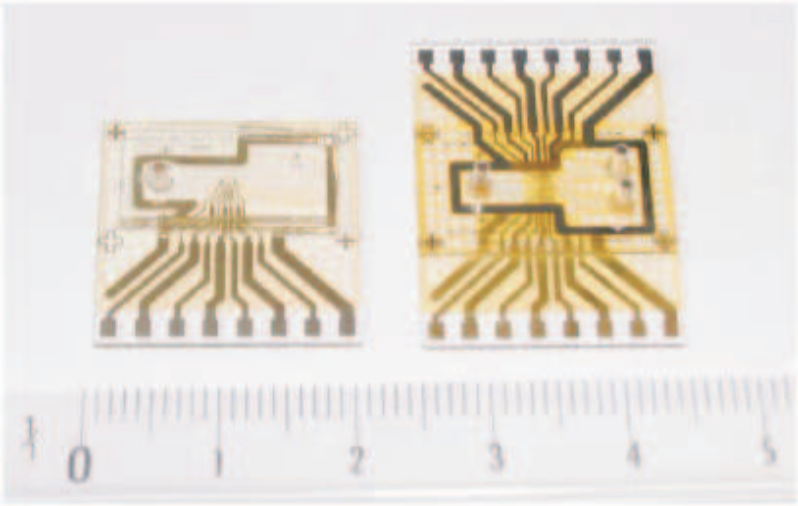

Figure 1.1 Microfluidic cytological tool (After Erickson and Li, 2004).

Most microfluidic systems rely on two modes of fluid transport: pressure-driven and electrokinetically-driven flows. Traditionally, flow is often driven by pressure. In micro systems, some parts like micro valves and micro pumps with moving components are difficult to design and fabricate, and they are prone to mechanical failure due to fatigue and fabrication defects.

Alternatively, fluid motion in the microfluidic systems can be achieved by using electroosmotic flow, which enjoys several advantages over pressure-driven flows: producing a nearly uniform "plug" profile, which results in reduced sample species dispersion as compared to the parabolic velocity profile associated with pressure-driven flows; controlling fluid pumping and valving without moving parts; and being capable of wide variety of processes including mixing, molecular separation, and generation of pressure work. Thus electrokinetic flow is often utilized in microfluidic devices to transport buffer solutions and to manipulate sample solutes. Examples include microfluidic pumping, flow control, mixing and reacting reagents, injecting or dispensing samples, capillary electrophoresis based chemical separations, chromatograph, *etc.* Li (2004) systematically reviewed electrokinetic microfluidics processes for lab-on-a-chip applications. A recent review by Chang (2006) demonstrates the viability to use electrokinetics in microfluidic platform for miniaturizing diagnostic kits.

The technological demands on microfluidic systems require a profound understand-

ing of the micro-scale thermal/fluid transport phenomena, which differ from their larger-scale counterparts mainly due to the size and the surface effects. Meanwhile, as on-chip electroosmotic and electrophoretic systems grow in complexity, the need for a detailed understanding of the underlying flow physics of such systems becomes ever more critical. Characterization, control, and manipulation of these flows are therefore needed to facilitate the development of microfabricated fluidic systems.

1.2 Objectives

Fundamental understanding of the behavior of fluid flow is essential to successful design and optimal control of microfluidic devices. Despite the difficulty arising from the microscale and surface effects, numerous techniques have been developed to diagnose the velocity profiles and probe flow characteristics in microfluidic channels. Micron-resolution particle image velocimetry (micro-PIV) is a powerful tool for such purposes. In this study, the micro-PIV technique is chosen to characterize electrokinetic flow field. Micro-PIV has several advantages over other pointwise measurement techniques. It can probe the whole flow velocity field, and nearly-matured processing algorithm provides improvements in velocity measurement accuracy and resolution. It also should be noted that as micro-PIV technique uses tracer particles that are usually charged in aqueous liquids, the velocity field obtained is a combination of the electrophoretic velocity of the tracer particles which is related to the particle electrophoretic mobility and the electroosmotic flow field which is associated with the zeta potential of the channel wall. To obtain the electroosmotic flow field, the electrophoretic component has to be subtracted from the micro-PIV measured particle velocity so that the electroosmotic flow field can be retrieved.

Exclusively, through the literature survey conducted in this study, most previous studies focus on the velocity field of steady-state electrokinetic flows. No study has been reported on measuring the velocity field of transient electrokinetic flows. This is mainly due to the fact that the time scale for the temporary evolution of elec-

trokinetic flows in microfluidic channels is in the order of milliseconds, which is too rapid for the relatively low frame rates of the state-of-the-art PIV cameras to capture. However, direct visualization of the dynamic electrokinetic flows is of fundamental importance as it provides insight into the underlying mechanisms of the development and stability of electrokinetic flows. Furthermore, study of the dynamic aspects of the electrokinetic flow plays a crucial role in the development of relevant microfluidic technologies. Hence, in the present study, one goal is to characterize the time- and frequency-dependent electroosmotic flows in microchannels.

Because of low Reynolds number laminar flows in microchannel, the mixing process in microfluidic systems is inherently poor. As a result, effective mixing in a microfluidic device poses a great challenge. Fortunately, the electrokinetic phenomena have offered various possible solutions to improve micromixing. The frequency-dependent EOF is a good choice, because its performance can be adjusted by modulating the amplitude and frequency, and its design and fabrication can be realized easily. However, a systematic study on characterization and investigation of electrokinetic micro mixer has never been pursued in the literature. This is partly because that the electrokinetic mixing is a complicated process and affected by numerous factors, such as amplitude, frequency, and geometry, *etc.* Hence, another goal in the present study is to design and fabricate novel electrokinetic micro mixers, and further systematically characterize and investigate their performances.

Hence, the objectives of this thesis can be stated as the following:
(1) To develop a method to decouple the electroosmotic and electrophoretic velocity components of the tracer particles.
(2) To develop a technique to investigate start-up transient electroosmotic flows in microchannels.
(3) To characterize and investigate the time-dependent and frequency-dependent EOF.
(4) To propose effective designs of electrokinetic micromixers and characterize mixing performance.

In summary, the present study focuses on characterization, control and manipu-

lation of electrokinetic flows in microchannels with an intend to provide insight into electrokinetic flow characteristics for the optimum design and process control of microfluidic systems.

1.3 Outline of the Thesis

There are seven chapters in this thesis. Chapter 1 serves as an introduction to the background and motivation of this work. The latest development in microfluidics and the advantages and applications of electrokinetic flows are presented. The objectives of the study are outlined. In the literature review, the current studies on electrokinetic flows and their diagnoses technologies have been discussed and remarked.

Chapter 2 covers the micro-PIV measurements of steady-state electrokinetic flows in straight rectangular open- and closed-end microchannels. Through the measurement under the same water chemistry condition, a method for decoupling the electrophoretic velocity of tracer particles and electroosmotic flow component, and thus for simultaneously determining the zeta potentials of the channel surface and the tracer particles is proposed.

In Chapter 3, a micro-PIV based phase locking technique is developed with an ordinary PIV CCD camera to carry out an experimental study of the transient electrokinetic flow in microchannels by synchronizing different trigger signals for the laser, CCD camera, and in-house designed high-voltage switch. With the transient micro-PIV technique, a method is further proposed to decouple the particle electrophoretic velocity from the micro-PIV measured velocity and to determine the zeta potential of the channel wall. The time evolution of the full-field, electroosmotic velocity distributions in both open- and closed-end rectangular microchannels is obtained. Using the slip velocity approach and the measured channel zeta potential, the theoretical predictions of the transient electroosmotic flow in the open- and closed-end microchannels are obtained.

In Chapter 4, an in-depth assessment of the finite reservoir size effect on electroos-

motic flows is presented theoretically and experimentally. First, an analytical model is given and solved. Based on the analytical model and simulation results, two important times are proposed and the factors that affect the EOF due to the finite-reservoir effects are analyzed. Finally, using micro-PIV technique, the model is validated with experiment.

Chapter 5 presents a theoretical and experimental study of the frequency-dependent electroosmotic flows in open- and closed-end rectangular microchannels. A theoretical approach combining the Laplace transform and the Frequency Domain Analysis is proposed to analyze the frequency-dependent EOF. The proposed theoretical model is verified with micro-PIV based experiment.

In Chapter 6, a systematic study on electrokinetic micromixing using frequency-dependent EOF is conducted. Numerical simulations are performed to analyze the mixing efficiency. PDMS/glass-made microchannels were fabricated using micro fabrication techniques. For experimentally characterizing the mixing quality, Rhodamine B visualization and micro-PIV were employed to quantify the mixing performance and determine the EOF velocity field. In addition, a novel design of electrokinetic micromixer using fabricated electrodes is proposed. From numerical simulations, we show that the proposed novel design effectively improves the mixing performance.

Finally, Chapter 7 summarizes the major results and findings from the present study. The contributions made by this thesis are highlighted and possible future work is outlined briefly.

1.4 The Electric Double Layer and the Electrokinetic Phenomena

For microfluidic electrokinetic systems fabricated from glass or fused silica, silanol groups on the surface deprotonate when in contact with an electrolyte. The extent of deprotonation depends on the local pH and the ion concentration of the solution. Polymer-based microchannels also characteristically acquire a surface charge when in

contact with an electrolyte. An electric double layer (EDL) is formed to balance such surface charges, and EDL consists of a charged solid surface and a liquid region near the surface that supports a net excess of counter-ions. In classical theory, these counter-ions are considered to reside in two regions: the Stern and Gouy-Chapman Diffuse Layers. The immobile counterions adsorbed to and immediately adjacent to the wall form the Stern layer, while the Gouy-Chapman layer comprises the diffuse and mobile counter-ion layer that is set in motion upon the application of an external electric field. The shear plane separates the Stern and Gouy-Chapman layers, and in simple models of the EDL it is the location where the condition of no-slip in fluid motion is enforced. The potential at the shear plane is called the zeta potential, ζ. Zeta potential is an experimentally measurable electrical potential that charcterizes the EDL, and it plays an important role in many applications such as electrokinetic transport of particles (Keh and Anderson, 1985) and capillary electrophoresis (Gaš, 1997; Gaš and Kenndler, 2002). The zeta potential is often measured indirectly using velocity or flow rate measurements. One effective approach to measure zeta potential is the so-called current monitoring method (Huang *et al.*, 1988). Two review papers by Brian and Hasselbrink (2004a and 2004b) present details on the measurement and data of the zeta potential of microfluidic substrates.

A sketch of the electrical potential associated with the EDL is shown in Figure 1.2. The magnitude of the potential decays away from the wall, and the bulk fluid far from the wall is assumed to be neutral. A review of modern EDL theory including recent descriptions and formulations of the basic structure (and component regions) of the EDL is given by Dukhin *et al.* (2001).

The phenomenon of electrokinetics may be broadly classified into four types: a) electroosmosis, b) electrophoresis, c) streaming potential, and d) sedimentation potential. In this study we are only interested in and focus on electroosmosis and electrophoresis, because these two electrokinetic phenomena are most relevant to microfluidic systems. The qualitative descriptions of electroosmosis and electrophoresis are as follows:

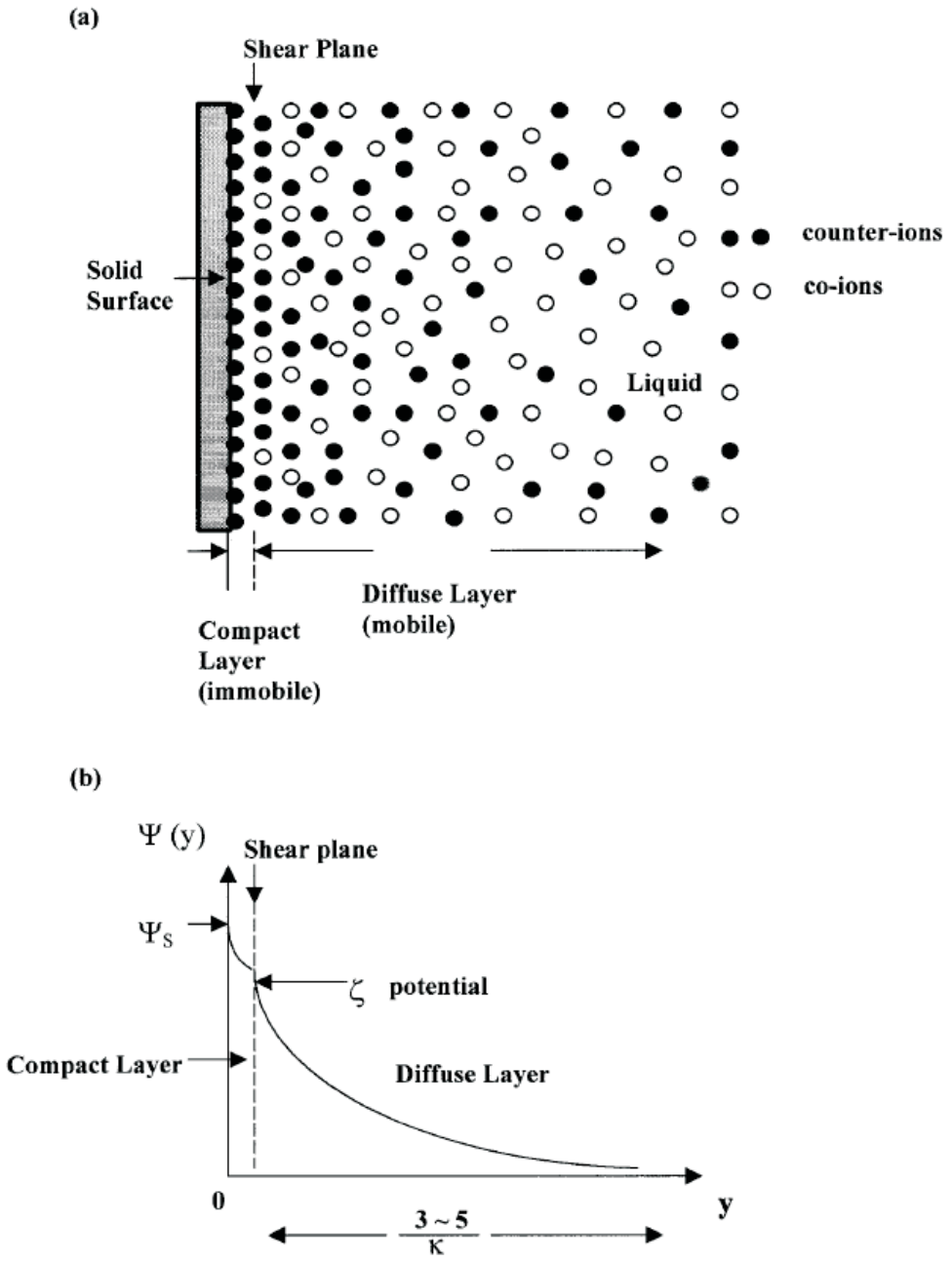

Figure 1.2 (a) Schematic of a simple EDL model; (b) A plot of electrical potential versus distance from the wall (not to scale).

a) Electrosmosis refers to the motion of bulk aqueous liquid in response to an applied electric field in a channel with electric double layers on its wetted surfaces.
b) Electrophoresis refers to the motion (relative to the bulk liquid) of charged colloidal particles suspended in a solution or molecules dissolved in a solution that results upon the application of an electric field.

Electroosmosis. According to its definition, electroosmosis refers to the movement of an electrolyte solution relative to a stationary charged surface (*i.e.*, a capillary tube, porous media) due to applied electric field. The pressure necessary to counterbalance electroosmotic flow is termed as the electroosmotic pressure. A typical electroosmotic fluid flow in a capillary is shown in Figure 1.3. When the capillary tube is negatively charged, the applied electric field exerts a force along the cathode direction on the excess positively charged ions near the surface. The positively charged ions drag the electrolyte solution, and thus liquid flow occurs towards the cathode, resulting in the electroosmotic flow. In case of thin EDL, the electric potential throughout most of the cross-sectional area of a microchannel is negligible and the expression for the electroosmotic flow, for the case of zero pressure gradients, is expressed as (Probstein, 1994)

$$u_{\mathrm{eo}} = -\frac{\varepsilon_{\mathrm{r}}\varepsilon_0\zeta E}{\mu} \tag{1.1}$$

which is the Helmholtz-Smoluchowski relation for electroosmotic flow. Since the typical thickness of an EDL is in the range of 1 to 100 nm and the typical size of microfluidic channels is of order $10 \sim 100$ μm (Stone *et al.*, 2004), the electroosmotic velocity profile inside the EDL region becomes insignificant, and thus the electroosmotic flow can be considered to be induced by a moving wall with velocity (slip velocity) given by Eq. (1.1). This method is often used in modeling electrokinetic problems in microfluidics (Cummings *et al.*, 2000; Santiago, 2001).

Two important electroosmotic flow parameters relevant to experimental measurements follow from this discussion. The first is the electroosmotic mobility, μ_{eo}, of a microchannel defined as the field-specific velocity of an electroosmotic flow with zero pressure gradient: $\mu_{\mathrm{eo}} = u_{\mathrm{eo}}/E$. The mobility is a fairly generally applicable concept

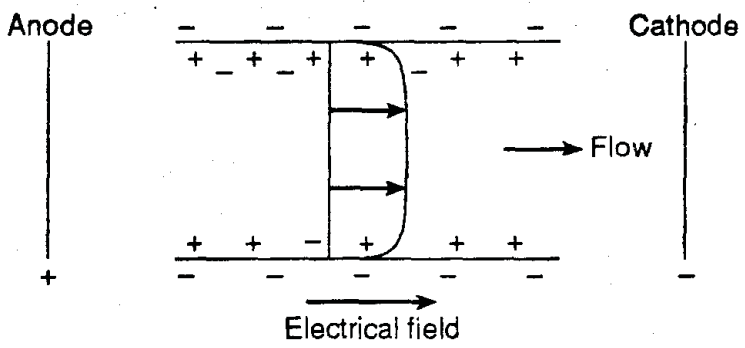

Figure 1.3 Electroosmotic flow in a capillary.

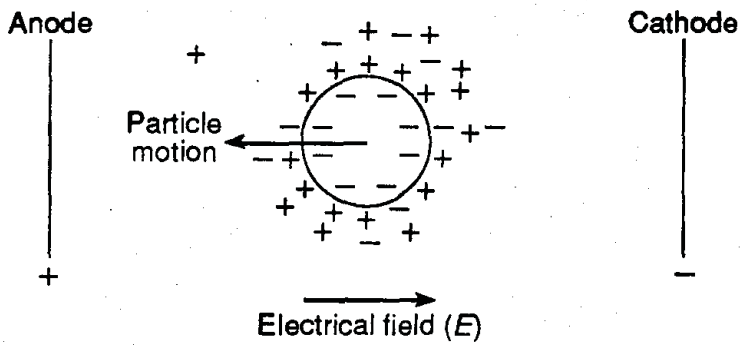

Figure 1.4 Electrophoresis of a particle.

as it describes the empirically observed proportionality between electric field and fluid velocity. For cases where Joule heating effects are negligible, the mobility is considered a constant of proportionality for a given wall material and solution chemistry. The second electroosmosis parameter is the zeta potential of the channel wall.

Electrophoresis. Electrophoresis refers to the movement of a charged surface relative to a stationary liquid under an applied electric field. A typical particle electrophoresis is shown in Figure 1.4. The negatively charged colloidal particle migrates towards the anode. Electrophoresis phenomenon is usually employed in measuring the surface potential of a charged particle.

In other words, electrophoresis is the induced motion of colloidal particles or molecules suspended in ionic solutions and is resulted from the application of an electric field. The electromigration of these species are classified into two regimes, based

on the ratio of the size of the particle or molecule to the Debye length of the solution. First, consider the electrophoresis of ionic molecules and macromolecules whose characteristic diameter are much smaller than the Debye length of the solution of interest. Under this condition, the electrophoretic velocity is given by (Probstein, 1994)

$$u_{\mathrm{ep}} = \frac{2}{3}\frac{\varepsilon_{\mathrm{r}}\varepsilon_0\zeta_{\mathrm{p}}E}{\mu} \tag{1.2}$$

A second limiting situation arises during electrophoresis of relatively large particles. Examples of large particles relevant to microfluidics include 100 $\sim$ 10,000 nm diameter polystyrene spheres and $\sim$ 10 μm diameter cells or single-celled organisms. In this second limiting case the electrophoretic velocity is a function of the electrostatic forces on the surface charge, the electrostatic forces on their charge double layers, and the viscous drag associated with both the motion of the particle as well as the motion of the ionic cloud around the particle. For a wide range of cases where the particle diameter-to-Debye length ratio is large so that, locally, the ionic cloud near the particle surface can be approximated by the EDL relations for a flat plate, the velocity of an electrophoretic particle is expressed as (Probstein, 1994)

$$u_{\mathrm{ep}} = \frac{\varepsilon_{\mathrm{r}}\varepsilon_0\zeta_{\mathrm{p}}E}{\mu} \tag{1.3}$$

In certain applications, such as micro-PIV technique, the 100 $\sim$ 1000 nm diameter seed particles typically fall into thin EDL particle flow regime. As in the discussion above for electroosmotic flows, Eqs. (1.2) and (1.3) demonstrate a direct proportionality between velocity and electric field which can be used to formulate an empirical mobility parameter of the form $\mu_{\mathrm{ep}} = u_{\mathrm{ep}}/E$. Applying the theoretical models discussed above, the two definitions of mobility are $\frac{2\varepsilon_{\mathrm{r}}\varepsilon_0\zeta_{\mathrm{p}}}{3\mu}$ and $\frac{\varepsilon_{\mathrm{r}}\varepsilon_0\zeta_{\mathrm{p}}}{\mu}$ for particles diameters small and large with respect to Debye length, respectively.

The theory relating the two limits described above has been discussed by Russel *et al.* (1999). In fact, the two limits can be combined into a universal expression for electrophoretic velocity. According to the Henry's theory (Probstein, 1994), the

velocity of electrophoresis can be expressed as:

$$u_{\mathrm{ep}} = \frac{2}{3} f\left(\kappa a\right) \frac{\varepsilon_{\mathrm{r}} \varepsilon_0 \zeta_{\mathrm{p}} E}{\mu} \tag{1.4}$$

In this expression, $f\left(\kappa a\right)$ is called the Henry function, which is simplified by Ohshima (1994) as:

$$f(\kappa a) = 1 + \frac{1}{2\left[1 + \dfrac{2.5}{\kappa a(1 + 2\mathrm{e}^{-\kappa a})}\right]^3} \tag{1.5}$$

where $\kappa a = a/\lambda_{\mathrm{D}}$, a is the radius of the spherical particles, and $\lambda_{\mathrm{D}} = \sqrt{\frac{\varepsilon_{\mathrm{r}} \varepsilon_0 k_{\mathrm{b}} T}{2\mathrm{e}_0^2 z_{\mathrm{v}}^2 n_0}}$ is the Debye length (where e_0 is the fundamental charge, z_{v} is the valence of the symmetric electrolyte, n_0 is the ionic number concentration of the bulk electrolyte, k_{b} is the Boltzmann constant, and T is the absolute temperature).

1.5 Literature Review

In the literature, numerous theoretical and experimental studies have been reported on the electrokinetic flows. For steady-state electroosmotic flows, several classical research works have paved the way for the further studies up to date. Among those earliest works, for examples, are the ones led by Burgreen and Nakache (1964), who formulated a mathematical model for the electroosmotic flow in an ultrafine slit, and Rice and Whitehead (1965), who analyzed the electrokinetic flow field in a narrow cylindrical capillary. In later efforts, Santiago (2001) validated a sufficient set of conditions for the slip velocity approximation in microfluids. Cummings *et al.* (2000) examined the conditions for similitude between the fluid velocity and the electric field in electroosmotic flow, and discussed numerical simulations in EOF. Yang *et al.* (1998) provided a conclusion of validating the Boltzmann distribution in the case of microchannel flows, which is that for a microchannel flow with a very small Peclet number or in a fully-developed hydrodynamic state, the Boltzmann equation is still valid.

Several studies have been reported on experimental measurement of the steady-

state EOF. Taylor and Yeung (1993) employed an imaging system using a microscope and a CCD camera, and realized direct measurement of the fluid motion inside the capillary. Using a laser-Doppler shift technique, Oka and Furusawa (1998) measured the particle velocity profile in a closed cell of 4 mm by 4 mm cross-section. Thus, the particle electrophoretic velocity and the fluid EOF velocity were determined using the experimental data and theoretically derived correlations.

Due to the fast development of flow visualization techniques, micro-particle image velocimetry (PIV) technique has been widely used to diagnose the velocity profiles and probe electroosmotic flow characteristics in microfluidic channels. However, it also should be noted that as micro-PIV technique utilizes tracer particles that are usually charged in aqueous liquids, the velocity field obtained is a combination of the electrophoretic velocity of the tracer particles which is related to the particle electrophoretic mobility and the electroosmotic flow field which is associated with the zeta potential of the channel wall. To obtain the electroosmotic flow field, the electrophoretic component has to be subtracted from the micro-PIV measured particle velocity so that the electroosmotic flow field can be retrieved. In fact, the zeta potential of the channel wall is an important parameter for characterizing the channel wall materials and modeling electrokinetic flows. Devasenathipathy and Santiago (2002) applied micro-PIV to demonstrate the similarity between electric and velocity fields. Kim *et al.* (2002) presented a comparative study of micro-PIV measurements and numerical simulation of electrokinetic flows in grooved and T-junction channels. MacInnes *et al.* (2003) studied electrokinetic flow in a T-junction microchannel. Experiments were carried out using a micro-PIV based simple particle tracking method with pulsed light imaging. Numerical simulations were found to agree with the measured particle velocity profiles within experimental uncertainty of 5%. Recently, Sadr *et al.* (2004) developed a nano-PIV technique to measure the near-wall velocity field in a steady-state electroosmotic flow.

Exclusively, the aforementioned studies center on the velocity field of steady-state electroosmotic flows. In the present study, we will focus on time- and frequency-

dependent electroosmotic flow. As an important electrokinetic application, the topic of EK mixing will be studied systematically. Hence, a detailed review of the literature will be presented in the following, with emphasis on two major aspects: (1) studies of time-dependent and frequency-dependent electroosmotic flows, and (2) studies of electrokinetic micromixers.

1.5.1 Transient and time-dependent electroosmotic flow

In contrast to the theoretical investigations on time-dependent EOF, very few experimental studies of the time-dependent EOF have been reported in the literature. In fact, direct visualization of the dynamic electrokinetic flows is of fundamental importance as it provides insight into the underlying mechanisms of the development and stability of electrokinetic flows (Suresh and Homsy, 2004). Furthermore, study of the dynamic aspects of the electrokinetic flow plays a crucial role in the development of relevant microfluidic technologies, such as microfluidic pumping, micro mixing, *etc.* Here, for avoiding confusion, it should be pointed out that the word "transient" denotes short time-dependent processes, *e.g.*, start-up transient processes, and "time-dependent" represents comparatively long time running processes.

In an earlier study, Hanna and Osterle (1968) investigated the start-up transient electro-osmosis of DI water in round capillary tubes by employing the Laplace transform technique. In their analysis, the effects of hydrodynamic resistance, electrical conductance and fluid inertia are considered, and the effects of fluid compressibility and electrical capacitance and inductance are neglected. Considering the time scale of the electric double layer dynamic response, Ivory (1983) obtained a simple analytical solution for the transient electroomotic velocity of electrolyte solutions near a solid surface whose local radius of curvature is much greater than the Debye layer. Tikhomolova (1993) originally solved the non-stationary electroosmotic flow with non-slipping boundary conditions. Using the Debye-Hückel approximation, Keh and Tseng (2001) studied the transient electrokinetic flow in a fine capillary slit (parallel plates) and compared the results with those in a cylindrical tube. Using the Green's function

approach, Yang *et al.* (2002) revisited the transient EOF in a slit microchannel but with considering both low and high potential regimes in the EDL region. In modern microfluidic applications, most channels in the micro devices and MEMS are made by micromachining technologies, and the cross-section of these channels is close to a rectangular shape. Due to this fact, employing the Debye-Hückel approximation and Green's function approach, Yang (2002) first theoretically investigated the start-up transient EOF in a rectangular microchannel.

Regarding the experimental studies on transient EOF, Söderman and Jonsson (1996) developed a theoretical frame work for the description of the EOF velocity profiles in different geometries with both temporal and spatial resolution. In their work, they compared the results of the theoretical predictions with the velocity profiles obtained from experiment using NMR imaging techniques.

Using micro-PIV technique, Kim and Khim (2004) studied EOF in straight and T-junctioned microchannels. They observed the time-dependent reservoir size effect due to the adverse pressure gradient, which is resulted from the downstream reservoir height rise with flow. However, no theoretical analysis was provided.

1.5.2 Frequency-dependent electroosmotic flow

Frequency-dependent electroosmotic flow is a special case of AC electrokinetics, which is an active research topic (Morgan and Green, 2003). In principle, the frequency-dependent electroosmotic flow can also be classified as the time-dependent electroosmotic flow. However, due to its periodic characteristics, frequency-dependent EOF has specific features, such as frequency and amplitude, which can be implemented and manipulated for potential applications.

Numerous studies have been reported on the frequency-dependent electroosmotic flows in simple geometrical channels, including slit, cylindrical, and rectangular microchannels. Dutta and Beskok (2001) obtained analytical solutions of time periodic electroosmotic flows in a slit channel, and compared the analytical solution with the one from solving the Stokes' second problem. They found that the electroosmotic flow

differs from the Stokes' second solution within the EDL, but matches well in the bulk flow region. Kang *et al.* (2002) investigated the dynamic aspects of electroosmotic flow in a cylindrical microcapillary. Not only having obtained some similar results as Dutta's, they also applied an analytical scheme to treat the problem under arbitrary zeta potentials. In addition, they proposed a characteristic frequency to study the characteristic features of the oscillating EOF and validated the assumption of equilibrium Boltzmann distribution under AC applications, *e.g.*, the frequency of the external electric field cannot be very high (less than 1 MHz). Bhattacharyya *et al.* (2003) also studied this problem but only limited to the Debye-Hückel approximation. Further, they discussed the streaming potential under oscillating pressure field.

Due to the important applications of rectangular microchannels, several efforts have been made. Marcos *et al.* (2004a) studied the frequency-dependent laminar EOF in open-end rectangular microchannels. Yang *et al.* (2003) analytically addressed the EOF and streaming potential in an infinitely extended rectangular microchannel (open-end). They employed the methods of Green's function and phasor notation to solve the mathematical models, and conducted parametric studies on steaming potential and electroviscous effects. Using a combined theoretical and numerical approach, Erickson and Li (2003) investigated the time periodic electroosmotic flow in a rectangular microchannel. Using the Green's function method, they obtained an analytical solution to the EOF filed driven by a sinusoidal electric field. They also analyzed the response of the EOF field to applied electric field of complex waveforms. In one of the latest developments, Xuan and Li (2005) investigated the electroosmotic flow in microchannels with arbitrary geometry and artitrary distribution of wall charges.

Compared to open-end channels, closed-end channels have their special features. For a closed system it is possible to create a pressure gradient using electroosmotic force, which can be potentially used for actuation of micro pistons or micro bellow mechanisms. These promising prospects of micro-scale applications have attracted some researchers' attention. Marcos *et al.* (2004b) analytically studied frequency-dependent laminar electroosmotic flow in a closed-end rectangular microchannel by

using the Green's function method together with a complex variable approach (phasor notation). In their work, they analyzed the development of EOF in a closed-end rectangular channel under AC electric field applied. Reppert and Morgan (2002) investigated frequency-dependent electroosmosis in a closed cylindrical capillary by a different analytical approach from that of Marcos', and they solved the problem by treating the flow field as a near-wall region and a bulk-fluid region respectively. They also did experiments to measure the pressure for verifying the theoretical model, and a good agreement was obtained. Later, using the finite element method, Reppert and Khan (2005) revisited the same problem and compared with the analytical model developed by Reppert and Morgan (2002). Considering the application of a stepwise voltage, Mishchuk and Gonzelez-Caballero (2006a and 2006b) analytically studied the nonstationary electroosmotic flows in both open- and closed-end cylindrical capillaries.

Recently, due to increasing interests in electrokinetic flow in porous media, Kang *et al.* (2004) presented a theoretical study on AC-driven electroosmotic flow in both open-end and closed-end microchannels packed with uniformly charged spherical microparticles. They studied the effects of pore size and the excitation frequency on EOF in an open-end capillary and the effects of packing particles on backpressure in a closed-end capillary under a fixed excitation frequency.

In electrokinetic applications, it is important to measure the particle's mobilities, in order to probe the features in the fluidic system, *e.g.*, measuring zeta potentials. Minor *et al.* (1997) presented a method of measuring particle mobilities by applying an alternating electric field with certain frequency under which electroosmosis is suppressed, whereas the particles are still able to follow the field according to their DC mobility. The principle was demonstrated by measurements performed with a laser-Doppler microelectrophoretic device in an alternating electric field as a function of frequency and position. As a result, this method overcomes the problems associated with electroosmosis in finding the stationary level in conventional electrophoretic cells. Oddy and Santiago *et al.* (2003) presented a method to determine the electrophoretic and electroosmotic mobilities by measuring the particle displacements in both AC and

DC electric fields. Using the two-color micro-PIV technique, Meinhart *et al.* (2003) and Wang *et al.* (2005) experimentally investigated the AC electrokinetic flows.

In order to investigate the stability of AC electroosmotic flow, using the thin double layer approximation Suresh and Homsy (2004) performed a linear stability analysis of electroosmotic flow in a slot geometry. They drew a conclusion that the system is linearly stable over a wide range of parameters.

1.5.3 Review on electrokinetic micromixers

Mixing in microfluidic systems is a difficult task, because under the low Reynolds number flow, the channel size is too small to shelter turbulence or hydrodynamic fluctuations. On the other hand, molecular diffusion based mixing is not a very good approach to improve micromixing performance, because microsystems are, in most cases, too large for diffusive mixing. Two review papers by Ottino and Wiggins (2004) and Nguyen and Wu (2005) discuss on the issues of improving micromixing with aid of chaotic flows and provide comments on the current situations and future trend of micromixing studies.

Generally, based on different external forces imposed on microfluidic systems, microfluidic mixers can be classified as pressure-driven and electrokinetically driven mixing. Many studies have been conducted for improving mixing effects in pressure-driven microfluidic systems. Employing hydrodynamic focusing and time-interleaved segmentation, Nguyen and Huang (2005) improved mixing effects in pressure-driven microflows. Using a passive method, Strook *et al.* (2002) developed a chaotic micromixer in which the mixing length has been shortened. In principle, electrokinetic micromixers belong to the category of active micromixers, because they need external electric forces to drive the flow. There are certain advantages and disadvantages in electrokinetic microfluidic mixing systems. The most important feature of electrokineitc flow is that the flow patterns can be adjusted by modulating the external electric field, either by amplitude or frequency. This feature can be implemented for enhancing micromixing. In addition, the advantages of electrokinetic pumping are

well-known, such as no moving parts, ease of control, *etc.* However, the flat velocity profile is a disadvantage for electrokinetic mixing, because this nature drastically reduces the Taylor-Aris dispersion (Taylor, 1953; Aris, 1956) in microfluidic systems, which is an effective mechanism to enhance micromixing (Ghosal, 2006).

Lastochkin *et al.* (2004) presented a micromixer design using AC electroosmotic flow based on AC Faradaic polarization. Jacobson *et al.* (1999) developed microfluidic designs that simplify the voltage control to perform parallel and serial electrokinetic mixing on microchips. Sundaram and Tafti (2004) presented numerical simulations of electrokinetically induced mixing in a microchamber (plain or with baffles) in the presence of a fluctuating electric field, and made recommendations on the optimal choice of nondimensional frequency and driving potential to lead to the best mixing effects. Huang and Breuer (2003) conducted an experimental study on the performance and scaling of an electroosmotic mixer, in which they used pressure-driven pumping and electroosmotic oscillatory perturbation on the fluid to improve the mixing.

Using FEMLAB software, Chen *et al.* (2003) presented a numerical study of a ring electroosmotic micromixer, in which four strategically integrated electrodes impose spatial and time varying electric field hence to perturb the flow pattern. Further, Zhang *et al.* (2003) designed and fabricated an electroosmosis-driven ring micromixer using the silicon bulk micromachining technology. The electroosmotic ring micromixer uses a novel arrangement of electrodes and flow obstacles to induce chaotic mixing. The design was tested by a micro-PIV system. In their experiment, as the fluid is pumped by pressure, it is possible to use low AC voltage to perturb the fluid. However, this design requires the complicated geometry and the moving parts (such as a syringe pump).

Recently, a novel micromixing strategy was proposed and analyzed numerically by Coleman and Sinton (2005), by exploiting the axial diffusion of a continuous sequence of discrete samples in a microchannel. Further, using rapid electric field switching, Coleman *et al.* (2006) fabricated a symmetry-based microfluidic mixer and provided an estimation of the preferred operating frequency range.

T-mixer (including Y-mixer) is a widely used device in microfluidic applications, which has a simple geometry and numerous advantages such as simultaneously mixing and transport of sample solutes. For electrokinetic T-mixers, Tang *et al.* (2002) presented a numerical and experimental study of electrokinetic flow control for composition modulation in T-microchannels. They studied the electric field frequency range, under which the banded composition structure can be achieved. This work may be among the earliest studies on the frequency-dependent modulation of electrokinetic microflows, but it is mainly focusing in flow modulation rather than micromixing. A numerical study by MacInnes (2002) focuses on the electrokinetic flow in situations where chemical reactions play a central role. This study provided a detailed parametric analysis by using scaling laws, and compared the simulation results for 2D and 3D under both electrokinetic and pressure driven conditions. The computations show that the 3D results are close to the 2D case for electrokinetic flow, but for pressure driven flow the results are significantly changed. Physically, this difference can be understood as follows: in the pressure driven flows the velocity profile is usually of parabolic shape, in which the top and bottom walls of the channel have strong influence on the flow pattern, resulting in Taylor dispersion induced mixing effects. However, in the electrokinetic flows, the velocity profile is plug-like, which reduces the top and bottom wall effect on the flow and thus on the mixing. This 2D-3D similarity in electrokinetic mixing gives a viable approach to use simplified numerical 2D models to simulate the electrokinetic mixing process.

Utilizing time-pulsed electroosmotic flows, Glasgow *et al.* (2004) investigated the electrokinetic micromixing in T channels. They used 2 series of square or sinusoidal waves with offset and phase difference to improve mixing effects. In addition to numerical simulations and experimental investigation, they used several dimensionless numbers such as Strouhal number, Stokes number and pulse volume ratio (PVR) to analyze the mixing process. Similarly, Lin *et al.* (2004) and Fu *et al.* (2005) developed several schemes to improve electrokinetic micromixing, such as different switching modes and channel structures. They conducted numerical simulations for parametric

study and experimental verification.

Efforts have also been made to study the effects of geometry and heterogeneity of the channel zeta-potential. Johnson *et al.* (2002) experimentally investigated the rapid microfluidic mixing with a series of slanted wells created at the T-junction. Chang and Yang (2004) presented a numerical study on electrokineticaly driven flow mixing in microchannels with patterned blocks. Their simulation results confirmed that the patterned blocks improve the diffusive mixing. Erickson and Li (2002) numerically investigated the effects of heterogeneous surface charges on electrokinetic micromixing, and further Biddiss *et al.* (2004) conducted experimental work to verify Erickson and Li's analyses. Lee *et al.* (2004) proposed an electrokinetically driven active micromixers utilizing zeta potential variation induced by field effects. Ng *et al.* (2004) numerically investigated the electrokinetic generation of microvortex using surface charge micropatterning.

In order to enhance mixing efficiency, an approach of using the electrokinetic instability was proposed by Oddy *et al.* (2001). This mechanism is based on the instability development under a fluctuating electric field. Lin *et al.* (2004) showed that the instabilities can be caused by conductivity gradients between the two sample streams driven by a DC electric field. Further, Chen *et al.* (2005) analyzed the induced mixing at the flow downstream of the T-junction. Similarly, Moctar *et al.* (2003) proposed a micromixer based on the electro-hydrodynamic force when the fluids to be mixed have different electrical properties and are subjected to an electric field.

1.5.4 Summary and comments on the previous studies

In conclusion, the literature survey has indicated that experimental characterization of time- and frequency-dependent electroosmotic flows poses great challenges to up-to-date experimental techniques, and very few relevant studies have been reported in the literature. Although several efforts have been made to employ electrokinetic flows in the micromixing applications, no systematical studies have been conducted to examine various factors affecting EK mixing efficiency.

Chapter 2

A Method for Simultaneously Determining the Zeta Potentials of the Channel Surface and the Tracer Particles

2.1 Introduction

In colloid and interface science, zeta potential is an experimentally measurable electrical potential that characterizes the EDL, and it plays an important role in many applications such as stability of colloidal dispersion, characterization of biomedical polymers, electrokinetic transport of particles, and capillary electrophoresis, *etc.* In addition, electrokinetic mobilities and zeta-potentials of the particles and the channel wall are crucial to the design and process control of microfluidic devices.

Numerous techniques have been used to characterize electroosmotic flow in microchannels. The details can be found in the literature review presented in Chapter 1. In the current chapter, using the micro-PIV technique, the electroosmotic flows are characterized in both open- and closed-end rectangular microchannels. Because both the channel surface and the tracer particles are charged, a novel method is proposed

for simultaneously determining the zeta potentials of both the channel surfaces and the tracer particles. This method combines the theories of electroosmosis and electrophoresis, and utilizes the micro-PIV technique to measure the steady electrokinetic velocity distributions of tracer particles in open- and closed-end microchannels.

2.2 Mathematical Model

Micro-PIV technique is used to measure the steady velocity of tracer particles in an electrolyte in both open- and closed-end microchannels. Under an applied DC electric field, the observed particle velocity, u_{p} evaluated from the micro-PIV measurement is the superposition of the electrophoretic velocity of the charged particle, u_{ep}, and the electroosmotic velocity of the electrolyte, u_{eo}:

$$u_{\mathrm{p}} = u_{\mathrm{eo}} + u_{\mathrm{ep}} \tag{2.1}$$

In the following, the analytical expressions for u_{ep} and u_{eo} in open- and closed-end rectangular microchannels will be provided.

2.2.1 Velocity distribution of the steady electroosmotic flow in open- and closed-end microchannels – Slip Velocity Approach

Consider a rectangular microchannel having a height, $2h$, a width, $2w$, and a length, l as shown in Figure 2.1. The liquid filled in the microchannel is assumed to be an incompressible, Newtonian, symmetric electrolyte of constant density, ρ, viscosity, μ, and dielectric constant, ε_{r}. The channel wall is assumed to be uniformly charged with a zeta potential, ζ_{w}. When an external electric field, E is applied along the axial direction of the channel, the liquid sets into motion as a result of the interaction between the net charge density in the electric double layer (EDL) of the channel and the applied electric field.

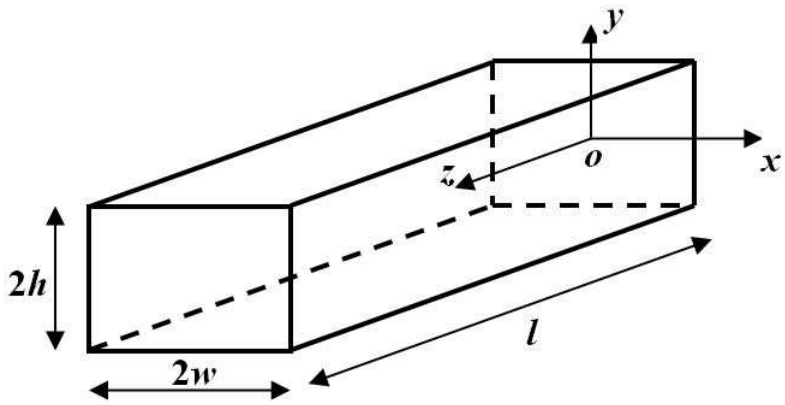

Figure 2.1 Geometry of the rectangular channel. The channel length is l and the width and height of the channel cross section is $2w \times 2h$.

The driving force of electroosmotic flow is present only within the EDL. The typical thickness of an EDL is in the range of 1 to 100 nm (Hunter, 1981); while the characteristic hydraulic diameter of microfluidic channels is of order 10 to 100 μm (Erickson and Li, 2004). Because of such orders of the magnitude difference, the electroosmotic velocity profile inside the EDL region becomes insignificant, and thus the electroosmotic flow can be considered to be induced by a moving wall with a velocity (*i.e.*, slip velocity) given by the Helmholtz-Smoluchowski equation

$$u_{\mathrm{s}} = -\frac{\varepsilon_0 \varepsilon_{\mathrm{r}} \zeta_{\mathrm{w}} E}{\mu} \tag{2.2}$$

In the literature, the fluid flow actuated by moving boundary of the wall and driven by hydrodynamic shear stresses is referred to as the Stokes second problem (Telionis, 1981), and is specifically referred to as the slip velocity approach in electroosmotic flows. More general discussions of the applicability of such slip velocity approach in electrokinetic flows were provided by Cummings *et al.* (2000) and Santiago (2001). Using the slip velocity approach, the steady velocity field of a fully-developed flow driven by an applied electric field, E and a pressure gradient, $\mathrm{d}p/\mathrm{d}z$ is governed by the Stokes equation, expressed as (Probstein, 1994)

$$\frac{\partial^2 u}{\partial x^2} + \frac{\partial^2 u}{\partial y^2} = \frac{1}{\mu}\frac{\mathrm{d}p}{\mathrm{d}z} \tag{2.3}$$

The appropriate boundary conditions applicable to Eq. (2.3) are

$$u\,|_{x=w} = u_{\mathrm{s}} \qquad u\,|_{y=h} = u_{\mathrm{s}} \tag{2.4}$$

$$\left.\frac{\partial u}{\partial x}\right|_{x=0} = 0 \qquad \left.\frac{\partial u}{\partial y}\right|_{y=0} = 0 \tag{2.5}$$

Eq. (2.3) together with its boundary conditions specified by Eqs. (2.4) and (2.5) can be non-dimensionalized by using the following dimensionless parameters:

$$\overline{u} = \frac{u}{U} \qquad X = \frac{x}{D_{\mathrm{h}}} \qquad Y = \frac{y}{D_{\mathrm{h}}} \qquad Z = \frac{z}{D_{\mathrm{h}}\mathrm{Re}} \qquad \bar{P} = \frac{p}{\rho U^2}$$

where U is the reference velocity, $D_{\mathrm{h}} = 4wh/(w+h)$ is the hydraulic diameter of the rectangular channel, and $\mathrm{Re} = \rho D_{\mathrm{h}} U/\mu$ is the reference Reynolds number. Further, a transform is introduced as

$$\bar{v} = \bar{u} - \bar{u}_{\mathrm{s}} \tag{2.6}$$

Then, the governing Stokes equation and its boundary conditions can be rewritten in dimensionless form as

$$\frac{\partial^2 \bar{v}}{\partial X^2} + \frac{\partial^2 \bar{v}}{\partial Y^2} = \frac{\mathrm{d}\bar{P}}{\mathrm{d}Z} \tag{2.7}$$

with the boundary conditions

$$\bar{v}\,\big|_{X=w/D_{\mathrm{h}}} = 0 \qquad \bar{v}\,\big|_{Y=h/D_{\mathrm{h}}} = 0 \tag{2.8}$$

$$\left.\frac{\partial \bar{v}}{\partial X}\right|_{X=0} = 0 \qquad \left.\frac{\partial \bar{v}}{\partial Y}\right|_{Y=0} = 0 \tag{2.9}$$

where $\bar{v} = \frac{v}{U}$ and $\bar{u}_{\mathrm{s}} = \frac{u_{\mathrm{s}}}{U} = -\frac{\varepsilon_0 \varepsilon_{\mathrm{r}} \zeta_{\mathrm{w}} E}{\mu U}$.

Using the Green's function method, the solution of Eq. (2.7) subjected to the boundary conditions given by Eqs. (2.8) and (2.9) can be explicitly expressed as

(Ozisik, 1993)

$$\bar{v}(X,Y) = \lim_{\bar{t}\to\infty} \int_{\tau=0}^{\bar{t}} \mathrm{d}\tau \int_{X'=0}^{w/D_\mathrm{h}} \int_{Y'=0}^{h/D_\mathrm{h}} G(X,Y,\bar{t}\,|X',Y',\tau) \left(-\frac{\mathrm{d}\bar{P}}{\mathrm{d}Z}\right) \mathrm{d}X'\mathrm{d}Y' \tag{2.10}$$

Here, the Green's function can be obtained by using the separation of variables method. The expression for $G(X,Y,\bar{t}\,|X',Y',\tau)$ is given by (Ozisik, 1993)

$$G(X,Y,\bar{t}\,|X',Y',\tau) = \frac{4D_\mathrm{h}^2}{wh} \sum_{m=1}^{\infty}\sum_{n=1}^{\infty} \cos(\alpha_m X)\cos(\alpha_m X') \times \cos(\beta_n Y)\cos(\beta_n Y')\,\mathrm{e}^{-T_{mn}\,(\bar{t}-\tau)} \tag{2.11}$$

where $\alpha_m = \left(\frac{2m-1}{2}\right)\frac{D_\mathrm{h}}{w}\pi$, $\beta_n = \left(\frac{2n-1}{2}\right)\frac{D_\mathrm{h}}{h}\pi$ and $T_{mn} = \alpha_m^2 + \beta_n^2$. Substituting Eq. (2.11) to Eq. (2.10) and carrying out the integration, one can obtain

$$\bar{v}\,(X,Y) = -\frac{\mathrm{d}\bar{P}}{\mathrm{d}Z}\frac{16}{\pi^2}\sum_{m=1}^{\infty}\sum_{n=1}^{\infty} \frac{(-1)^{m+n}\cos(\alpha_m X)\cos(\beta_n Y)}{(2m-1)(2n-1)\,T_{mn}} \tag{2.12}$$

Here, two cases are considered:

Case 1: Electroosmotic flow field in an open-end rectangular microchannel

In this situation, $\mathrm{d}\bar{P}/\mathrm{d}Z \equiv 0$, because no external pressure is applied (assuming that the microchannel is infinitely extended). Thus, Eq. (2.12) becomes

$$\bar{v}\,(X,Y,\bar{t}) = 0 \quad \text{or} \quad \bar{u}(X,Y,\bar{t}) = \bar{u}_\mathrm{s} \tag{2.13}$$

Eq. (2.13) shows that for steady, fully-developed electroosmotic flow in an open-end rectangular microchannel, the slip velocity approach leads to a "plug-like" velocity profile, given by the Smoluchowski equation:

$$u_{\mathrm{eo-open}} = -\frac{\varepsilon_\mathrm{r}\varepsilon_0\zeta_\mathrm{w}E}{\mu} \tag{2.14}$$

Case 2: Electroosmotic flow field in a closed-end rectangular microchannel

Due to the closed-end structure, a backpressure gradient $\mathrm{d}\bar{P}/\mathrm{d}Z$ is induced to fulfill

the condition of the zero net flow rates, which mathematically is expressed as

$$\int_{X=-w/D_\mathrm{h}}^{w/D_\mathrm{h}} \int_{Y=-h/D_\mathrm{h}}^{h/D_\mathrm{h}} \bar{u}\left(X,Y,\bar{t}\right)\mathrm{d}X\,\mathrm{d}Y = 0 \tag{2.15}$$

For an infinitely extended channel, $\mathrm{d}\bar{P}/\mathrm{d}Z$ is constant along the axial flow direction (Marcos *et al.*, 2004b). Substituting Eqs. (2.6) and (2.12) into Eq. (2.15), one can show that the dimensionless induced pressure gradient is given by

$$\frac{\mathrm{d}\bar{P}}{\mathrm{d}Z} = \frac{\pi^4}{64}\frac{\bar{u}_\mathrm{s}}{\sum_{m=1}^{\infty}\sum_{n=1}^{\infty}\frac{1}{(2m-1)^2(2n-1)^2 T_{mn}}} \tag{2.16}$$

Further substituting Eq. (2.16) back to Eq. (2.12) and noticing that $\bar{v} = \bar{u} - \bar{u}_s$, one can obtain

$$\bar{u}\left(X,Y\right) = \bar{u}_\mathrm{s} - \frac{\pi^2\bar{u}_\mathrm{s}}{4}\frac{\sum_{m=1}^{\infty}\sum_{n=1}^{\infty}\frac{(-1)^{m+n}\cos\left(\alpha_m X\right)\cos\left(\beta_n Y\right)}{(2m-1)(2n-1)T_{mn}}}{\sum_{m=1}^{\infty}\sum_{n=1}^{\infty}\frac{1}{(2m-1)^2(2n-1)^2 T_{mn}}} \tag{2.17}$$

Eq. (2.17) gives the electroosmotic velocity distribution in a closed-end rectangular microchannel.

As the microscope objective lens is focused on the mid-plane of the channel (*i.e.*, $Y = 0$) during the micro-PIV experiment, the dimensional electroosmotic velocity at the mid-plane is expressed as

$$\begin{aligned} u_{\mathrm{eo-closed}}\left(X,0\right) &= \bar{u}_{\mathrm{eo-closed}}\left(X,0\right)U \\ &= -\zeta_\mathrm{w}\frac{\varepsilon_0\varepsilon_\mathrm{r}E}{\mu}\left[1 - \frac{\pi^2}{4}\frac{\sum_{m=1}^{\infty}\sum_{n=1}^{\infty}\frac{(-1)^{m+n}\cos\left(\alpha_m X\right)}{(2m-1)(2n-1)T_{mn}}}{\sum_{m=1}^{\infty}\sum_{n=1}^{\infty}\frac{1}{(2m-1)^2(2n-1)^2 T_{mn}}}\right] \end{aligned} \tag{2.18}$$

2.2.2 Electrophoretic velocity of the tracer particles

Under assumptions of the undisturbed EDL structure of a charged particle and the Debye-Hückel approximation, the electrophoretic velocity of tracer particles, according to Hunter (1981) can be expressed as:

$$u_{\mathrm{ep}} = \frac{2}{3} f\left(\kappa a\right) \frac{\varepsilon_{\mathrm{r}} \varepsilon_0 \zeta_{\mathrm{p}} E}{\mu} \tag{2.19}$$

A simple expression for Henry's function was provided by Ohshima (1994) as:

$$f(\kappa a) = 1 + \frac{1}{2\left[1 + \dfrac{2.5}{\kappa a(1 + 2\mathrm{e}^{-\kappa a})}\right]^3} \tag{2.20}$$

Here a is the radium of the tracer particle, and κ is the Debye parameter defined as $\kappa = \sqrt{\frac{2\mathrm{e}_0^2 z_{\mathrm{v}}^2 n_0}{\varepsilon_{\mathrm{r}} \varepsilon_0 k_{\mathrm{b}} T}}$ (where e_0 is the fundamental charge, z_{v} is the valence of the symmetric electrolyte, n_0 is the ionic number concentration of the bulk electrolyte, k_{b} is the Boltzmann constant, and T is the absolute temperature). It should be pointed out here that the Henry's expression for the electrophoretic velocity of tracer particles is applicable to both open-end and closed-end channels.

2.2.3 Relationships between the micro-PIV measured particle velocity in open- and closed-end channels and the zeta potentials of the channel surface and the particles

As indicated by Eq. (2.1), the particle velocity measured from the micro-PIV technique is a combination of the electrophoretic velocity of the tracer particles which is related to the particle zeta potential, ζ_{p} and the electroosmotic flow field which is associated with the zeta potential of the channel surface, ζ_{w}. If micro-PIV experiments are carried out in an electrolyte in open-end and closed-end microchannels, according to Eq. (2.1), the expressions for the micro-PIV measured velocity of the tracer particles

in open-end and closed-end rectangular microchannels can be written as below:

$$u_{\mathrm{p-open}} = u_{\mathrm{eo-open}}(\zeta_{\mathrm{w}},\, E_1) + u_{\mathrm{ep}}(\zeta_{\mathrm{p}},\, E_1) \tag{2.21}$$

$$u_{\mathrm{p-closed}} = u_{\mathrm{eo-closed}}(\zeta_{\mathrm{w}},\, E_2) + u_{\mathrm{ep}}(\zeta_{\mathrm{p}},\, E_2) \tag{2.22}$$

where E_1 and E_2 are the electric field applied across the open-end and closed-end channel, respectively.

We define the particle mobility, μ_{p} measured by micro-PIV technique in an electric filed, E as

$$\mu_{\mathrm{p}} = \frac{u_{\mathrm{p}}}{E} \tag{2.23}$$

Making use of the results of Eqs. (2.14), (2.18), and (2.19), we can further rewrite Eqs. (2.21) and (2.22) in terms of the measured particle mobility as

$$\mu_{\mathrm{p-open}} = \zeta_{\mathrm{w}} F + \zeta_{\mathrm{p}} G \tag{2.24}$$

$$\mu_{\mathrm{p-closed}} = \zeta_{\mathrm{w}} H(x) + \zeta_{\mathrm{p}} G \tag{2.25}$$

where the expressions for F, H, and G are given by

$$F = -\frac{\varepsilon_{\mathrm{r}}\varepsilon_0}{\mu} \qquad G = \frac{2}{3} f\left(\kappa a\right) \frac{\varepsilon_{\mathrm{r}}\varepsilon_0}{\mu} \tag{2.26}$$

$$H(x) = -\frac{\varepsilon_0\varepsilon_{\mathrm{r}}}{\mu}\left[1 - \frac{\pi^2}{4}\frac{\displaystyle\sum_{m=1}^{\infty}\sum_{n=1}^{\infty}\frac{(-1)^{m+n}\cos\left(\alpha_m x/D_{\mathrm{h}}\right)}{(2m-1)(2n-1)T_{mn}}}{\displaystyle\sum_{m=1}^{\infty}\sum_{n=1}^{\infty}\frac{1}{(2m-1)^2(2n-1)^2 T_{mn}}}\right] \tag{2.27}$$

In principle, Eqs. (2.24) and (2.25) show that if the distributions of the particle mobility measured by micro-PIV in the open-and closed-end channels are known, the zeta potentials of both the particles and the channel surface can be determined simultaneously.

2.3 Experimental Section

2.3.1 Measurement cell and materials used

The measurement cell consists of a borosilicate glass microchannel (VitroCom), a polymer holder, and two reservoirs. Such microchannel has a rectangular 300 μm × 300 μm cross-section and is 4 cm long. Prior to experiment, the cell was cleaned in an ultrasonic cleaner with a NaOH base solution and then flushed with deionized water. For the closed-end cell, Epoxy glue was used for sealing the two ends of the channel.

Fluorescent polystyrene particles of radius $a = 465$ nm (Duke Scientific Co.) were used for tracking the flow. Such tracer particles have the excitation and emission wavelength of 540 nm and 610 nm, respectively. In all experiments, the number concentration of tracer particles was approximately about 2×10^9 particles/ml.

A DC electric field was applied using platinum wire electrodes inserted into the two reservoirs connecting the two ends of the microchannel. A high-voltage power supply (PS350, Stanford Research) was used to apply 400 V potential difference on the two electrodes, giving rise to a 100 V/cm strength of the applied DC field.

Three types of working fluids were used including sodium chloride and boric acid with various concentrations (10^{-2} M, 10^{-3} M, 10^{-4} M and 10^{-5} M) as well as deionized water.

2.3.2 Experimental setup

The micro-PIV setup consists of four main components: an illumination system, an optical system, a coupled charge device (CCD) camera and a control system. The control system consists of a peripheral component interface (PCI) card, and its corresponding software is implemented in a personal computer. The computer can control and synchronize all actions related to illumination and image recording. The schematic of the setup is illustrated in Figure 2.2.

Particles were imaged using an epifluorescent microscope (Nikon TE2000-S) with a 20× objective lens having a numerical aperture (NA) of 0.45. An interline transfer

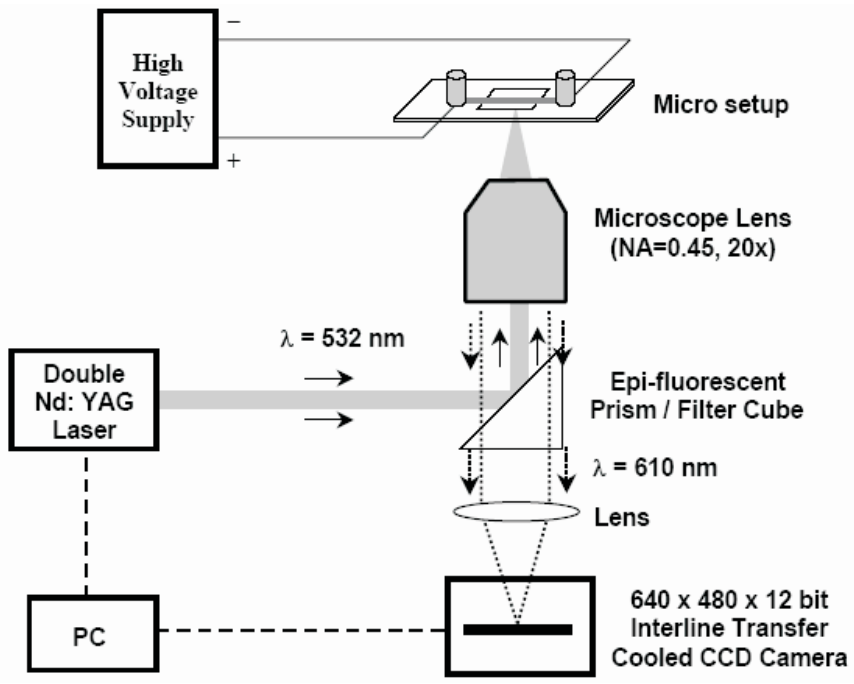

Figure 2.2 Schematic of the micro-PIV setup. The PC controls and synchronizes the lasers for illumination, the CCD camera for image recording, and the high voltage switch for turning on the high voltage supply.

CCD camera (Sony ICX 084) was used for recording the images. The resolution of the camera is 640 pixels × 480 pixels, with 12 bits grayscale. The active area of the CCD sensor is 6.3 mm × 4.8 mm. The minimum inter-frame transfer time, and thus the fastest time delay for the two PIV images, is $\Delta t_{\mathrm{PIV}} = 500$ μs. To ensure that the CCD camera is working at its optimum temperature of −15 °C, a cooling system is integrated in the CCD camera. In the mode of double exposure in double frames, the camera records two frames of the flow fields and then digitizes them in the same image buffer.

2.4 Results and Discussion

2.4.1 Micro-PIV images and particle velocity data

With the objective lens focusing on the mid-plane (*i.e.*, $y = 0$) of the rectangular channel as shown in Figure 2.1, the micro-PIV was used to measure the particle velocity

distributions in both the open- and closed-end channels. The images acquired from micro-PIV measurements were then evaluated with PIVview software (PivTec GmbH) to obtain the particle velocity data. For example, the vector plots of the particles' velocity distributions in deionized water are shown in Figure 2.3. Extracting the velocity data and averaging the values along the flowing direction, the averaged velocity values are plotted in Figure 2.4.

2.4.2 Least-square analysis

With the experimental data, the least-square analysis was used to determine the values of the fitted zeta potentials of both the particles and the channel surface by minimizing the sum of the square of the errors between the meausured and predicted particle mobility.

Along the lateral (x-axis) direction of the channel, it is assumed that the measured average particle's mobility at the ith position in the open-end channel as $\mu_{\mathrm{p-open},\,i}$ and the measured average particle's mobility at the ith position in the closed-end channel as $\mu_{\mathrm{p-closed},\,i}$. Applying the least-square method, we introduce the least-square function S as

$$S = \sum_{i\,=\,1}^{N} \left[\left(\mu_{\mathrm{p-closed},\,i} - \mu_{\mathrm{p-closed}}\right)^2 + \left(\mu_{\mathrm{p-open},\,i} - \mu_{\mathrm{p-open}}\right)^2 \right] \tag{2.28}$$

where N is the number of the measured points along the lateral direction of the mid-plane of the channel. Thus, the best-fitted values of the two zeta potentials, ζ_{w} and ζ_{p} can be obtained by minimizing the value of S. Substituting Eqs. (2.24) and (2.25) into Eq. (2.28), we know that the derivatives of function S with aspect to ζ_{w} and ζ_{p} should be equal to zero

$$\frac{\partial S}{\partial \zeta_{\mathrm{w}}} = \sum_{i\,=\,1}^{N} \left[2\left(\mu_{\mathrm{p-closed},\,i} - \mu_{\mathrm{p-closed}}\right)\left(-H\left(x_i\right)\right) + 2\left(\mu_{\mathrm{p-open},\,i} - \mu_{\mathrm{open}}\right)\left(-F\right) \right] = 0 \tag{2.29}$$

$$\frac{\partial S}{\partial \zeta_{\mathrm{p}}} = \sum_{i\,=\,1}^{N} \left[2\left(\mu_{\mathrm{p-closed},\,i} - \mu_{\mathrm{p-closed}}\right)\left(-G\right) + 2\left(\mu_{\mathrm{p-open},\,i} - \mu_{\mathrm{open}}\right)\left(-G\right) \right] = 0 \tag{2.30}$$

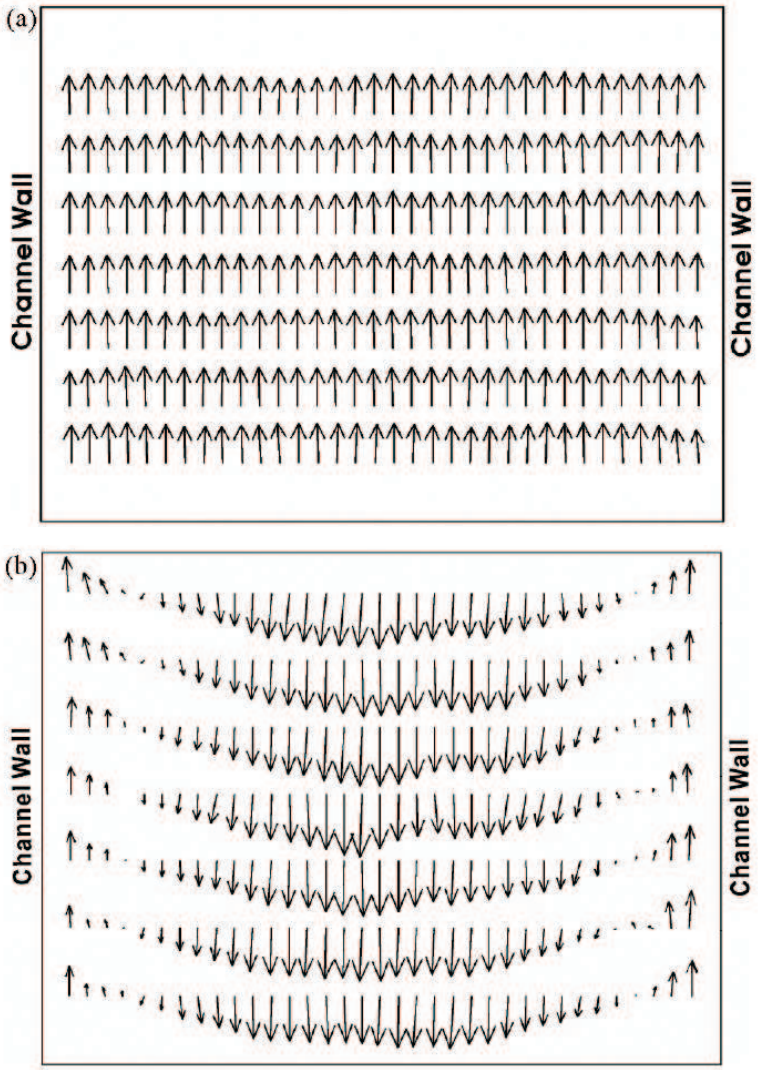

Figure 2.3 Micro-PIV measurement of the velocity distributions of the 930 nm polysterene fluorescent tracer particles in deionized water in (a) an open-end rectangular microchannel, and (b) a closed-end rectangular channel. The channel is made of borosilicate glass and has a length of 4 cm. Both the channel width and height are 300 μm (inner dimension). The electric field direction is imposed towards up and has a strength of 100 V/cm.

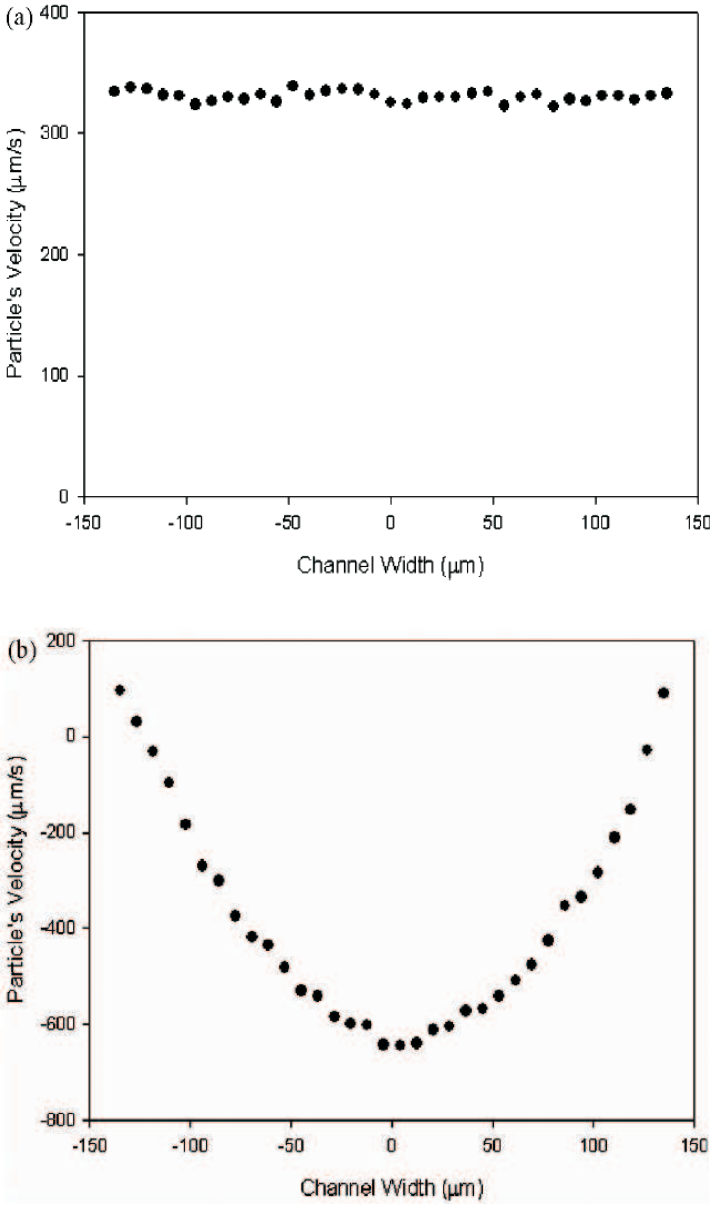

Figure 2.4 Plots for velocity data of the 930 nm polysterne fluoresecnt tracer particles in deionized water in (a) an open-end rectangular microchannel, and (b) a closed-end rectangular channel. Other parameters are the same as those specified in Figure 2.3.

Rearranging Eqs. (2.29) and (2.30) and making use of Eqs. (2.24) and (2.25), we obtain

$$\zeta_{\mathrm{w}} \sum_{i=1}^{N} \left[F + H\left(x_i\right)\right] + \zeta_{\mathrm{p}} \left(2NG\right) = \sum_{i=1}^{N} \left(\mu_{\mathrm{p-open},\,i} + \mu_{\mathrm{p-closed},\,i}\right) \tag{2.31}$$

$$\begin{aligned} \zeta_{\mathrm{w}} \sum_{i=1}^{N} \left[F^2 + \left(H\left(x_i\right)\right)^2\right] + \zeta_{\mathrm{p}} \sum_{i=1}^{N} \left[G\left(F + H\left(x_i\right)\right)\right] \\ = \sum_{i=1}^{N} \left[F\mu_{\mathrm{p-open},\,i} + H\left(x_i\right)\mu_{\mathrm{p-closed},\,i}\right] \end{aligned} \tag{2.32}$$

It is convenient to express Eqs. (2.31) and (2.32) in the matrix form

$$\begin{aligned} &\begin{bmatrix} \sum\limits_{i=1}^{N} \left[F + H\left(x_i\right)\right] & 2NG \\ \sum\limits_{i=1}^{N} \left[F^2 + \left(H\left(x_i\right)\right)^2\right] & \sum\limits_{i=1}^{N} \left[G\left(F + H\left(x_i\right)\right)\right] \end{bmatrix} \begin{bmatrix} \zeta_{\mathrm{w}} \\ \zeta_{\mathrm{p}} \end{bmatrix} \\ &\qquad = \begin{bmatrix} \sum\limits_{i=1}^{N} \left(\mu_{\mathrm{p-open},\,i} + \mu_{\mathrm{p-closed},\,i}\right) \\ \sum\limits_{i=1}^{N} \left[F\mu_{\mathrm{p-open},\,i} + H\left(x_i\right)\mu_{\mathrm{p-closed},\,i}\right] \end{bmatrix} \end{aligned} \tag{2.33}$$

Introducing

$$A = \begin{bmatrix} \sum\limits_{i=1}^{N} \left[F + H\left(x_i\right)\right] & 2NG \\ \sum\limits_{i=1}^{N} \left[F^2 + \left(H\left(x_i\right)\right)^2\right] & \sum\limits_{i=1}^{N} \left[G\left(F + H\left(x_i\right)\right)\right] \end{bmatrix} \tag{2.34}$$

and

$$B = \begin{bmatrix} \sum\limits_{i=1}^{N} \left(\mu_{\mathrm{p-open},\,i} + \mu_{\mathrm{p-closed},\,i}\right) \\ \sum\limits_{i=1}^{N} \left[F\mu_{\mathrm{p-open},\,i} + H\left(x_i\right)\mu_{\mathrm{p-closed},\,i}\right] \end{bmatrix} \tag{2.35}$$

we get

$$\begin{bmatrix} \zeta_{\mathrm{w}} \\ \zeta_{\mathrm{p}} \end{bmatrix} = A^{-1}B \tag{2.36}$$

With the measured data for $\mu_{\mathrm{p-open},\,i}$ and $\mu_{\mathrm{p-closed},\,i}$, A and B are known matrices. Using Eq. (2.36), we can simultaneously determine the two zeta potentials of the

Table 2.1 The zeta potentials (mV) of channel wall and tracer particles in different electrolytes with various concentrations (M).

Electrolytes	10^{-5} M	10^{-4} M	10^{-3} M	10^{-2} M
Sodium Chloride (NaCl)	$\zeta_w = -59 \pm 5$ $\zeta_p = -36 \pm 4$	$\zeta_w = -46 \pm 5$ $\zeta_p = -29 \pm 7$	$\zeta_w = -27 \pm 5$ $\zeta_p = -23 \pm 6$	$\zeta_w = -16 \pm 6$ $\zeta_p = -17 \pm 5$
Boric Acid ($H_2B_4O_7$)	$\zeta_w = -46 \pm 5$ $\zeta_p = -29 \pm 4$	$\zeta_w = -29 \pm 5$ $\zeta_p = -29 \pm 6$	$\zeta_w = -19 \pm 4$ $\zeta_p = -21 \pm 7$	$\zeta_w = -10 \pm 6$ $\zeta_p = -13 \pm 5$

channel surface and the tracer particles in deionized water as $\zeta_w = -62 \pm 6$ mV and $\zeta_p = -37 \pm 4$ mV, respectively. Furthermore, the same method was used to determine the zeta potentials in the sodium chloride and boric acid solutions with various concentrations. The experimental data are summarized in Table 2.1. We plot the zeta potential data versus the electrolyte concentration and present them in Figure 2.5. It is noted that all the zeta potentials are negative. Furthermore, it can be observed that the higher the electrolyte concentration, the smaller the absolute value of zeta potentials will be. This tendency is common for the zeta potentials of glass or polymer surfaces in aqueous solutions such as NaCl. Using the streaming potential technique, Gu and Li (2000) measured the zeta potential of glass surface in contact with different aqueous solutions of various concentrations. For NaCl solutions, they reported the zeta potential values, ranging from -20 mV to -60 mV, which are in good agreement with our data obtained in the present work.

2.4.3 Measurement errors due to Brownian motion

In micro-PIV measurement, the major uncertainty is due to the Brownian motion of tracer particles. In particular, the Brownian motion plays an important role when submicron tracer particles are used in PIV experiments with flow velocities of less than 1 mm/s. According to Einstein (1905), the Brownian motion induced random velocity can be estimated from

$$u_B = \sqrt{\frac{2D}{\Delta t_{PIV}}} \tag{2.37}$$

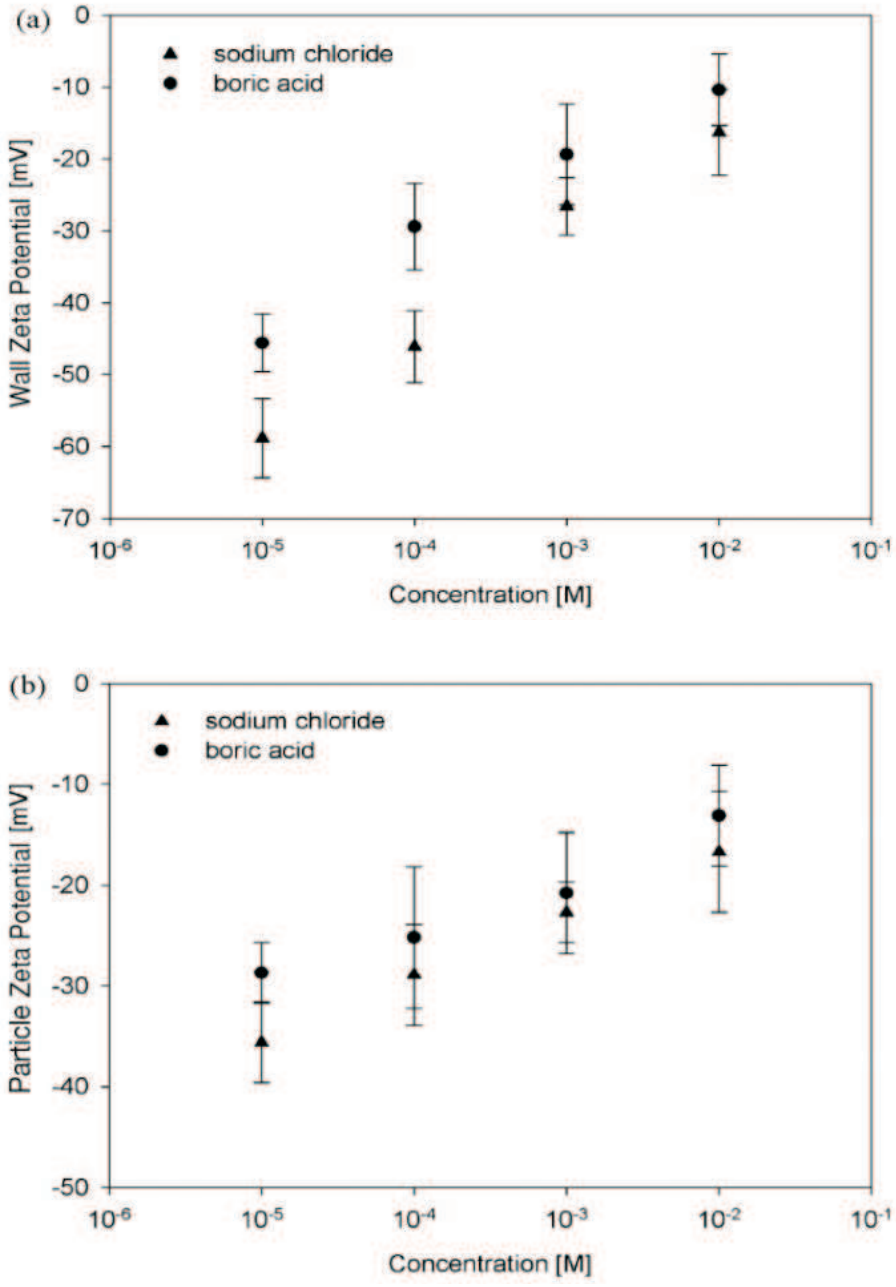

Figure 2.5 Measured zeta potentials versus solution concentration (mole/liter or M) of the sodium chloride and boric acid electrolytes for (a) the microchannel surface, and (b) the tracer particles.

The mass diffusivity of dilute tracer particles suspended in water is given by the Einstein-Stokes equation expressed as (Probstein, 1994)

$$D = \frac{k_\mathrm{b} T}{6\pi\mu a} \tag{2.38}$$

where k_b is Boltzmann's constant and is the absolute temperature of the fluid. Given the tracer particles of $a = 465$ nm, room temperature $T = 298$ K and the PIV exposure time $\Delta t_\mathrm{PIV} = 500$ μs, the Brownian velocity is estimated as 46 μm/s. The Brownian motion is the main source of errors of the velocity measurements, from which the electrokinetic mobilities are determined. Due to the linear relationship between the mobility and the zeta potential, the resulting error on the zeta potentials due to the contribution of the Brownian motion is the same as the Brownian motion error.

2.5 Summary

With the micro-PIV technique, the steady-state EOF in open- and closed-end rectangular microchannels were characterized. The typical plug-like flow pattern in open-end channel and parabolic velocity profile in closed-end channel have been demonstrated. However, because the tracer particles are charged, the micro-PIV measured velocity of tracer particles is a combination of the electroosomtic flow velocity and the particle's electrophoretic velocity. Hence, to retrieve the electroosmotic flow field, the particles' electrophoretic velocity has to be removed, which needs the information of particle zeta potential. Accordingly, a method is proposed to simultaneously determine the zeta potentials of the channel surface and the tracer particles in aqueous solutions.

Accurate measurement of the zeta potentials of tracer particles and microchannel surfaces is crucial to understanding of the stability of colloidal suspensions and transport of colloidal particles, obtaining micro-PIV measurements of electroosmotic flow fields, and quantifying the performance of electrokinetic microfluidic devices. The proposed method uses the micro-PIV technique to measure the steady velocity dis-

tributions of tracer particles in both open- and closed-end microchannels under the same water chemistry condition. As a result, the zeta potentials of the tracer particles and the channel surfaces can be determined using the least-square method to fit the micro-PIV measured velocity distributions of the tracer particles. This method was implemented to the open- and closed-end rectangular channels having 300 μm × 300 μm cross section and 4 cm in length under a 100 V/cm applied electric field. Measurements were carried out with a micro-PIV system to determine the zeta potentials of the channel surfaces and the fluorescent tracer particles in deionized water and sodium chloride and boric acid electrolytes of various concentrations. The obtained zeta potentials are in reasonable agreement with the data reported in the literature. Nonetheless, the proposed method avoids dealing with the problems associated with the stationary level in microelectrophoretic measurements, and allows for simultaneously determining the zeta potentials of the tracer particles and the microchannel surfaces using the micro-PIV technique.

Chapter 3

Start-up Transient Electrokinetic Flow in Microchannels

3.1 Introduction

As discussed in Chapter 1, the understanding of transient electroosmotic flow not only provides insights into the characteristics of electroosmotic flow but also is important to the practical development and operation of microfluidic devices. Experimentally, direct visualization of the dynamic electrokinetic flows is of fundamental importance as it provides insight into the underlying mechanisms of the development and stability of electrokinetic flows (Oddy *et al.*, 2001; Lin *et al.*, 2004). Furthermore, study of the dynamic aspects of the electrokinetic flow plays a crucial role in the development of relevant microfluidic technologies. According to Fan and Harrison (1994), the efficiency of electrophoretic separation is strongly dependent on the duration of electroosmotic injection, which in turn is related to the time evolution of electrokinetic flow. To reduce the contributions due to injection plug width and Joule heating, Jacobson *et al.* (1994 and 1998) proposed a high-speed electrophoretic separation mode to achieve separation within less than one millisecond, which is in the same order of the temporal development of electrokinetic flow.

However, because of the limitations of existing techniques, experimentally the tran-

sient measurement is usually difficult to realize. To our best knowledge, no study has been reported on measuring the velocity field of transient electrokinetic flows. This is mainly due to the fact that the time scale for the time evolution of electrokinetic flows in microfluidic channels is in the order of milliseconds, which is too rapid for the relatively low frame rates of the state-of-the-art PIV cameras to capture.

In this chapter, a technique is developed to characterize the transient electrokinetic flow by using an ordinary PIV CCD camera. Experiments are conducted to measure the time evolution of electrokinetic flows in both open-end and closed-end rectangular microchannels. Utilizing such transient micro-PIV technique, a method is proposed to determine the electrophoretic mobility of the tracer particles and the zeta potential of the channel wall. Using the measured channel zeta potential, the theoretical predictions of the transient electroosmotic velocity fields are validated with the experimental data.

3.2 Mathematical Modeling of Electrokinetic Flow – Slip Velocity Approach

Study of the transient development of electrokinetic flows in both open-end and closed-end channels is of fundamental interest; the former is due to pure electroosmosis and the latter is due to a combination of the electroosmosis and the induced back-pressure gradient. From a practical viewpoint, a straight open-end channel is an essential part of microfluidic devices. For closed-end channels, they are traditionally used for the electrophoretic measurement to determine the particle's zeta potential. Recently, a promising application using the closed-end channel structure has been proposed for the development of electrokinetic microactuators (Marcos *et al.*, 2004b).

Consider a transient electroosmotic flow in a rectangular microchannel having a height, $2h$ and width, $2w$ shown in Figure 2.1. The liquid filled in the microchannel is assumed to be an incompressible, Newtonian, symmetric electrolyte of constant density, ρ, and viscosity, μ. The channel wall is uniformly charged with a zeta potential,

ζ. When an external electric field, E is applied along the axial direction of the channel, the liquid starts to move as a result of the interaction between the net charge density in the electric double layer (EDL) of the channel and the applied electric field. The driving force of electroosmotic flow is present only within the EDL. The typical thickness of an EDL is in the range of 1 to 100 nm; while the characteristic hydraulic diameter of microfluidic channels is of order 10 to 100 μm (Stone *et al.*, 2004; Erickson and Li, 2004). Because of such orders of magnitude difference, the electroosmotic velocity profile inside the EDL region becomes insignificant, and thus the electroosmotic flow can be considered to be induced by a moving wall with velocity (slip velocity) given by the Smoluchowski equation, $u_{\mathrm{s}} = -\frac{\varepsilon_0 \varepsilon_{\mathrm{r}} \zeta E}{\mu}$. In the literature, the fluid flow actuated by the moving boundary of the wall and driven by hydrodynamic shear stresses is referred to as the Stokes first problem (Telionis, 1981). More general discussions of the applicability of the slip velocity approach in electrokinetic flows are provided elsewhere (Cummings *et al.*, 2000; Santiago, 2001).

The following dimensionless parameters are introduced:

$$\overline{u} = \frac{u}{U} \quad \bar{t} = \frac{\mu}{\rho D_{\mathrm{h}}^2} t \quad X = \frac{x}{D_{\mathrm{h}}} \quad Y = \frac{y}{D_{\mathrm{h}}} \quad Z = \frac{z}{D_{\mathrm{h}} \mathrm{Re}} \quad \bar{P} = \frac{p}{\rho U^2} \tag{3.1}$$

where U is the reference velocity, $D_{\mathrm{h}} = \frac{4wh}{w+h}$ is the hydraulic diameter of the rectangular channel, and $\mathrm{Re} = \frac{\rho D_{\mathrm{h}} U}{\mu}$ is the reference Reynolds number. Using the slip velocity approach, the transient velocity profile of a fully-developed electrokinetic flow is governed by the Stokes equation, in a dimensionless form, expressed as (Yang, 2002)

$$\frac{\partial \bar{u}}{\partial \bar{t}} = \frac{\partial^2 \bar{u}}{\partial X^2} + \frac{\partial^2 \bar{u}}{\partial Y^2} - \frac{\mathrm{d}\bar{P}}{\mathrm{d}Z} \tag{3.2}$$

The appropriate initial and boundary conditions applicable to Eq. (3.2) are

$$\bar{u}(X, Y, \bar{t})|_{\bar{t}=0} = 0 \tag{3.3}$$

$$\bar{u}\,\big|_{X=w/D_{\mathrm{h}}} = \bar{u}_{\mathrm{s}} \qquad \bar{u}\,\big|_{Y=h/D_{\mathrm{h}}} = \bar{u}_{\mathrm{s}} \tag{3.4}$$

$$\left.\frac{\partial \bar{u}}{\partial X}\right|_{X=0} = 0 \qquad \left.\frac{\partial \bar{u}}{\partial Y}\right|_{Y=0} = 0 \tag{3.5}$$

where $\bar{u}_{\mathrm{s}} = \frac{u_{\mathrm{s}}}{U} = -\frac{\varepsilon_0 \varepsilon_{\mathrm{r}} \zeta E}{\mu U}$. Here, two cases are considered:

Case 1: Transient electroosmotic flow field in an open-end rectangular microchannel

In this situation, $\frac{\mathrm{d}\bar{P}}{\mathrm{d}Z} \equiv 0$, because no external pressure is applied. Using the separation variables method, the solution of Eq. (3.2) is given by

$$\bar{u}(X, Y, \bar{t}) = \bar{u}_{\mathrm{s}} - \frac{16\bar{u}_{\mathrm{s}}}{\pi^2} \sum_{m=1}^{\infty} \sum_{n=1}^{\infty} \frac{(-1)^{m+n} \cos(\alpha_m X) \cos(\beta_n Y) \, \mathrm{e}^{-T_{mn}\bar{t}}}{(2m-1)(2n-1)} \tag{3.6}$$

where $\alpha_m = \left(\frac{2m-1}{2}\right) \frac{D_{\mathrm{h}}}{w}\pi$, $\beta_n = \left(\frac{2n-1}{2}\right) \frac{D_{\mathrm{h}}}{h}\pi$ and $T_{mn} = \alpha_m^2 + \beta_n^2$.

Case 2: Transient electroosmotic flow field in a closed-end rectangular microchannel

Due to the closed-end structure, an inner backpressure gradient $\frac{\mathrm{d}\bar{P}}{\mathrm{d}Z}$ (a function of $\bar{t}$ only under assumption of an infinitely extended channel) is induced to fulfill the condition of the zero net flow rates, which mathematically is expressed as

$$\int_{X=-w/D_{\mathrm{h}}}^{w/D_{\mathrm{h}}} \int_{Y=-h/D_{\mathrm{h}}}^{h/D_{\mathrm{h}}} \bar{u}(X, Y, \bar{t}) \mathrm{d}X \mathrm{d}Y = 0 \tag{3.7}$$

Using the Green's function formulation (Ozisik, 1993) and Laplace transform (Doetsch and Nader, 1970), we solve the problem as below. Introducing

$$\bar{v} = \bar{u} - \bar{u}_{\mathrm{s}} \tag{3.8}$$

we can rewrite Eq. (3.2) as

$$\frac{\partial \bar{v}}{\partial \bar{t}} = \frac{\partial^2 \bar{v}}{\partial X^2} + \frac{\partial^2 \bar{v}}{\partial Y^2} - \frac{\mathrm{d}\bar{P}}{\mathrm{d}Z} \tag{3.9}$$

with the initial condition and boundary conditions

$$\bar{v}(X, Y, 0) = -\bar{u}_{\mathrm{s}} \tag{3.10}$$

$$\bar{v}\big|_{X=w/D_{\mathrm{h}}} = 0 \qquad \bar{v}\big|_{Y=h/D_{\mathrm{h}}} = 0 \tag{3.11}$$

$$\left.\frac{\partial \bar{v}}{\partial X}\right|_{X=0} = 0 \qquad \left.\frac{\partial \bar{v}}{\partial Y}\right|_{Y=0} = 0 \tag{3.12}$$

According to the Green's function method (Ozisik, 1993), the solution of Eq. (3.9) subjected to the initial and boundary conditions given in Eqs. (3.10) – (3.12) can be explicitly expressed as

$$\begin{aligned}\bar{v}(X,Y,\bar{t}) = &\int_{\tau=0}^{\bar{t}} \mathrm{d}\tau \int_{X'=0}^{w/D_\mathrm{h}} \int_{Y'=0}^{h/D_\mathrm{h}} G(X,Y,\bar{t}\,|X',Y',\tau)\left(-\frac{\mathrm{d}\bar{P}}{\mathrm{d}Z}\right)\mathrm{d}X'\mathrm{d}Y' \\ &+ \int_{X'=0}^{w/D_\mathrm{h}} \int_{Y'=0}^{h/D_\mathrm{h}} G(X,Y,\bar{t}\,|X',Y',\tau)\,|_{\tau=0}\,(-\bar{u}_\mathrm{s})\,\mathrm{d}X'\mathrm{d}Y'\end{aligned} \tag{3.13}$$

Here, the Green's function $G(X,Y,\bar{t}\,|X',Y',\tau)$ can be obtained by using the separation of variables method. The expression for $G(X,Y,\bar{t}\,|X',Y',\tau)$ is given by

$$\begin{aligned}G(X,Y,\bar{t}\,|X',Y',\tau) = &\frac{4D_\mathrm{h}^2}{wh}\sum_{m=1}^{\infty}\sum_{n=1}^{\infty}\cos(\alpha_m X)\cos(\alpha_m X') \\ &\times \cos(\beta_n Y)\cos(\beta_n Y')\,\mathrm{e}^{-T_{mn}\,(\bar{t}-\tau)}\end{aligned} \tag{3.14}$$

Substituting Eq. (3.14) into Eq. (3.13) and carrying out the integration, we can get

$$\begin{aligned}\bar{v}\,(X,Y,\bar{t}) = &-\frac{16}{\pi^2}\sum_{m=1}^{\infty}\sum_{n=1}^{\infty}\frac{(-1)^{m+n}\cos(\alpha_m X)\cos(\beta_n Y)}{(2m-1)(2n-1)} \\ &\times \int_{\tau=0}^{\bar{t}} \exp\left[-T_{mn}\,(\bar{t}-\tau)\right]\frac{\mathrm{d}\bar{P}}{\mathrm{d}Z}(\tau)\,\mathrm{d}\tau \\ &-\frac{16\bar{u}_\mathrm{s}}{\pi^2}\sum_{m=1}^{\infty}\sum_{n=1}^{\infty}\frac{(-1)^{m+n}\cos(\alpha_m X)\cos(\beta_n Y)}{(2m-1)(2n-1)}\exp(-T_{mn}\bar{t})\end{aligned} \tag{3.15}$$

With Eq. (3.7) and the symmetric condition, we know

$$\int_{Y=0}^{h/D_\mathrm{h}} \int_{X=0}^{w/D_\mathrm{h}} \bar{u}\,(X,Y,\bar{t})\mathrm{d}X\mathrm{d}Y = 0 \tag{3.16}$$

Substituting Eq. (3.8) into Eq. (3.16), we find

$$\int_{Y=0}^{h/D_\mathrm{h}}\int_{X=0}^{w/D_\mathrm{h}}(\bar{v}+\bar{u}_\mathrm{s})\mathrm{d}X\mathrm{d}Y=\int_{Y=0}^{h/D_\mathrm{h}}\int_{X=0}^{w/D_\mathrm{h}}\bar{v}\mathrm{d}X\mathrm{d}Y+\bar{u}_\mathrm{s}\frac{wh}{D_\mathrm{h}^2}=0 \tag{3.17}$$

Substituting Eq. (3.15) into Eq. (3.17), we get

$$\begin{aligned}-\frac{64wh}{\pi^4 D_\mathrm{h}^2}\sum_{m=1}^{\infty}\sum_{n=1}^{\infty}\frac{1}{(2m-1)^2(2n-1)^2}\int_{\tau=0}^{\bar{t}}\exp\left[-T_{mn}(\bar{t}-\tau)\right]\frac{\mathrm{d}\bar{P}}{\mathrm{d}Z}(\tau)\,\mathrm{d}\tau\\ -\frac{64wh}{\pi^4 D_\mathrm{h}^2}\bar{u}_\mathrm{s}\sum_{m=1}^{\infty}\sum_{n=1}^{\infty}\frac{1}{(2m-1)^2(2n-1)^2}\exp\left(-T_{mn}\bar{t}\right)+\bar{u}_\mathrm{s}\frac{wh}{D_\mathrm{h}^2}=0\end{aligned} \tag{3.18}$$

Applying the Laplace transform on Eq. (3.18), we obtain the Laplace transform of the dimensionless pressure gradient as

$$\mathcal{L}\left[\frac{\mathrm{d}\bar{P}}{\mathrm{d}Z}(\bar{t})\right]=\frac{\pi^4\bar{u}_\mathrm{s}}{64}\frac{1}{\sum_{m=1}^{\infty}\sum_{n=1}^{\infty}\frac{1}{(2m-1)^2(2n-1)^2}\frac{s}{s+T_{mn}}}-\bar{u}_\mathrm{s} \tag{3.19}$$

where s is the corresponding variable of $\bar{t}$ in Laplace space. Substituting Eq. (3.15) into Eq. (3.8) and applying Laplace transform, and substituting Eq. (3.19), one can show that the Laplace transform of the velocity field is

$$\begin{aligned}\hat{u}(X,Y,s)&=\mathcal{L}\left[\bar{u}(X,Y,\bar{t})\right]\\ &=-\frac{16}{\pi^2}\sum_{m=1}^{\infty}\sum_{n=1}^{\infty}\frac{(-1)^{m+n}\cos(\alpha_m X)\cos(\beta_n Y)}{(2m-1)(2n-1)}\frac{1}{s+T_{mn}}\left\{\mathcal{L}\left[\frac{\mathrm{d}\bar{P}}{\mathrm{d}Z}(\bar{t})\right]+\bar{u}_\mathrm{s}\right\}+\frac{\bar{u}_\mathrm{s}}{s}\\ &=\frac{\bar{u}_\mathrm{s}}{s}-\frac{\pi^2\bar{u}_\mathrm{s}}{4}\frac{\sum_{m=1}^{\infty}\sum_{n=1}^{\infty}\frac{(-1)^{m+n}\cos(\alpha_m X)\cos(\beta_n Y)}{(2m-1)(2n-1)}\frac{1}{s+T_{mn}}}{\sum_{m=1}^{\infty}\sum_{n=1}^{\infty}\frac{1}{(2m-1)^2(2n-1)^2}\frac{s}{s+T_{mn}}}\end{aligned} \tag{3.20}$$

Since this Laplace transform function involves double infinite series, a numerical Laplace inversion method is sought to obtain $\bar{u}(X,Y,\bar{t})$ at a given time $\bar{t}$. In this study, we apply the fixed Talbot (FT) method (Abate and Valko, 2004; Appendix C) to $\hat{u}(X,Y,s)$

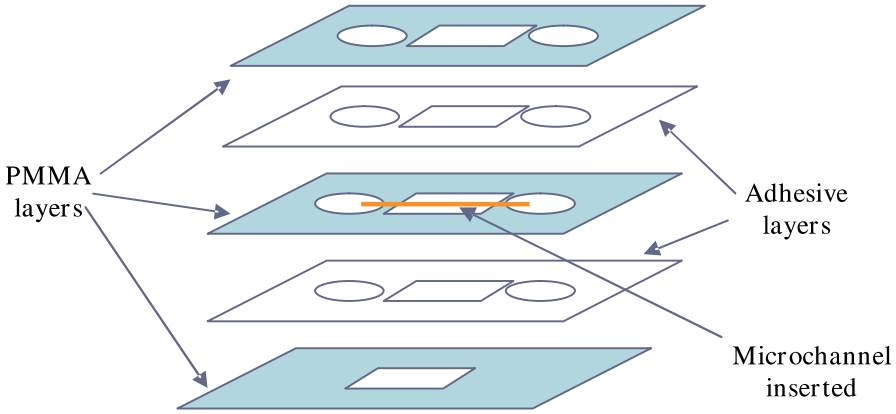

Figure 3.1 The sketch of the measurement cell. The layers are bounded together. Open-end channel connects with two reservoirs. Closed-end channel is made by sealing the two ends with Epoxy glue.

for the inversion of the Laplace transform

$$\bar{u}\left(X, Y, \bar{t}\right) = \mathcal{L}^{-1}\left[\hat{u}\left(X, Y, s\right)\right] \tag{3.21}$$

3.3 Experimental Section

3.3.1 Measurement cell and materials

A schematic of the measurement cell is shown in Figure 3.1. The measurement cell consists of a borosilicate glass microchannel (VitroCom), a polymer holder, and two reservoirs. The microchannel has a rectangular 300 μm × 300 μm cross section and is 4 cm in length. For the closed-end cell, Epoxy glue was used for sealing the two ends of the channel.

Fluorescent polystyrene particles of radius $a = 465$ nm (Duke Scientific Co.) were used as tracer particles for tracking the flow. The tracer particles have the excitation and emission wavelength of 540 nm and 610 nm, respectively. Prior to experiment, the cell was cleaned in an ultrasonic cleaner with a NaOH base solution and then flushed with deionized water. In all of the experiments, DI water and NaCl solutions (pH 6) of various concentrations were chosen as the working fluids. The number concentration of tracer particles was approximately about 2×10^9 particles per ml.

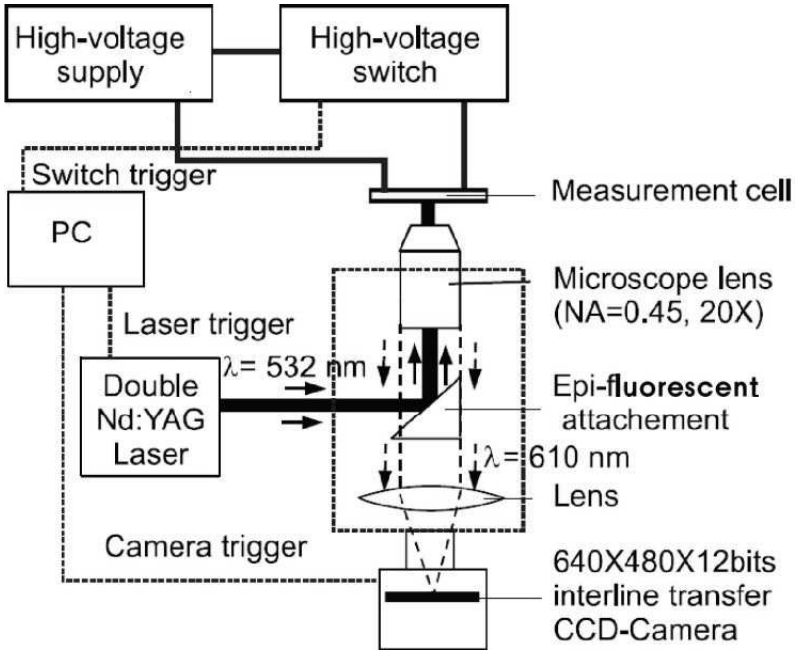

Figure 3.2 Schematic of the micro-PIV setup. The PC controls and synchronizes the lasers for illumination, CCD camera for image recording, and high voltage switch for turning on the high voltage supply.

A DC electric field was applied using platinum wire (Sigma Aldrich) electrodes inserted into the two reservoirs at the ends of the microchannel. A high-voltage power supply (PS350, Stanford Research Systems) was used to apply 800 V potential difference on the two electrodes, giving rise to a 200 V/cm strength of the applied DC field.

3.3.2 Experimental setup

A schematic of the experimental setup of the micro-PIV system is illustrated in Figure 3.2. The micro-PIV system is basicly the same as the one used in Chapter 2. However, since we take measurements during short transient time, we use the PIV system's function of synchronization. For precisely synchronizing the operation of the laser, CCD camera and high voltage supply, the internal triggering mode is applied in the experiment. In addition, an in-house made high-voltage switch is designed, and used in the transient measurements. In the next subsection, the detailed description of synchronization will be provided.

3.3.3 Measurement of transient electrokinetic flow

In order to capture the transient electrokinetic flows, we need to quantify the time scale for electrokinetic flow development. Previous analysis suggests that the characteristic response time of a charged particle to an applied electric field is of order (Minor *et al.*, 1997)

$$\tau_{\mathrm{ep}} = \mathcal{O}(a^2 \rho_{\mathrm{p}}/\mu) \tag{3.22}$$

where a and ρ are the radius and density of the particle, respectively, μ is the viscosity of electrolyte. In our experiment, latex particles of 930 nm in diameter and 1050 kg/m^3 in density were used, giving rise to a particle electrophoretic response time of order $\tau_{\mathrm{ep}} = \mathcal{O}(10^{-6})$ s. In the same fashion, the characteristic response time of an electroosmotic flow after switching on the electric field can be estimated from (Yang, 2002)

$$\tau_{\mathrm{eo}} = \mathcal{O}(D_{\mathrm{h}}^2 \rho/\mu) \tag{3.23}$$

For NaCl electrolyte in a typical microchannel of 100 μm in hydraulic diameter, we can estimate the electroosmotic flow relaxation time of order $\tau_{\mathrm{eo}} = \mathcal{O}(10^{-2})$ s. Such small response time poses a big challenge for the relatively low frame rates of the state-of-the-art PIV cameras. We implement a technique that essentially is similar to the one used by Meinhart and Zhang (2000) for characterizing the transient pressure-driven flow in an ink-jet nozzle. This technique allows for measuring the transient developing process of electroosmotic flow without the need of a high-speed camera, and it applies the phase lock method to capture image pairs at a given time by precise timing and synchronization among the high-voltage switching, laser illumination, and camera triggering to freeze particle image pairs at any time from the start of electrokinetic effects. It is achieved by use of an in-house built high voltage switch shown in Figure 3.3(a), which mainly consists of an insulated gate bipolar transistor (IGBT, IRG4PH40U) with a short switching time of 2×10^{-6} s, which is of the same order of magnitude as τ_{ep} by Eq. (3.22) but several orders smaller than τ_{eo} by Eq. (3.23). The switching time has been characterized by an oscilloscope as shown in Figure 3.3(b),

in which the triggering signal is applied on the Channel 1 and the Channel 2 presents the voltage drop down across the IBGT.

In operation, the micro-PIV system is set in internal triggering mode, under which an output signal (A8) from PCI card is sent to the high voltage switch to turn on the electric field. With the control software (Davis 6.2, LaVision Inc.), a programmable delay can be precisely generated in the range of $\tau_{\mathrm{ep}} < t \leq \tau_{\mathrm{eo}}$. The diagram of the control scheme is shown in Figure 3.4. Given any specified time in this range, the first particle image is recorded and then the second image is captured immediately after a time period of $\Delta t_{\mathrm{PIV}} = 500$ μs. Thus, the snapshot of particle velocity field at this time can be obtained by evaluating these two images with PIVview software (PivTec GmbH). As the flow development process is highly repeatable, the entire time evolution of the transient electrokinetic flow can be found through recoding back-to-back images. The resolution of this micro-PIV transient technique is constrained by the shortest PIV exposure time $\Delta t_{\mathrm{PIV}} = 0.5 \times 10^{-3}$ s, which is adequate enough for analyzing the temporal development of the electrokinetic flow of order $\tau_{\mathrm{eo}} = \mathcal{O}(10^{-2})$ s.

Focusing the objective lens on the mid-plane ($Y = 0$) of the rectangular channel, we took measurements at different times, $t = 0.5$ ms, 2 ms, 7 ms, 4 ms, 10 ms and 60 ms for the open-end channel, and $t = 0.5$ ms, 2 ms, and 5 ms for the closed-end channel. We captured at least 20 pairs for each given time. Correspondingly, the instantaneous velocity fields were obtained at these specified moments. Due to the relatively large reservoirs at the two ends of the capillary, pressure-driven velocity component is negligible during the short time of the transient process.

As discussed in Chapter 2, the major uncertainty in micro-PIV measurement is due to the Brownian motion of tracer particles. It has been reported in the literature that the measurement errors due to the particle's Brownian motion can be reduced by using the so-called ensemble correlation technique because the random Brownian motion errors are unbiased. The ensemble averaging technique was first proposed and demonstrated by Meinhart *et al.* (2000). Wereley *et al.* (2002) discussed the effect of Brownian motion and found that this technique can effectively reduce the

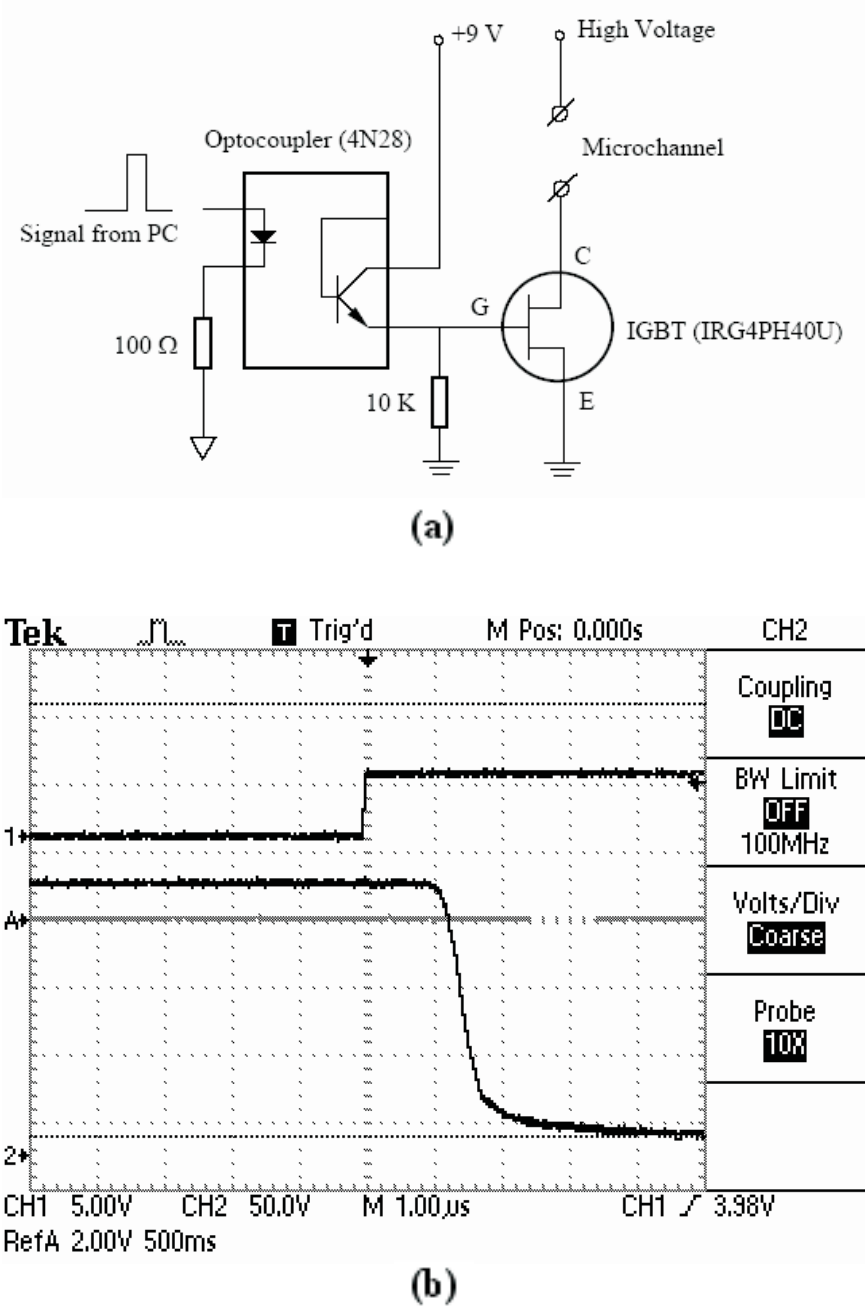

Figure 3.3 (a) Circuit diagram of the high voltage switch. This high voltage switch mainly consists of an ultra fast speed IGBT (IRG4PH40U) and an optocoupler (4N28). The optocoupler is used to separate the electrical connection between the PCI card and the high voltage power supply in order to avoid the high voltage shock on the controlling hardware in the PC. With the IGBT, the switch can sustain high voltage (up to 1200 V) and has a very short switching time (around 2 µs). (b) A captured screen of an oscilloscope for characterizing the switching time of the insulated gate bipolar transistor (IGBT).

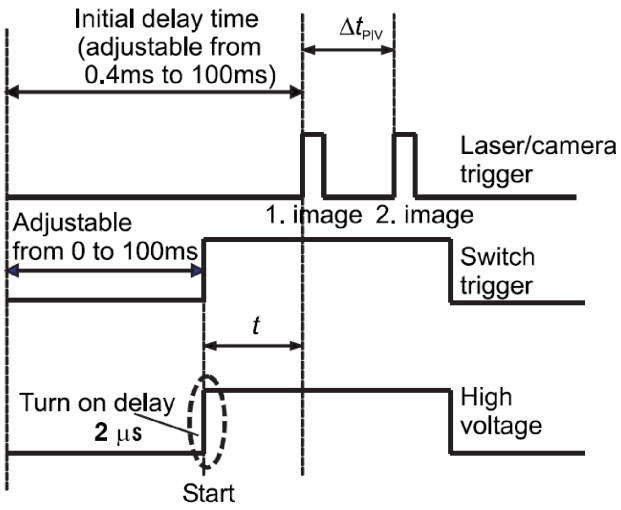

Figure 3.4 Timing and synchronization (not to scale). The control scheme is under internal triggering mode. The initial delay value is the time between PTU start and the first laser flash, and it is adjustable from 0.4 ms to 100 ms. The output signal A8 is a general purpose TTL-output to synchronize other external devices. Here the external device is a high voltage switch. The time of A8 signal is also adjustable, and the switch-on time of high voltage supply time can be altered before measurement by setting different time values.

errors due to the random distributed noises. Here an open-source program URAPIV (http://urapiv.wordpress.com/) is utilized to do the ensemble averaging by averaging the correlation matrices for all different image pairs at given times (phases).

3.4 Results and Discussion

3.4.1 Subtracting electrophoretic component from micro-PIV measurement

As pointed out earlier, the particle velocity, u_{p} evaluated from the micro-PIV measurement is a combination of two components, the particle electrophoretic velocity, u_{ep} and the electroosmotic velocity, u_{eo}:

$$u_{\mathrm{p}} = u_{\mathrm{ep}} + u_{\mathrm{eo}} \tag{3.24}$$

To obtain the electroosmotic velocity, a method is proposed to eliminate the contribution of particle electrophoresis in transient micro-PIV measurements. The method is based on the large difference between the response time scales of electrophoresis, τ_{ep} and electroosmotic flow, τ_{eo}. As analyzed earlier, the electrophoretic component can attain its steady-state velocity shortly after applying the electric field, say $t = 0.5\,\mathrm{ms} \gg \tau_{\mathrm{ep}} \sim \mathcal{O}(10^{-6})$ s; while the electroosmotic component is only developed in the neighborhood of the channel wall, and in the center part of the channel fluid still remains stationary because $t = 0.5\,\mathrm{ms} \ll \tau_{\mathrm{eo}} \sim \mathcal{O}(10^{-2})$ s. Thus, at this moment, the particle electrophoretic velocity is equal to the measured particle velocity in the center region of the channel, $u_{\mathrm{p}} = u_{\mathrm{ep}}$ as shown by a dotted box in Figure 3.5(a). After applying the ensemble averaging technique to the image pairs, the value of the particle electrophoretic velocity is obtained as $u_{\mathrm{ep}} = -890 \pm 21.6$ μm/s, in which the error is less than half of the estimated Brownian motion velocity value 46 μm/s. According to Eq. (3.24), the electroosmotic component (*i.e.*, electroosmotic flow field) can be extracted from the micro-PIV measured velocities, and is shown in Figure 3.5(b). In the same fashion, the electroosmotic flow fields at various times can be obtained, which are shown in Figure 3.6 for the open-end channel and in Figure 3.9 for the closed-end channel.

3.4.2 A Method of determining the zeta potential of the channel wall

The zeta potential of the channel wall is an important parameter for characterizing the channel wall materials and it offers a basis for design and control of microfluidic devices. According to Eq. (3.6) which expresses the transient electroosmotic velocity for the open-end microchannels, it can be shown that as $\bar{t} \to \infty$, Eq. (3.6) becomes

$$\bar{u}(X, Y, \bar{t})\,|_{\bar{t}\to\infty} = \bar{u}_{\mathrm{s}} = \mathrm{const} \tag{3.25}$$

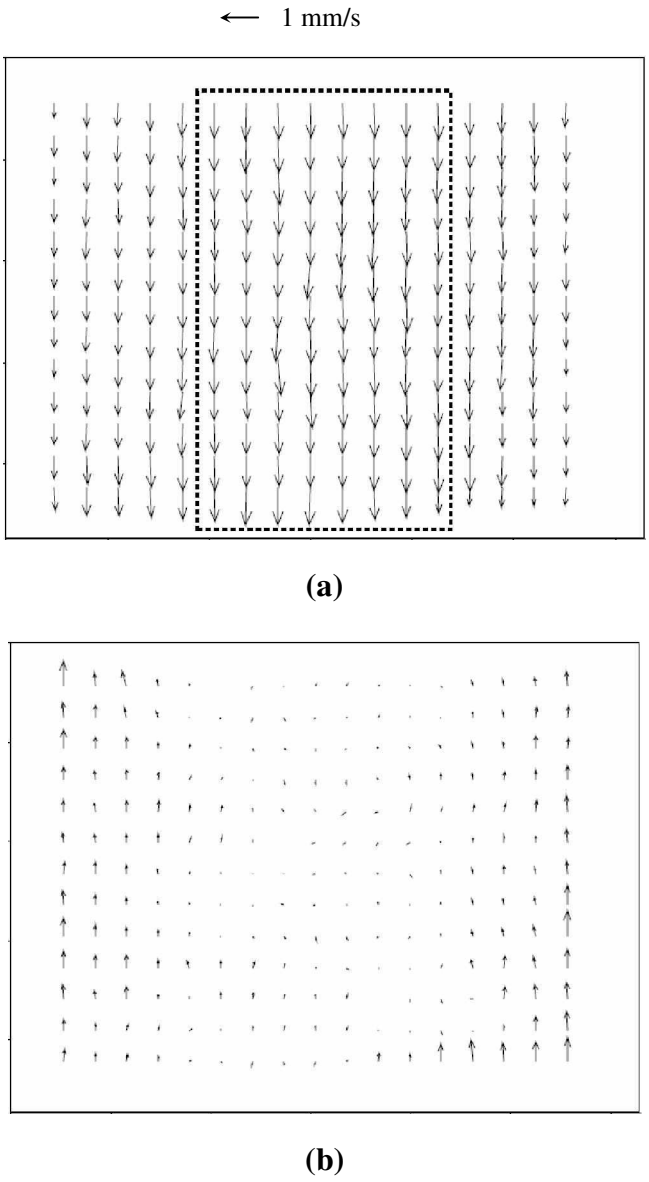

Figure 3.5 Transient velocity field measured at the mid-plane ($y = 0$) of an open-end channel filled with 1 mM NaCl electrolyte: (a) the velocity field of the 930 nm polystyrene fluorescent tracer particles at $t = 0.5$ ms; and (b) the corresponding electroosmotic flow field after subtracting the electrophoretic component from the measured particle velocity. The electroosmotic flow is developed near the channel wall region only and the fluid in the major center part of the channel still remains stationary. The electric field is imposed upwards and has a strength of 200 V/cm.

This suggests that the electroosmotic flow reaches its steady state which is given by the Smoluchowski equation expressed as

$$u_{\mathrm{eo}}\,|_{t\to\infty} = u_{\mathrm{s}} = -\frac{\varepsilon_0\varepsilon_{\mathrm{r}}\zeta_{\mathrm{w}}E}{\mu} \tag{3.26}$$

Experimentally, the steady-state electroosmotic velocity can be obtained at a sufficiently long time. For example, as shown in Figure 3.6 when $t = 60$ ms, the velocity profile exhibits a "plug-like" shape, suggesting the flow attains its at steady state. In our experiment, the measured electroosmotic velocity in steady-state is $u_{\mathrm{eo}} = 0.949$ mm/s. Then, the zeta potential of the channel wall can be determined using Eq. (3.16). Using the properties of water leads to a zeta potential of $\zeta_{\mathrm{w}} = -57.7$ mV, which agrees well with the value of -56 mV reported by Erickson *et al.* (2000).

On the one hand, this method avoids the difficulty associated with the electrophoretic measurement conducted at the stationary level. On the other hand, as the time of applying the electric field is rather short, Joule heat effects are minimized so that it is extremely useful in the situations where Joule heating associated problems are severe.

3.4.3 Comparisons of experimental data and theoretical results

Having obtained the zeta potential of the channel wall, the transient, 2D electroosmotic velocity distributions were computed using Eq. (3.6) for the open-end channel and Eq. (3.21) for the closed-end channel. It should be noted that the channel wall is in a charging process during the start-up transient EOF, and the zeta potential is also changing during this period. However, this characteristic response time is very short compared with the transient period. According to Bazant *et al.* (2004), the response time (Debye time) can be estimated by using $\tau_{\mathrm{ch}} = \lambda_{\mathrm{D}}^2/D$, where λ_{D} is the Debye screening length (in the order of $1 \sim 10$ nm), and D is the ionic diffusion constant (for

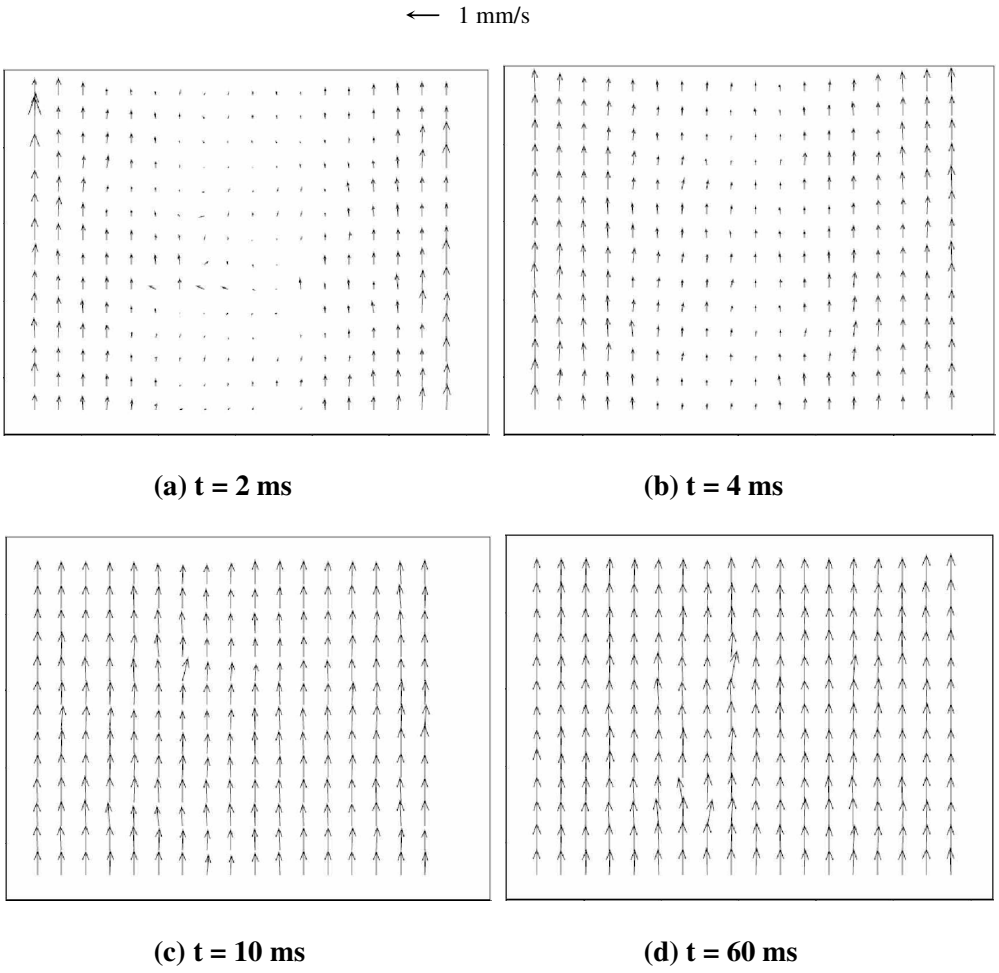

Figure 3.6 Vector plots for the time evolution of the electroosmotic velocity distributions at the mid-plane ($y = 0$) of an open-end rectangular channel for various times: (a) $t = 2$ ms, (b) $t = 4$ ms, (c) $t = 10$ ms, and (d) $t = 60$ ms. Other conditions are the same as those stated in Figure 3.5.

aqueous solutions, $D \sim 10^4$ $\mu m^2/s$). Hence the charging time is $\tau_{ch} \sim 1$ μs, which is much shorter than the start-up transient period of EOF (of order in 10 ms). Therefore, the time-dependent zeta potential has reached the steady value much earlier than the transient EOF starting up, and it is safe to calculate the velocity field using the zeta potential obtained in the measurement.

In calculation, the thermophysical and electrical properties of NaCl electrolytes were chosen the same as those of water, and they are the dielectric constant, $\varepsilon_r = 80$, density, $\rho = 1000$ kg/m^3, and viscosity, $\mu = 9 \times 10^{-4}$ Pa s. Figures 3.7 and 3.10 respectively depict a comparison between the experimental data and the predicted 2D velocity profiles at the mid-plane ($y = 0$) of the open-end and closed-end channels for various times. A good agreement is found between the experimentally measured transient electroosmotic velocity distributions and the theoretical predictions for electroosmotic flows in both open-end and closed-end microchannels.

It can also be observed that for the same channel dimensions and under the same experimental conditions, the time taken for the electroosmotic flow to develop in a closed-end channel is shorter than that in an open-end channel. This is because for the electroosmotic flow in open-end channels, the electroosmotic effect that only functions in the near-wall EDL region is the sole driving force, and then the momentum is transported to the rest of the channel through hydrodynamic shear stress. While for the electroosmotic flow in closed-end channels, the driving forces include not only the electroosmosis but also the induced backpressure gradient; the latter is applied upon the bulk flow region and thus speeds up the flow development.

It is known that the EDL is characterized by the Debye length, λ_D, and an expression for a symmetrical electrolyte of valence, z_v at room temperature 25 °C is given by (Masliyah, 1994)

$$\lambda_D = \frac{9.61 \times 10^{-9}}{(z_v^2 c)^{1/2}} \tag{3.27}$$

where the unit for λ_D is meter and the units for the bulk ionic concentration, c are mole m^{-3}. For NaCl solution, the Debye length is about 10 nm for the concentration of 1 mM, and correspondingly the EDL thickness is around $(3 \sim 5)\lambda_D$, which is 50 nm.

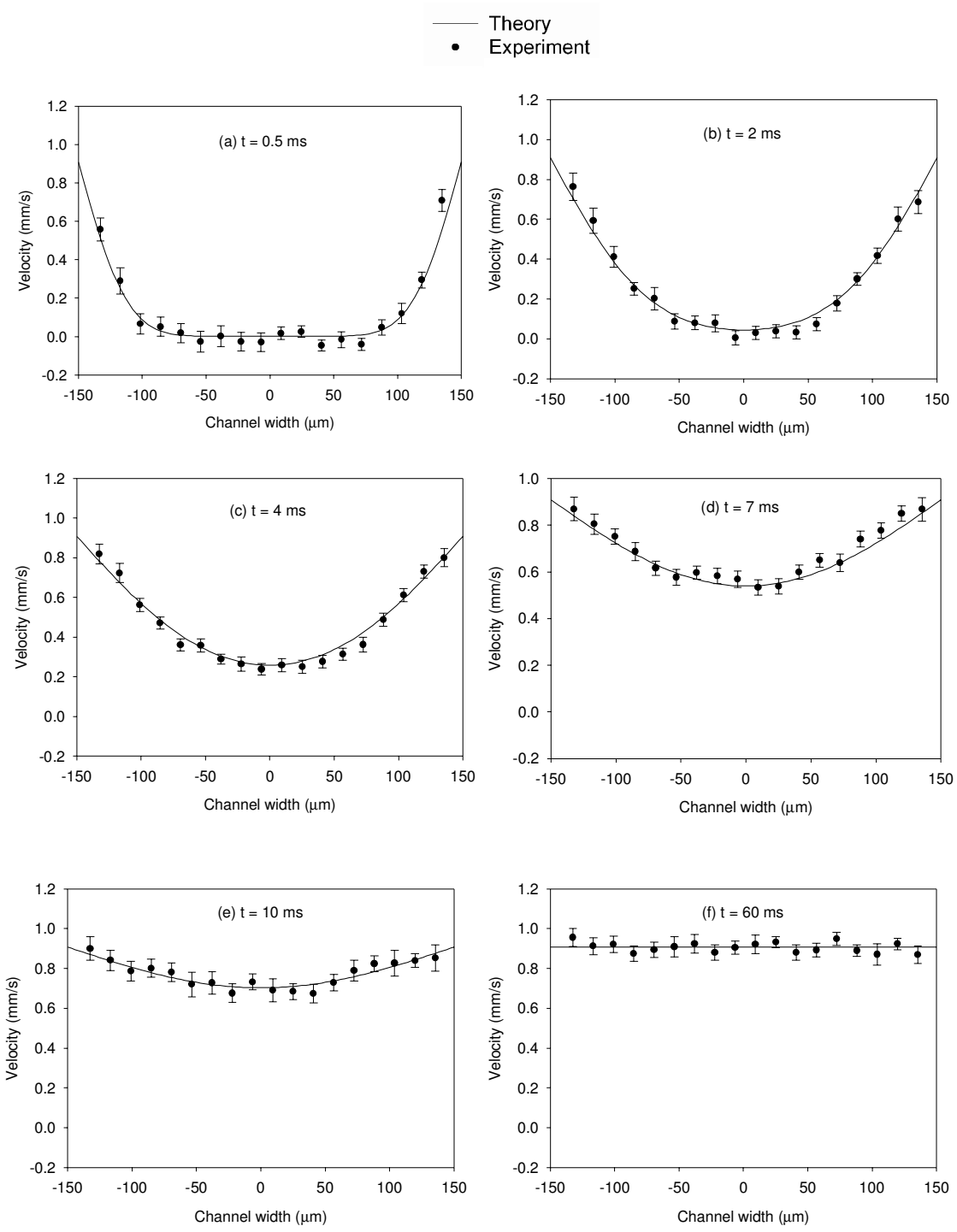

Figure 3.7 Comparison of the measured, lateral electroosmotic velocity distributions with ensemble correlation at the mid-plane ($y = 0$) of an open-end rectangular channel with the theoretical velocity profiles predicted on the basis of the slip velocity approach for various times: (a) $t = 0.5$ ms, (b) $t = 2$ ms, (c) $t = 4$ ms, (d) $t = 7$ ms, (e) $t = 10$ ms, and (f) $t = 60$ ms. Other conditions are the same as those stated in Figure 3.5. The experimental data represent the averaged electroosmotic velocities taken at various locations along the axial flow direction but within the mid-plane of the channel.

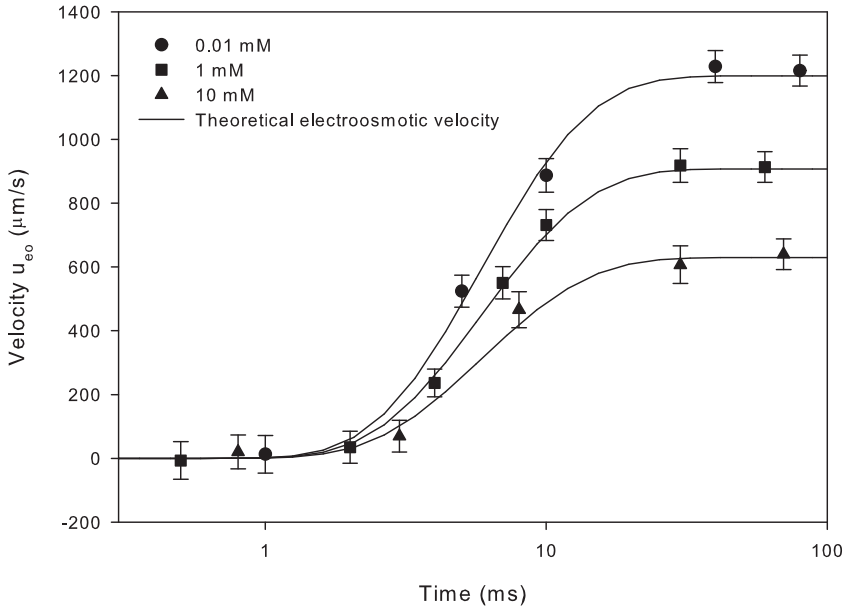

Figure 3.8 Transient response of electroosmotic velocity at the channel center for different NaCl concentrations. The symbols denote the experimental data. The lines represent the theoretical prediction of the electroosmotic velocity. The electric field strength is $E = 200$ V/cm.

Hence, it is obviously not feasible to use particles of 930 nm in diameter to track the flow and give the fluid velocity distributions in the EDL region. This explains why the current measurements did not extend to the region in the neighborhood of the channel wall. In fact, it poses a great challenge to directly measure the fluid velocity near the channel wall because of possible involvement of complex surface force interactions between the tracer particles and the channel wall, such as van der Waals and EDL forces (Unni and Yang, 2005). Sadr *et al.* (2004) developed a nano-particle image velocimetry (nano-PIV) technique to measure the near-wall velocity field in an electroosmotic flow, which is the first experimental verification of the analytical predictions that the region of uniform flow extends to within 100 nm of the wall and that the thickness of the EDL in EOF is much less than 100 nm.

However, from a microfluidic applications viewpoint, the characteristic size of the channel (*e.g.*, the hydraulic diameter) is much larger than the EDL thickness, suggesting that the contributions of velocity distributions in the EDL region, though of

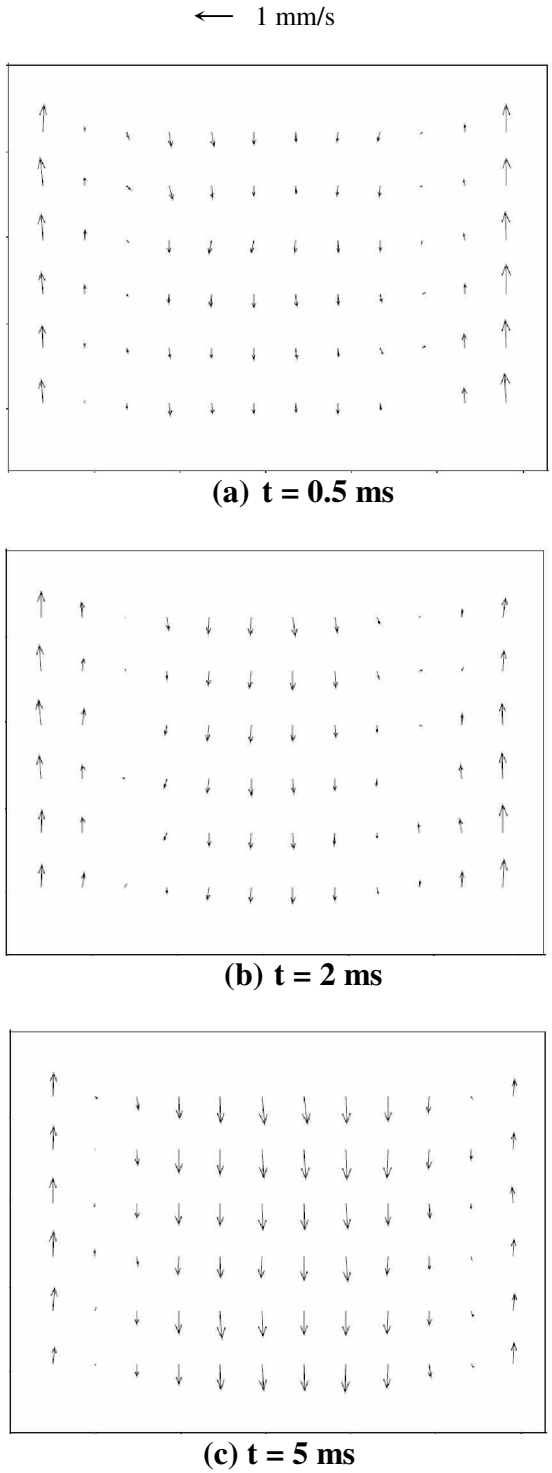

Figure 3.9 Vector plots for the time evolution of the electroosmotic velocity distributions at the mid-plane of a close-end rectangular channel filled with 1 mM NaCl electrolyte for various times: (a) $t = 0.5$ ms, (b) $t = 2$ ms, and (c) $t = 5$ ms. The electric field is imposed upwards and has a strength of 200 V/cm.

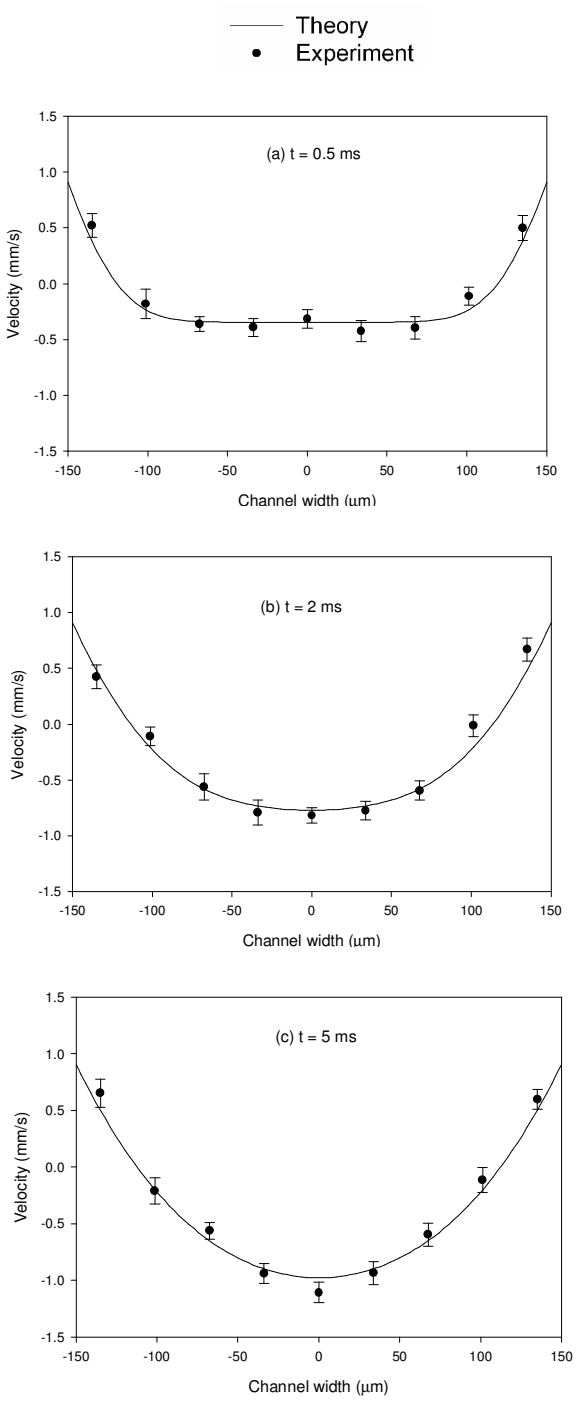

Figure 3.10 Comparison of the measured, lateral electroosmotic velocity distributions at the mid-plane ($y = 0$) of a closed-end rectangular channel with the theoretical velocity profiles predicted on the basis of the slip velocity approach for various times: (a) $t = 0.5$ ms, (b) $t = 2$ ms, and (c) $t = 5$ ms. Other conditions are the same as those stated in Figure 3.7. The experimental data represent the electroosmotic velocities taken at various locations along the axial flow direction but within the mid-plane of the channel.

fundamental interest, are not important. This can be seen from both Figure 3.7 and Figure 3.10, which show that using the transient micro-PIV technique described in this study the temporal development of the electroosmotic velocity field in the bulk flow region can be captured very well. In addition, the slip velocity approach, which neglects the detailed information inside the EDL region by assuming the slip velocity on the basis of the Smoluchowski equation, is verified by our experimental data.

In addition, we also measured the transient electroosmotic flow in the open-end channel for NaCl solutions with concentrations of 0.01 mM, 1 mM and 10 mM. Figure 3.8 depicts the transient response of the electroosmotic velocity in NaCl electrolyte of three different concentrations. The time axis is shown on a logarithmic scale. The theoretical results shown by the solid line were obtained based on the measured zeta potentials. It can be noted that the more dilute the NaCl electrolyte concentration, the higher the electroosmotic flow velocity and the wall zeta potential. Again, it is found that the theoretical predictions are in good accordance with the experimental data.

3.5 Summary

A phase locking based micro-PIV technique is proposed to investigate transient electroosmotic flow fields by using precise synchronization of different trigger signals for the laser, CCD camera, and in-house designed high-voltage switch. This technique allows for recoding two consecutive particle images at any time during the temporal development of electrokinetic flow so that the entire time evolution of electrokinetic flow can be obtained by putting together the recorded back-to-back images. This technique was implemented to study the transient electrokinetic flow in both open- and closed-end rectangular channels. Using the transient micro-PIV technique, a method, based on the large difference in the response time scales of the electrophoresis of tracer particles and the microchannel electroosmotic flow, was proposed to subtract the electrophoretic component of the particle velocity from the micro-PIV measured

data, and thus the transient electroosmotic flow fields were obtained. Furthermore, the zeta potential of the channel wall was also determined using the Smoluchowski equation from the measured steady-state electroosmotic velocity in the open-end channel. Using the ensemble averaging technique, the measurement errors due to Brownian motion have been reduced effectively. The method reported here allows for measuring the channel wall's zeta potential without dealing with the difficulty related to the so-called stationary level and is suitable for the situations where the Joule heating associated problems are severe.

In addition, using the slip velocity approach and the measured zeta potential, the theoretical predictions of the temporal development of electroosmotic flow in both open- and closed-end microchannels are found to agree with the experimental results, validating the slip velocity approach and the effective transient micro-PIV technique. To our best knowledge, this study reports the first measurement of transient electroosmotic flow fields and the first experimental verification of analytical predictions of the temporal development of electroosmotic flows. The transient micro-PIV technique presented in this study can be a useful tool to study the dynamic characteristics of the electroosmotic velocity field in microfluidic devices.

Chapter 4

Time-dependent Electroosmotic Flow in Microchannels due to Finite Reservoir Size Effect

4.1 Introduction

In electrokinetically-driven microfluidic applications, reservoirs are indispensable and have finite sizes. During operation processes, as the liquid level difference in reservoirs keeps changing as time elapses, a backpressure is generated. Thus, the flow in microfluidic channels actually exhibits a combination of the electroosmotic flow and the time-dependent induced backpressure-driven flow. The objective of this study is to examine how the reservoir size will affect the EOF in a microchannel.

Less attention has been paid to study the finite reservoir size effect on EOF. Yang *et al.* (2005) numerically investigated on the end effect in entry and exit regions. Zhang *et al.* (2004) studied the same problem by introducing a better method of determining the static pressures at the inlet and outlet of the microchannel. Their analyses show that such end effect is significant only when the ratio of channel length to channel hydraulic diameter is less than 10, but in most microfluidic devices, the ratio of channel length to lateral dimension is more than 100. Crabtree *et al.* (2001) reported an experimental

study of anomalies in microchip injection and separation due to the reservoir pressure effect. However, no systematic study has been reported on the effect of finite reservoir size on EOF in microchannels.

In this chapter, a model is presented to describe the effect of the finite reservoir size on electroosmotic flow in a rectangular microchannel. Important parameters that describe the effect of finite reservoir size on flow characteristics are discussed. A new concept termed as "effective pumping period" is introduced to characterize the reservoir size effect. The proposed model identifies the mechanisms of the finite-reservoir size effects and is verified by experiment using the micro-PIV technique. The results reported in this study can be used for facilitating the design of microfluidic devices.

4.2 Mathematical Model

4.2.1 EOF in a rectangular microchannel with reservoir size effects

As shown in Figure 2.1, a rectangular channel has a length l and a cross section $2w \times 2h$, and it is connected with two cylindrical reservoirs initially with a same liquid level. The liquid in the microchannel is assumed to be an incompressible, Newtonian, symmetric electrolyte of constant density, ρ, and dynamic viscosity, μ. Joule heating effect is assumed negligible (Tang *et al.*, 2003).

Surface tension effect on liquid level in the reservoir may cause a hydrostatic pressure (Crabtree *et al.*, 2001). However, since we choose two identical reservoirs, the Laplace pressure effect on the two reservoirs should be balanced each other (MacInnes *et al.*, 2003). The channel wall is uniformly charged with a zeta potential, ζ. When an external DC electric field $\boldsymbol{E}$ is applied along the channel axial direction, the liquid starts to move due to electroosmosis that is resulted from the interaction between the net charge density in the electric double layer (EDL) of channel and the applied electric field. The governing equations for the EOF field can be non-dimensionalized

by using

$$\bar{\boldsymbol{r}} = \boldsymbol{r}/D_\mathrm{h} \qquad \bar{t} = t/\tau_\mathrm{ch} \qquad \overline{\boldsymbol{V}} = \boldsymbol{V}/U \tag{4.1a}$$

$$\bar{p} = p/P_0 \qquad \overline{\nabla} = D_\mathrm{h}\nabla \qquad \overline{\nabla}^2 = D_\mathrm{h}^2\nabla^2 \tag{4.1b}$$

where $\boldsymbol{r}$, t, $\boldsymbol{V}$, and p are the position vector, time, local velocity vector, and pressure, respectively. These quantities are normalized using D_h, τ_ch, U, and $P_0 = \mu U/D_\mathrm{h}$, which are the microchannel hydraulic diameter, characteristic time scale, characteristic flow velocity, and characteristic pressure, respectively. Then one can write down the continuity equation,

$$\overline{\nabla} \cdot \overline{\boldsymbol{V}} = 0 \tag{4.2}$$

and the Navier-Stokes equation,

$$\mathrm{Re}\left[\frac{1}{\mathrm{St}}\frac{\partial \overline{\boldsymbol{V}}}{\partial \bar{t}} + (\overline{\boldsymbol{V}} \cdot \overline{\nabla})\overline{\boldsymbol{V}}\right] = -\overline{\nabla}\bar{p} + \overline{\boldsymbol{F}}_\mathrm{e} + \overline{\nabla}^2\overline{\boldsymbol{V}} \tag{4.3}$$

where $\mathrm{Re} = \rho U D_\mathrm{h}/\mu$ is the Reynolds number that characterizes the ratio of inertial force to viscous force, $\mathrm{St} = \tau_\mathrm{ch}U/D_\mathrm{h}$ is the Strouhal number that represents the ratio of the characteristic process time, τ_ch to the convective time, $\tau_\mathrm{c} = D_\mathrm{h}/U$ (Deen, 1998), and $\overline{\boldsymbol{F}}_\mathrm{e} = \frac{D_\mathrm{h}^2}{\mu U}\rho_\mathrm{e}\boldsymbol{E}$ is the non-dimensionless electrostatic body force due to the interaction between the net charge density in the EDL of channel, ρ_e and the applied electric field, $\boldsymbol{E}$. Consider that usually the microchannel hydraulic diameter and the characteristic flow velocity respectively are of order $D_\mathrm{h} = 100\,\mu\mathrm{m}$ and $U = 1$ mm/s, we can estimate Re of order 10^{-1}, showing a low Reynolds number flow and thus a negligible inertial term, $\mathrm{Re}(\overline{\boldsymbol{V}} \cdot \overline{\nabla})\overline{\boldsymbol{V}}$ in Eq. (4.3). Furthermore, for most microfluidic applications, the pumping time is of order $10^0 \sim 10^1$ s, the characteristic convective time scale is $\tau_\mathrm{c} = D_\mathrm{h}/U = 10^{-1}$ s, leading to the Strouhal number of order $\mathrm{St} = 10^1 \sim 10^2$. As a result, we can assume a pseudosteady flow by ignoring the transient term, $\frac{\mathrm{Re}}{\mathrm{St}}\frac{\partial \overline{\boldsymbol{V}}}{\partial \bar{t}}$ (Marcos *et al.*, 2005). Hence, Eq. (4.3) reduces to the Stokes equation expressed as

$$-\overline{\nabla}\bar{p} + \overline{\boldsymbol{F}}_\mathrm{e} + \overline{\nabla}^2\overline{\boldsymbol{V}} = 0 \tag{4.4}$$

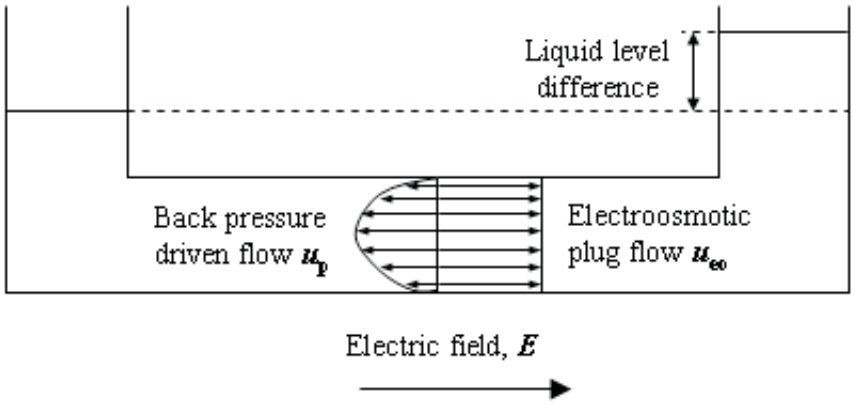

Figure 4.1 Superposition of electroosmotic flow and pressure-driven flow.

For a microchannel whose length dimension is much larger than its lateral dimensions, the flow in the channel can be considered as unidirectional; this implies that the flow is modeled as a fully-developed flow, namely $\partial u/\partial x = 0$, $v = 0$ and $w = 0$ in terms of Cartesian Coordinates. Furthermore, since the Stokes equation (*i.e.*, Eq. (4.4)) and its corresponding no slip boundary conditions are linear, we can treat the flow field as a superposition of two parts including the electroosmotic flow due to $\overline{\boldsymbol{F}}_{\mathrm{e}}$ and the pressure driven flow due to the induced backpressure, $\overline{\nabla}\bar{p}$ resulted from the liquid level difference in reservoirs, as shown in Figure 4.1. Hence one can write the expression for the flow field in dimensional form as (Deen, 1998)

$$u\left(x,y,t\right) = u_{\mathrm{eo}} + u_{\mathrm{p}}\left(x,y,t\right) \tag{4.5}$$

In Eq. (4.5), the electroosmotic flow field u_{eo} is steady, while the backpressure driven flow field $u_{\mathrm{p}}(x,y,t)$ is time-dependent because of the change of liquid level in the reservoirs with time.

In microfluidic systems, due to very thin EDL thickness compared to the microchannel dimension, the information of electroosmotic velocity profile inside the EDL region becomes insignificant, and thus one does not need to solve the Poisson-Boltzmann equation and the Stokes equation to obtain the electroosmotic flow field. Instead

the EOF can be considered as a flow induced by a moving wall with a velocity (slip velocity) given by Smoluchowski equation (Santiago, 2001),

$$u_{\mathrm{eo}} = -\frac{\varepsilon_0 \varepsilon_{\mathrm{r}} \zeta E}{\mu} \tag{4.6}$$

Using the Cartesian coordinates system shown in Figure 2.1, with assumption of the pseudosteady pressure-driven flow, the flow velocity profile is described by the well-known Poiseuille flow which in a rectangular channel is expressed as (Papanastasiou *et al.*, 2000; Appendix D)

$$u_{\mathrm{p}}(x,y,t) = \frac{h^2}{2\mu}\frac{\Delta p(t)}{l}\left[1-\left(\frac{y}{h}\right)^2 + 4\sum_{k=1}^{\infty}\frac{(-1)^k}{\alpha_k^3}\frac{\cosh\left(\frac{\alpha_k x}{h}\right)}{\cosh\left(\frac{\alpha_k w}{h}\right)}\cos\left(\frac{\alpha_k y}{h}\right)\right] \tag{4.7}$$

where $\alpha_k = (2k-1)\pi/2$ (here $k = 1, 2, \cdots$). $\Delta p(t)$ is the time-dependent pressure drop induced by change of the liquid levels in the reservoirs. Without knowing the induced backpressure, $\Delta p(t)$, one cannot compute the velocity profile expressed in Eq. (4.7).

4.2.2 Determination of the induced backpressure gradient

Similarly, the total flow rate in the channel also consists of two parts, the electroosmotic flow rate and the backpressure-driven flow rate. Then according to Eq. (4.5), the total flow rate can be expressed as

$$q(t) = q_0 - q_{\mathrm{p}}(t) \tag{4.8}$$

where "−" sign indicates that the induced backpressure-driven flow is always opposite to the electroosmotic flow. q_0 is the electroosmotic flow rate and is expressed as

$$q_0 = u_{\mathrm{eo}} A_{\mathrm{cross}} = -\frac{\varepsilon_0 \varepsilon_{\mathrm{r}} \zeta E}{\mu} 4wh \tag{4.9}$$

Integrating Eq. (4.7) over the cross-sectional area of the rectangular microchannel gives an expression for the volumetric flow rate in the induced pressure-driven flow as

$$q_{\mathrm{p}}(t)=\frac{4wh^{3}\Delta p(t)}{3\mu l}\left[1-\frac{6h}{w}\sum_{k=1}^{\infty}\frac{1}{\alpha_{k}^{5}}\tanh\left(\frac{\alpha_{k}w}{h}\right)\right] \tag{4.10}$$

For two identical reservoirs with radius R, and the cross section area is $A=\pi R^{2}$. Thus, the induced backpressure drop resulted from the change of fluid levels in the two reservoirs can be related to the total quantity of liquid transported during the pumping period from time zero to time t, and the correlation then can be expressed as

$$\Delta p(t)=\rho g\frac{2Q(t)}{A} \tag{4.11}$$

where $Q(t)$ is the total quantity of liquid transported at given time t and can also be expressed as

$$Q(t)=\int_{\tau=0}^{t}q(\tau)\mathrm{d}\tau \tag{4.12}$$

Substituting Eq. (4.11) into Eq. (4.10), we can obtain

$$q_{\mathrm{p}}(t)=\frac{8wh^{3}\rho g}{3\mu A l}\left[1-\frac{6h}{w}\sum_{k=1}^{\infty}\frac{1}{\alpha_{k}^{5}}\tanh\left(\frac{\alpha_{k}w}{h}\right)\right]Q(t) \tag{4.13}$$

Introducing a parameter,

$$C=\frac{8wh^{3}\rho g}{3\mu A l}\left[1-\frac{6h}{w}\sum_{k=1}^{\infty}\frac{1}{\alpha_{k}^{5}}\tanh\left(\frac{\alpha_{k}w}{h}\right)\right] \tag{4.14}$$

one can write

$$q_{\mathrm{p}}(t)=CQ(t) \tag{4.15}$$

Using Eqs. (4.8), (4.12) and (4.15), one can show the expression for the total flow rate

$$q(t)=q_{0}-C\int_{\tau=0}^{t}q(\tau)\mathrm{d}\tau \tag{4.16}$$

Eq. (4.16) is an integral equation. With the initial condition of $q\,(t=0)=q_0$, one can solve it to obtain the time-dependent flow rate,

$$q(t) = q_0 \exp(-Ct) \tag{4.17}$$

Substituting Eq. (4.17) into Eq. (4.12) yields an expression for the total quantity of liquid transported during the period of time zero to time t :

$$Q\,(t) = \frac{q_0}{C}\left[1 - \exp\left(-Ct\right)\right] \tag{4.18}$$

Putting Eq. (4.18) into Eq. (4.11), one can show that the induced backpressure gradient along the channel can be expressed as

$$\frac{\Delta p\,(t)}{l} = \frac{2\rho g q_0}{CAl}\left[1 - \exp\left(-Ct\right)\right] \tag{4.19}$$

With the pressure gradient obtained, one can determine the electroosmotic-backpressure driven velocity field using Eqs. (4.5) and (4.7).

4.2.3 Two important time parameters for electroosmotic pumping

4.2.3.1 Effective pumping period

According to Eq. (4.17), it can be observed that the volumetric flow rate exhibits an exponential decay with time. In fact, C defined in Eq. (4.14) is a characteristic parameter that depends on the channel cross section, w and h, channel length, l, and reservoir cross section area, A. We then can estimate the effective pumping period, t_{eff} as follows. Here we define the effective pumping period as the time at which the volumetric flow rate falls to 95% of q_0, and thus one can use Eq. (4.17) to obtain

$$t_{\text{eff}} = -\frac{\log\left(0.95\right)}{C} \approx \frac{0.05}{C} \tag{4.20}$$

The estimation value of $t_{\text{eff}} = 0.05/C$ can give a reference for efficient pumping in a microfluidic system.

4.2.3.2 Reverse flow starting time

At the channel centerline, when the backpressure induced flow overcomes the electroosmotic flow the reverse flow starts. Taking advantage of the analytical model presented in this study, we can determine the reverse flow starting time, t_{rev} at which the fluid velocity at the channel centerline ($y = z = 0$) should meet

$$|u_{\text{p}}(0, 0, t_{\text{rev}})| = |u_{\text{eo}}| \tag{4.21}$$

Together with Eqs. (4.7), (4.9), and (4.19), we can show that the expression for the reverse flow starting time,

$$t_{\text{rev}} = -\frac{1}{C}\log\left[1 - \frac{\mu C A l}{4\rho g w h^3}\frac{1}{1 + 4\sum_{k=1}^{\infty}\frac{(-1)^k}{\alpha_k^3\cosh(\alpha_k w/h)}}\right] \tag{4.22}$$

4.2.4 Simulation results and discussion

4.2.4.1 Volumetric flow rate

For analysis, we choose the following parameters: the half height and half width of the rectangular channel are $w = h = 150\,\mu\text{m}$, the channel length is $l = 4$ cm, the wall zeta potential of borosilicate glass channel is $\zeta = -62$ mV (Chapter 2), the electric strength is $E = 100$ V/cm, and the reservoir radii are $R = 1$ mm.

Figure 4.2 presents the volumetric flow rate and the pressure gradient versus time. It can be seen that both the volumetric flow rate and the induced backpressure gradient are dependent on time. A close examination of Figure 4.2 shows that in the early pumping stage, the curve for flow rate is flat, indicating the volumetric flow rate keeps unchanged. During this period, the change of the fluid level in the two reservoirs is so small that the induced pressure gradient is negligible. As a result, the flow field is

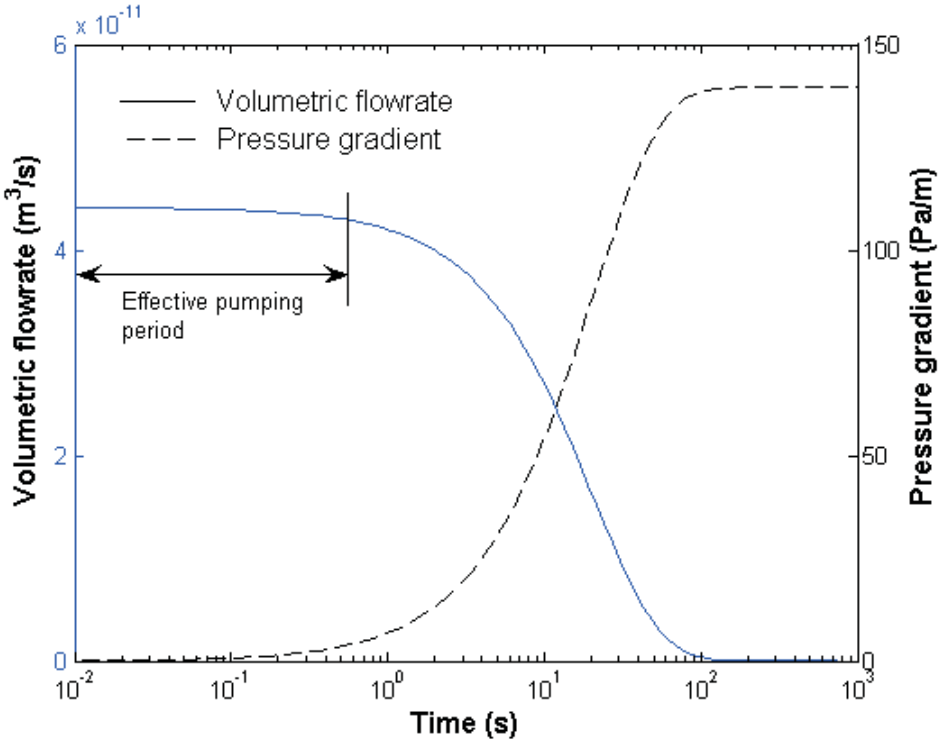

Figure 4.2 Volumetric flow rate and induced pressure gradient versus time.

dominated by EOF which, as shown in Eq. (4.9), is steady. Since the velocity profile can keep a "plug flow" during this period, we define it as the effective pumping period. After this effective pumping period, the volumetric flow rate decreases as the liquid level difference in the two reservoirs becomes large and thus the induced backpressure gradient increases. When the backpressure reaches its maximum, the total flow rate becomes zero, suggesting the electroosmotic flow is completely counterbalanced by the induced backpressure-driven flow.

Figure 4.3 shows the volumetric flow rate versus time for various reservoir radii. It can be seen that by enlarging the reservoir size, the period of "plug flow" (*i.e.*, the flat part of the curve) can be prolonged, demonstrating a decreasing effect of the backpressure-driven flow when increasing the reservoir size (radius). Figure 4.4 shows the flow rates for various channel cross-sectional areas. It is noted that the smaller the channel cross-sectional area, the longer the effective pumping period, but at the cost of a reduction in flow rate. Figure 4.5 shows the flow rates for various channel lengths. It can be observed that a longer channel length gives rise to a longer effective

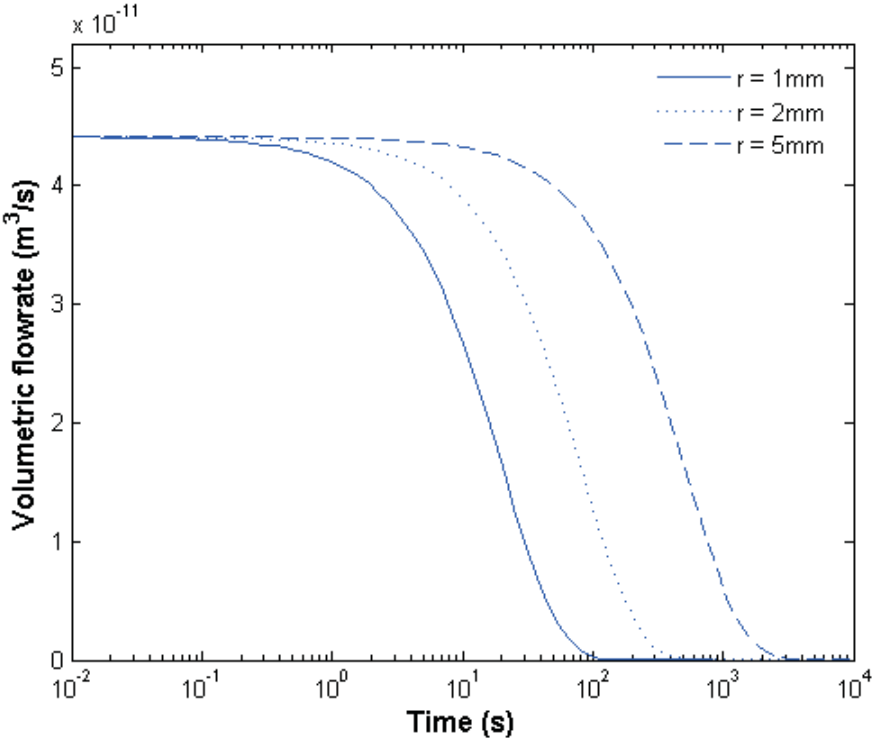

Figure 4.3 Volumetric flow rate versus time for different reservoir radii.

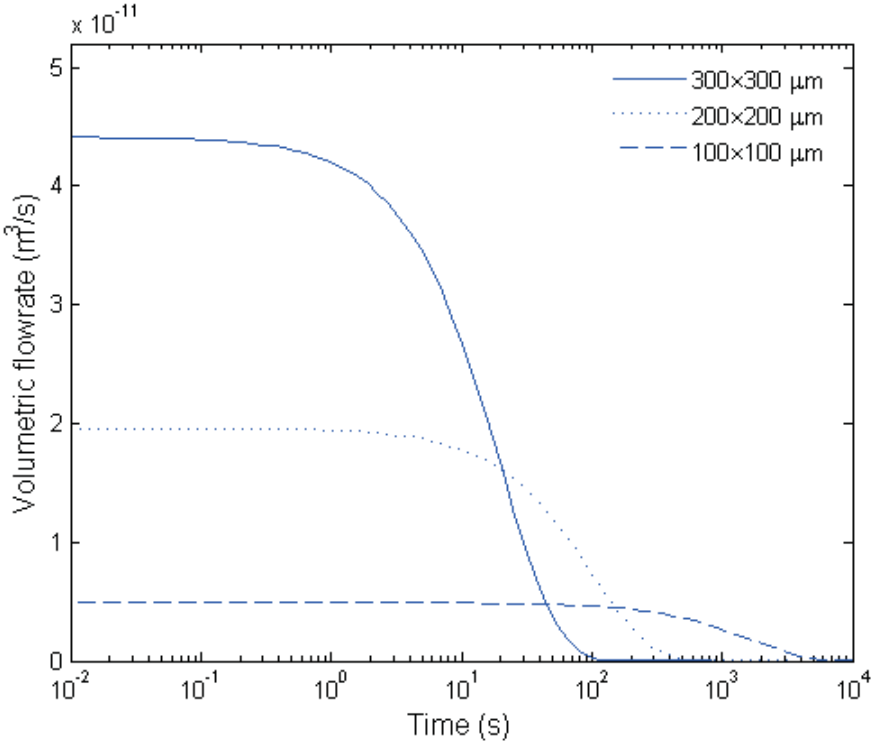

Figure 4.4 Volumetric flow rate versus time for different channel cross sections ($2w \times 2h$).

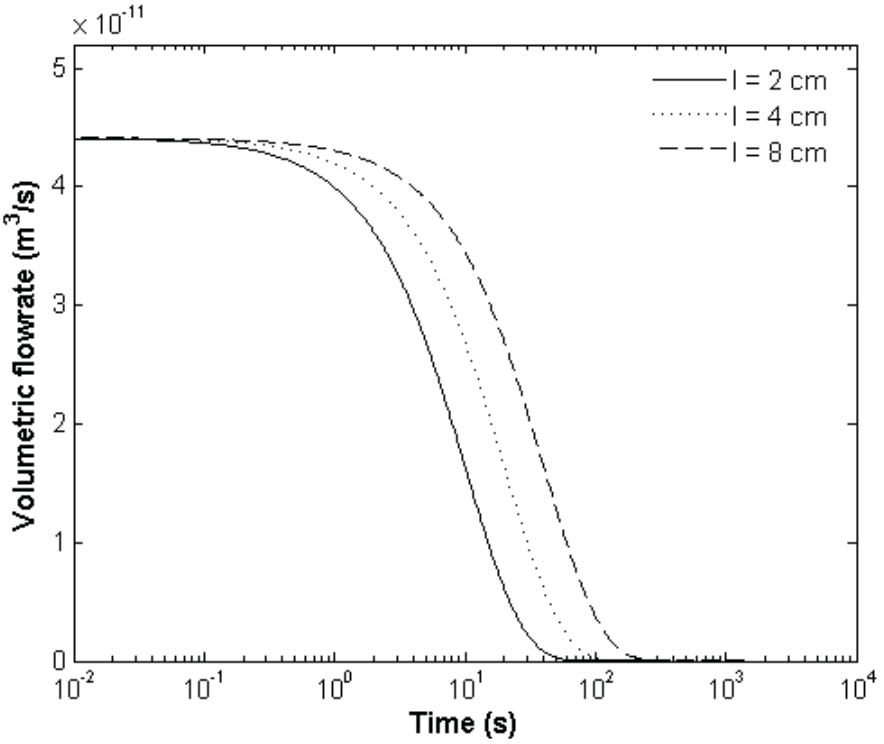

Figure 4.5 Volumetric flow rate versus time for different channel lengths.

pumping period, with the maximum flow rate unchanged which is determined by the EOF velocity and the cross-sectional area of the channel as shown in Eqs. (4.8) and (4.9). Nevertheless, the scenarios shown in Figure 4.3 to Figure 4.5 can be explained using Eqs. (4.11) and (4.13) which clearly show the induced backpressure and the backpressure-driven flow rate are inversely proportional to the cross-sectional area of reservoir, A or/and the channel length, l. Though no simple analytical expression is available to describe the relationship between the channel cross-sectional area, $4wh$ and the induced backpressure gradient or driven flow rate, it can be deduced that the general trend is the larger the channel cross-sectional area, the stronger the effect of the induced backpressure-driven flow.

4.2.4.2 Velocity field

The evolution of the velocity distribution with time is simulated, and the simulation results are displayed in Figure 4.6. It is noted in Figure 4.6(a) that the velocity field keeps the "plug-flow" during the period of EOF effective pumping. Afterwards the

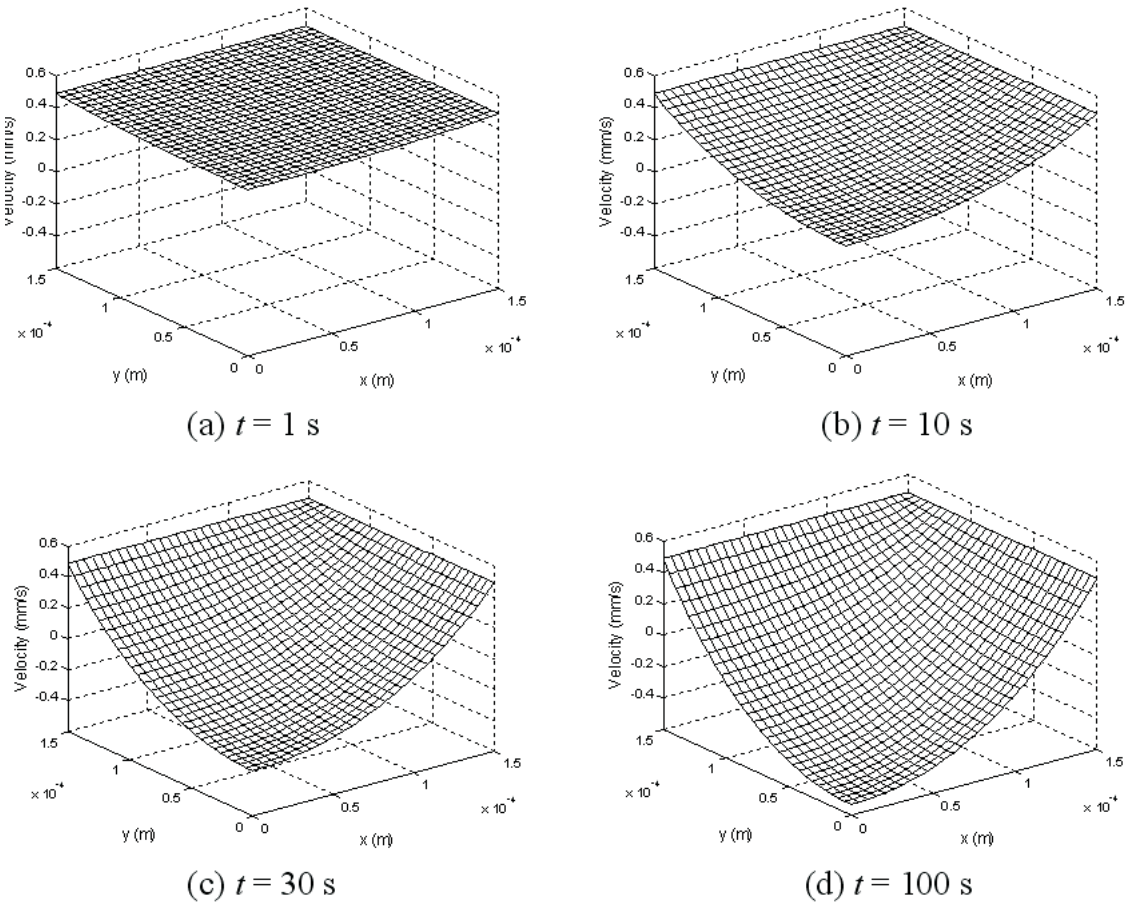

Figure 4.6 Time evolution of EOF velocity distributions due to finite reservoir size effects. The electric field is imposed upwards and has a strength of 100 V/cm, and the working fluid is DI water.

fluid velocity starts changing its shape due to the induced backpressure resulted from the difference of fluid level in the two reservoirs (see Figure 4.6(b)). As time elapses, the induced backpressure-driven flow is getting stronger by showing a parabolic velocity distribution in Figure 4.6(c). In Figure 4.6(d), it is observed that the flow velocity field finally reaches a stage that the total volumetric flow rate is zero due to a counterbalance between the EOF velocity upward in the near wall region and the induced backpressure-driven flow downward in the central region of the channel.

4.3 Experimental Study

4.3.1 Experimental setup and procedure

To verify the proposed model, a micro-PIV system was used to measure the velocity field (Santiago *et al.*, 1998). A schematic of the measurement setup is the same as shown in Figure 3.2. The rectangular microchannel (VitroCom, ST8330) is made of borosilicate glass with a 300 μm × 300 μm inner dimension and a 4 cm length. The microchannel was embedded in a polymer holder with two cylindrical reservoirs machined in it. Radius of both reservoirs is 1 mm. The working fluid is deionized water. For DI water, the characteristic EDL thickness specified by the Debye length is around 1 μm (Probstein, 1994). Compared to the channel size of 300 μm, the EDL thickness is so small that the velocity profile in the EDL region can be negligible by using slip-velocity approximation approach.

Prior to loading the measurement cell with the particle suspension, the cell was cleaned in an ultrasonic cleaner with deionized water. Fluorescent polystyrene particles of diameter 930 nm (Duke Scientific Co.) were used. The number concentration of seeding particle in the suspension was approximately 2×10^9 particles/ml. A DC electric field was applied using platinum electrodes inserted into both reservoirs at the ends of the microchannel cell. A high-voltage power supply (PS350, Stanford Research) was used to apply 400 volts to the electrodes, resulting in an electric field of 100 V/cm. Under such low electric field strength, the Joule heating effect is negligible with DI water as working fluid (Tang *et al.*, 2003). This justifies the assumption of the neglect of Joule heating effects in the model development. Focusing the objective lens on the mid-plane of the rectangular channel, we measured the velocity distributions at four different times: 1 s, 10 s, 30 s, and 100 s. The images obtained in measurements were evaluated with PIVview software (PivTec GmbH).

4.3.2 Experimental results and comparison with theory

Micro-PIV technique utilizes tracer particles that are usually charged in liquids. As a result, the measured particle velocity is a combination of the electrophoretic velocity of the tracer particles and the fluid flow field. To obtain the true fluid flow field, the electrophoretic component has to be subtracted from the measured particle velocity. From Chapter 2, the zeta potentials are known for both the channel wall (-62 mV) and the tracer particles (-37 mV) in DI water. With the images processed, the flow velocity field can be obtained by removing the electrophoretic component of the tracer particles' velocity measured by micro-PIV directly.

The flow velocity distributions at the four different times are shown in Figure 4.7. For comparison, quantitative results are presented in Figure 4.8(a) in which the measured data of the fluid velocity are found in good agreement with the results of model predictions, showing the validity of the proposed model. Figure 4.8(b) presents the variation of the fluid velocity at the channel centerline with time. It clearly shows the reverse flow starting time, that is determined by Eq. (4.22) is a divided point, before which the electroosmotic flow is dominated and after which the induced backpressure driven flow overcomes the electroosmotic flow.

4.4 Summary

A theoretical model was presented to describe the finite reservoir size effect. The proposed model was verified by experiment using the micro-PIV technique. Two important time parameters were introduced, including the effective pumping period and the reverse flow starting time to characterize the electroosmotic pumping, and both the effective pumping period and the reverse flow starting time can be determined using the analytical model presented in this study. Several parameters were studied to analyze the reservoir size effects on the EOF effective pumping, including the dimension of the reservoir's cross section, the length of the microchannel, and the cross-sectional area of the microchannel. It was found that the reservoir effect is stronger for smaller

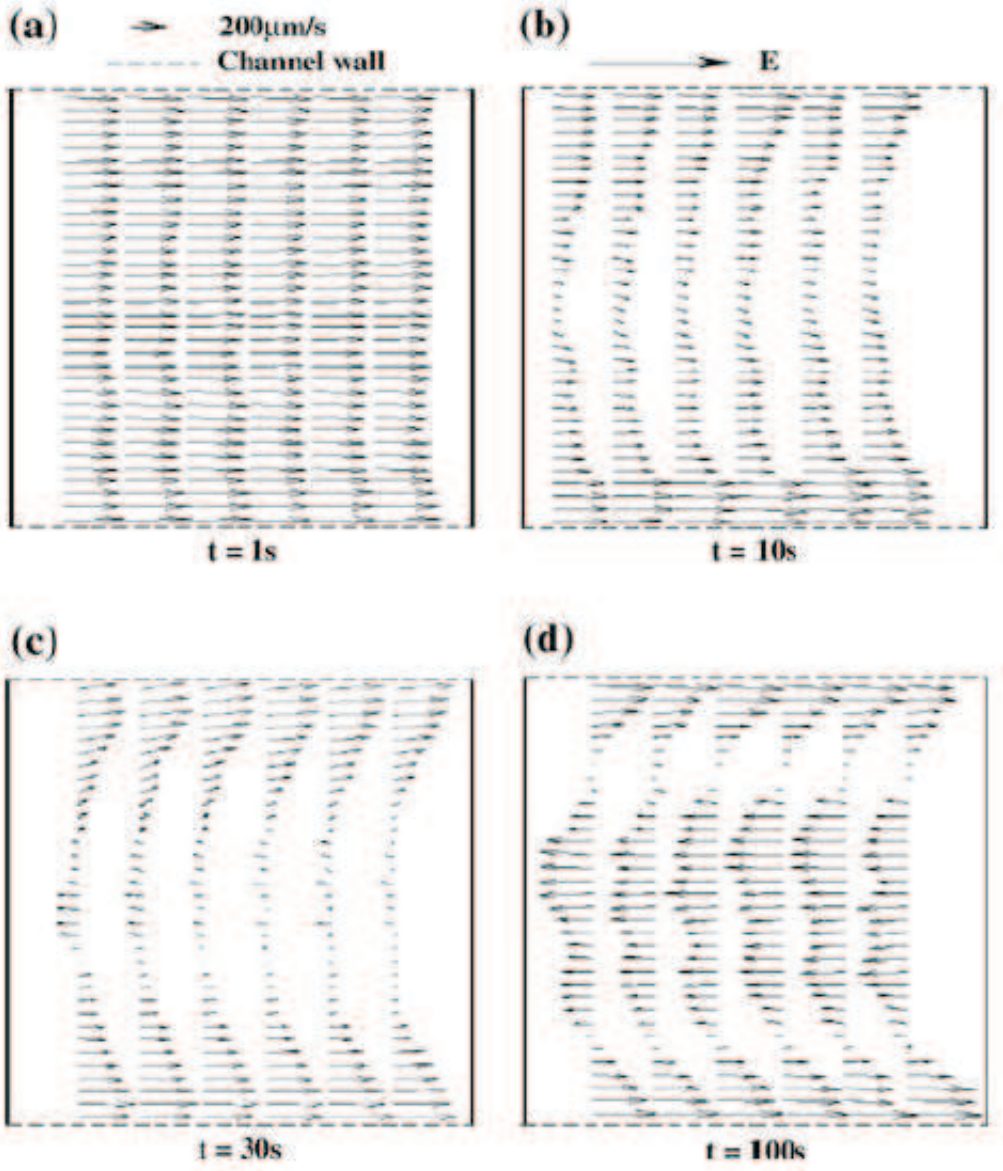

Figure 4.7 Micro-PIV measurement results with finite reservoir size effects at various times: (a) $t = 1$ s, (b) $t = 10$ s, (c) $t = 30$ s, and (d) $t = 100$ s. The electric field is imposed from left to right and has a strength of 100 V/cm, and the working fluid is DI water.

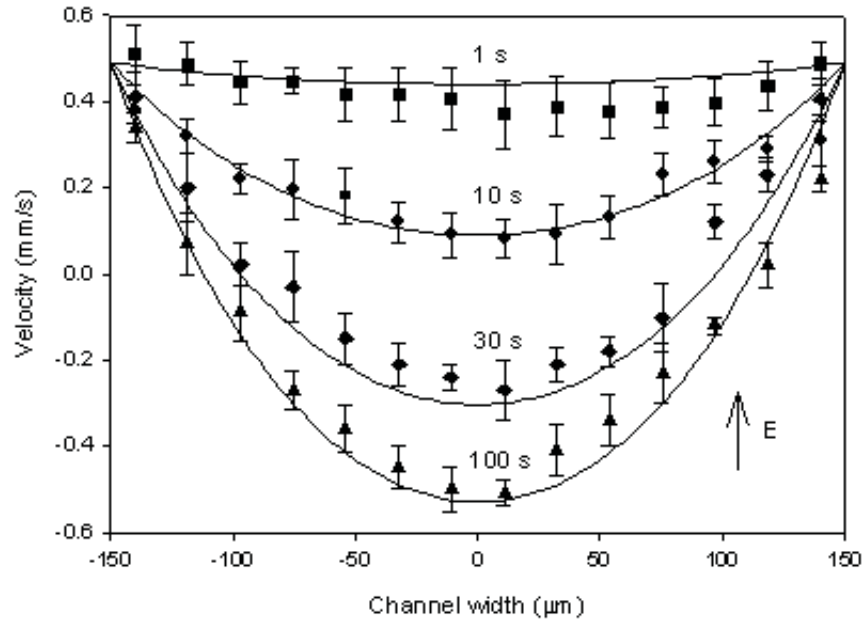

(a)

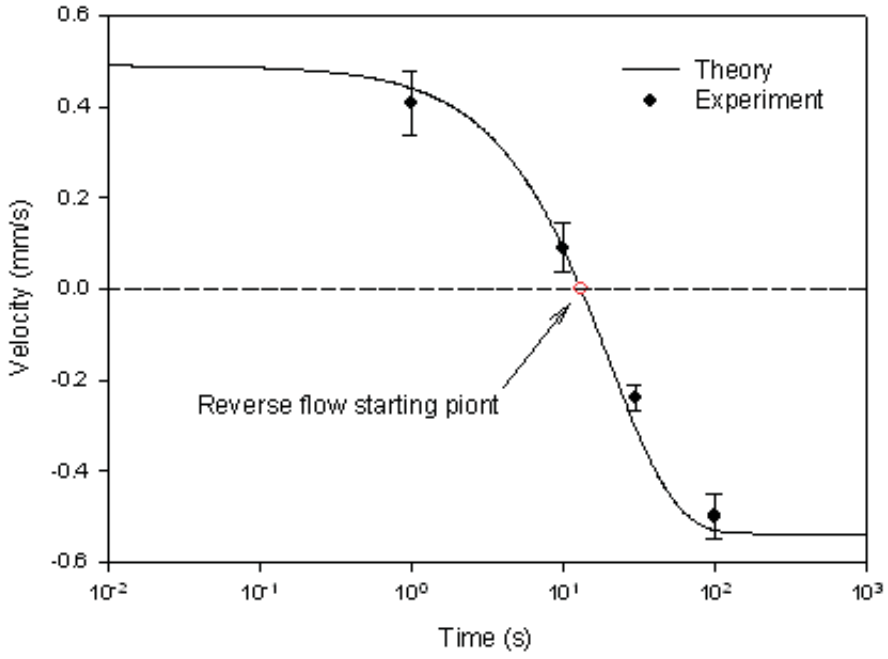

(b)

Figure 4.8 Comparisons of experimental results and theory: (a) Experimental data of the fluid flow (shown by solid symbols) and the theoretically predicted velocity profiles (shown by solid lines) on the middle-plane of the channel at various times; (b) time-dependent response of electroosmotic velocity at the channel center ($x = y = 0$). Reservoir radius: $R = 1$ mm; Electric field strength: $E = 100$ V/cm; Working fluid: DI water.

reservoir size, shorter channel length, and larger channel cross-sectional area. From the simulations, we can conclude that when the dimensions of a channel are fixed, the only factor that will affect the EOF is the area of the reservoir's cross section. Moreover, it is also noted that the size of the channel's cross section significantly affects the effective pumping period. In addition, because the flow rate is proportional to the electric field strength, the flow rate can be improved by increasing the electric field strength applied.

Since cylindrical channels have been widely used in various applications, such as capillary electrophoresis, in Appendix A we present the theoretical derivation for the EOF in a cylindrical tube with finite reservoir size effect using the method developed in this chapter.

Chapter 5

Frequency-dependent Electroosmotic Flow in Microchannels

5.1 Introduction

The study of frequency-dependent electroosmotic flow has attracted lots of attentions due to its perspective of wide applications, such as micromixing (Glasgow *et al.*, 2004), micro actuation (Marcos *et al.*, 2004b), *etc.* In the theoretical studies reported in the literature (referring to Chapter 1), various methods have been used to investigate this problem. However, these approaches employed numerical techniques or complex analysis, which make the analysis complicated. In the present study, based on the slip velocity approximation, a method that combines the Laplace transform and the Frequency Domain Analysis is proposed to solve the governing equations for the frequency-dependent electroosmotic flows in a rectangular microchannel. The DC/AC combined electroosmotic flow in open-end rectangular microchannels is investigated in this study. The analytical solutions for the velocity profiles of the DC/AC combined EOF are obtained.

In nature, the frequency-dependent EOF is also time dependent. Using the micro-

PIV technique, with a synchronization scheme similar to what described in Chapter 3, for the first time we have measured the frequency-dependent EOF velocity distributions. The experimental results are in reasonable agreement with the model predictions.

5.2 Mathematical Modeling of Frequency-dependent EOF in Rectangular Microchannels – Slip Velocity Approach

In this section, we use the slip-velocity approximation method to analyze the frequency-dependent EOF in straight rectangular microchannels. First, the EOF under sole AC (sinusoidal) electric field is studied; then the electroosmotic flow driven by a combined AC and DC electric field is investigated.

5.2.1 The frequency-dependent EOF velocity distributions in both open- and closed-end rectangular microchannels

5.2.1.1 The EOF velocity distributions in both open- and closed-end channels

A frequency-dependent electroosmotic flow in a rectangular microchannel as described in Figure 2.1 is considered. With externally applied electric field $E = E_0 \sin \omega t$, this flow problem essentially belongs to the Stokes second problem with the oscillating slip velocity boundaries. The following dimensionless parameters are introduced:

$$\overline{u} = \frac{u}{U} \quad \bar{t} = \frac{\mu}{\rho D_{\mathrm{h}}^2} t \quad X = \frac{x}{D_{\mathrm{h}}} \quad Y = \frac{y}{D_{\mathrm{h}}} \quad Z = \frac{z}{D_{\mathrm{h}} \mathrm{Re}} \quad \bar{P} = \frac{p}{\rho U^2}$$

where U is the reference velocity, $D_{\mathrm{h}} = 4wh/(w+h)$ is the hydraulic diameter of the rectangular channel, and $\mathrm{Re} = \rho D_{\mathrm{h}} U/\mu$ is the reference Reynolds number. Using the slip-velocity approximation, the slip boundary velocity is determined by the Smolu-

chowski equation, $u_{\mathrm{s}} = -\frac{\varepsilon_0 \varepsilon_{\mathrm{r}} \zeta E_0}{\mu} \sin \omega t$. With $E = E_0 \sin \omega t = E_0 \sin \bar{\omega} \bar{t}$, $\bar{\omega} = \frac{\rho D_{\mathrm{h}}^2}{\mu} \omega$ is introduced as the dimensionless angular frequency, where $\omega = 2\pi f$, and f is the frequency of the AC electric field.

Hence, the velocity field can be obtained by solving the following transient Stokes equation, in a dimensionless form (Yang, 2002)

$$\frac{\partial \bar{u}}{\partial \bar{t}} = \frac{\partial^2 \bar{u}}{\partial X^2} + \frac{\partial^2 \bar{u}}{\partial Y^2} - \frac{\mathrm{d}\bar{P}}{\mathrm{d}Z} \tag{5.1}$$

The initial and boundary conditions applicable to Eq. (5.1) are

$$\bar{u}(X, Y, \bar{t})|_{\bar{t}=0} = 0 \tag{5.2}$$

$$\bar{u}\,\big|_{X=w/D_{\mathrm{h}}} = \bar{u}_{\mathrm{s}0} \sin(\bar{\omega}\bar{t}) \qquad \bar{u}\,\big|_{Y=h/D_{\mathrm{h}}} = \bar{u}_{\mathrm{s}0} \sin(\bar{\omega}\bar{t}) \tag{5.3}$$

$$\left.\frac{\partial \bar{u}}{\partial X}\right|_{X=0} = 0 \qquad \left.\frac{\partial \bar{u}}{\partial Y}\right|_{Y=0} = 0 \tag{5.4}$$

where $\bar{u}_{\mathrm{s}0} = -\frac{\varepsilon_0 \varepsilon_{\mathrm{r}} \zeta E_0}{\mu U}$.

Eq. (5.1) together with above boundary and initial conditions can be solved using the Green's function method. According to Ozisik (1993), the corresponding Green's function G can be obtained by using the separation of variables method, and its expression is given by

$$\begin{aligned} &G(X, Y, \bar{t}\,|X', Y', \tau) \\ &= \frac{4D_{\mathrm{h}}^2}{wh} \sum_{m=1}^{\infty} \sum_{n=1}^{\infty} \mathrm{e}^{-T_{mn}(\bar{t}-\tau)} \cos(\alpha_m X) \cos(\alpha_m X') \cos(\beta_n Y) \cos(\beta_n Y') \end{aligned} \tag{5.5}$$

where $\alpha_m = \left(\frac{2m-1}{2}\right) \frac{D_{\mathrm{h}}}{w}\pi$, $\beta_n = \left(\frac{2n-1}{2}\right) \frac{D_{\mathrm{h}}}{h}\pi$, and $T_{mn} = \alpha_m^2 + \beta_n^2$.
Using the Green's function formulation, one can obtain the velocity distribution as

$$\bar{u}(X, Y, \bar{t}) = -\frac{4D_{\mathrm{h}}^2}{wh} \sum_{m=1}^{\infty} \sum_{n=1}^{\infty} \frac{(-1)^{m+n} \cos(\alpha_m X) \cos(\beta_n Y)}{\alpha_m \beta_n} \int_{\tau=0}^{\bar{t}} \mathrm{e}^{-T_{mn}(\bar{t}-\tau)} \frac{\mathrm{d}\bar{P}}{\mathrm{d}Z}(\tau)\, \mathrm{d}\tau$$

$$+\frac{4D_{\mathrm{h}}^2\bar{u}_{\mathrm{s}0}}{wh}\sum_{m=1}^{\infty}\sum_{n=1}^{\infty}\frac{(-1)^{m+n}\,T_{mn}\cos(\alpha_m X)\cos(\beta_n Y)}{\alpha_m\beta_n}\int_{\tau=0}^{\bar{t}}\mathrm{e}^{-T_{mn}(\bar{t}-\tau)}\sin(\bar{\omega}\tau)\,\mathrm{d}\tau \quad (5.6)$$

Eq. (5.6) is the general solution of the AC-driven electroosmotic flow in a rectangular microchannel. Hence, two specific cases are considered as below.

Case 1: The velocity distribution in an open-end rectangular microchannel

For an open-end channel, if we assume that the channel is infinitely extended and the reservoirs are infinite, there is no pressure gradient along the channel, *i.e.*, $\mathrm{d}\bar{P}/\mathrm{d}Z = 0$. Hence, the expression given by Eq. (5.6) of the velocity distribution can be analytically evaluated as

$$\begin{aligned}\bar{u}(X,Y,\bar{t}) &= \frac{4D_{\mathrm{h}}^2\bar{u}_{\mathrm{s}0}}{wh}\sum_{m=1}^{\infty}\sum_{n=1}^{\infty}(-1)^{m+n}\frac{T_{mn}}{\alpha_m\beta_n}\cos(\alpha_m X)\cos(\beta_n Y)\\ &\qquad\times\int_{\tau=0}^{\bar{t}}\mathrm{e}^{-T_{mn}(\bar{t}-\tau)}\sin(\bar{\omega}\tau)\,\mathrm{d}\tau\\ &= \bar{u}_{\mathrm{s}0}\sin(\bar{\omega}\bar{t}) + \frac{4D_{\mathrm{h}}^2\bar{u}_{\mathrm{s}0}}{ab}\sum_{m=1}^{\infty}\sum_{n=1}^{\infty}\frac{(-1)^{m+n}\cos(\alpha_m X)\cos(\beta_n Y)}{\alpha_m\beta_n}\\ &\qquad\times\frac{-\bar{\omega}^2\sin(\bar{\omega}\bar{t}) - T_{mn}\bar{\omega}\cos(\bar{\omega}\bar{t}) + T_{mn}\bar{\omega}\exp(-T_{mn}\bar{t})}{T_{mn}^2+\bar{\omega}^2} \quad (5.7)\end{aligned}$$

The Laplace transform of Eq. (5.7) is expressed by

$$\hat{u}(X,Y,s) = \frac{4D_{\mathrm{h}}^2\bar{u}_{\mathrm{s}0}}{wh}\frac{\bar{\omega}}{s^2+\bar{\omega}^2}\sum_{m=1}^{\infty}\sum_{n=1}^{\infty}(-1)^{m+n}\frac{\cos(\alpha_m X)\cos(\beta_n Y)}{\alpha_m\beta_n}\frac{T_{mn}}{s+T_{mn}} \quad (5.8)$$

Case 2: The velocity distribution in a closed-end rectangular microchannel

For a closed-end channel, due to the closed-end structure, a back pressure gradient $\mathrm{d}\bar{P}/\mathrm{d}Z$ will be induced to fulfill the zero flow rate condition, which due to geometric symmetry can be expressed as

$$\int_{X=0}^{w/D_{\mathrm{h}}}\int_{Y=0}^{h/D_{\mathrm{h}}}\bar{u}(X,Y,\bar{t})\mathrm{d}X\mathrm{d}Y = 0 \quad (5.9)$$

Substituting Eq. (5.6) into Eq. (5.9) gives

$$-\frac{4D_{\mathrm{h}}^2}{wh}\sum_{m=1}^{\infty}\sum_{n=1}^{\infty}\frac{1}{\alpha_m^2\beta_n^2}\int_{\tau=0}^{\bar{t}}\mathrm{e}^{-T_{mn}(\bar{t}-\tau)}\frac{\mathrm{d}\bar{P}}{\mathrm{d}Z}(\tau)\,\mathrm{d}\tau$$
$$+\frac{4D_{\mathrm{h}}^2}{wh}\sum_{m=1}^{\infty}\sum_{n=1}^{\infty}\frac{T_{mn}}{\alpha_m^2\beta_n^2}\int_{\tau=0}^{\bar{t}}\mathrm{e}^{-T_{mn}(\bar{t}-\tau)}\sin(\bar{\omega}\tau)\,\mathrm{d}\tau=0 \tag{5.10}$$

Eq. (5.10) is an integration equation whose analytical solution is difficult to obtain. Applying the Laplace transform to Eq. (5.10) and making rearrangement, we obtain the Laplace transform of the dimensionless pressure gradient as

$$\mathcal{L}\left[\frac{\mathrm{d}\bar{P}}{\mathrm{d}Z}(\bar{t})\right]=\bar{u}_{\mathrm{s}0}\frac{\bar{\omega}}{s^2+\bar{\omega}^2}\frac{\sum_{m=1}^{\infty}\sum_{n=1}^{\infty}\frac{T_{mn}}{\alpha_m^2\beta_n^2}\frac{1}{s+T_{mn}}}{\sum_{m=1}^{\infty}\sum_{n=1}^{\infty}\frac{1}{\alpha_m^2\beta_n^2}\frac{1}{s+T_{mn}}} \tag{5.11}$$

Further applying the Laplace transform to Eq. (5.6) and using Eq. (5.11), one can obtain the Laplace transform of the velocity field as

$$\hat{u}(X,Y,s)=-\frac{4D_{\mathrm{h}}^2}{wh}\sum_{m=1}^{\infty}\sum_{n=1}^{\infty}\frac{(-1)^{m+n}\cos(\alpha_m X)\cos(\beta_n Y)}{\alpha_m\beta_n}\frac{1}{s+T_{mn}}\mathcal{L}\left[\frac{\mathrm{d}\bar{P}}{\mathrm{d}Z}(\bar{t})\right]$$
$$+\frac{4D_{\mathrm{h}}^2}{wh}\bar{u}_{\mathrm{s}0}\sum_{m=1}^{\infty}\sum_{n=1}^{\infty}(-1)^{m+n}\frac{\cos(\alpha_m X)\cos(\beta_n Y)}{\alpha_m\beta_n}\frac{T_{mn}}{s+T_{mn}}\frac{\bar{\omega}}{s^2+\bar{\omega}^2}$$

$$=\frac{4D_{\mathrm{h}}^2\bar{u}_{\mathrm{s}0}}{wh}\frac{\bar{\omega}}{s^2+\bar{\omega}^2}\left\{-\sum_{m=1}^{\infty}\sum_{n=1}^{\infty}\frac{(-1)^{m+n}\cos(\alpha_m X)\cos(\beta_n Y)}{\alpha_m\beta_n(s+T_{mn})}\right.$$
$$\left.\times\frac{\sum_{m=1}^{\infty}\sum_{n=1}^{\infty}\frac{T_{mn}}{\alpha_m^2\beta_n^2}\frac{1}{s+T_{mn}}}{\sum_{m=1}^{\infty}\sum_{n=1}^{\infty}\frac{1}{\alpha_m^2\beta_n^2}\frac{1}{s+T_{mn}}}+\sum_{m=1}^{\infty}\sum_{n=1}^{\infty}(-1)^{m+n}\frac{\cos(\alpha_m X)\cos(\beta_n Y)T_{mn}}{\alpha_m\beta_n(s+T_{mn})}\right\} \tag{5.12}$$

Using the fixed Talbot (FT) method (Abate and Valko, 2004), we obtain the EOF velocity distribution at a given time $\bar{t}$

$$\bar{u}(X,Y,\bar{t})=\mathcal{L}^{-1}\left[\hat{u}(X,Y,s)\right] \tag{5.13}$$

Figure 5.1 An overall system with single input and single output.

5.2.1.2 Steady oscillating flow by frequency domain analysis

Based on Eqs. (5.11) and (5.12), one can numerically inverse the Laplace transform to obtain the pressure gradient and velocity distributions. In fact, one needs this numerical inversion to get the velocity distribution or pressure gradient, especially in the transient stage with initial effect. However, for the steady oscillating period after the initial effect decays, use of the numerical Laplace inversion method is tedious and inefficient. Thus, one can propose to use the Frequency Domain Analysis to solve this problem (see Appendix B for details). This method also provides a physical insight into this AC-driven EOF.

It is noted that in the expressions for the Laplace transforms of the pressure gradient and the velocity field, there is a factor $\frac{\bar{\omega}}{s^2+\bar{\omega}^2}$, which denotes the Laplace transform of $\sin \bar{\omega}\bar{t}$. Hence, one can readily treat the expressions of the Laplace transforms of the pressure gradient and the velocity distribution as a product of two factors: one is $\frac{\bar{\omega}}{s^2+\bar{\omega}^2}$, the other is noted as $G(s)$, Which is represented by $G_{\mathrm{p}}(s)$ or $G_{\mathrm{v}}(s)$, for the pressure gradient and the velocity field, respectively.

According to the theory of signals and systems, $\frac{\bar{\omega}}{s^2+\bar{\omega}^2}$ is the input function $U(s)$ of a sinusoidal wave, $G(s)$ is a transfer function, and the expression of either $\mathcal{L}\left[\frac{\mathrm{d}\bar{P}}{\mathrm{d}Z}(\bar{t})\right]$ or $\mathcal{L}[\bar{u}(X,Y,\bar{t})]$ is an output function $Y(s)$. Physically, the system of $G(s)$ is a stable one (Suresh and Homsy, 2004). The overall system can be sketched in Figure 5.1.

$$Y(s) = G(s)\,U(s) \tag{5.14}$$

Due to the sinusoidal input function $\frac{\bar{\omega}}{s^2+\bar{\omega}^2}$ applied to a stable system of $G(s)$, the

output is also a sinusoidal one, whose amplitude is given by

$$|G(\mathrm{j}\bar{\omega})| = \sqrt{\mathrm{Real}\left[G(\mathrm{j}\bar{\omega})\right]^2 + \mathrm{Imag}\left[G(\mathrm{j}\bar{\omega})\right]^2} \tag{5.15}$$

and the sinusoidal output is shifted by a phase angle expressed as

$$\psi = \tan^{-1}\left\{\frac{\mathrm{Imag}\left[G(\mathrm{j}\bar{\omega})\right]}{\mathrm{Real}\left[G(\mathrm{j}\bar{\omega})\right]}\right\} \tag{5.16}$$

where $\mathrm{j} = \sqrt{-1}$. Using this approach, one can compute any value of the pressure gradient or the velocity distribution as

$$y = |G(\mathrm{j}\bar{\omega})| \sin(\bar{\omega}\bar{t} + \psi) \tag{5.17}$$

where y is the output value of either the pressure gradient $\frac{\mathrm{d}\bar{P}}{\mathrm{d}Z}(\bar{t})$ or the velocity distribution $\bar{u}(X, Y, \bar{t})$. In fact, y is the Laplace inverse transform of the output function $Y(s)$. In this way, one can avoid using the numerical inversion of the Laplace transform to compute the pressure gradient $\frac{\mathrm{d}\bar{P}}{\mathrm{d}Z}(\bar{t})$ and velocity distribution $\bar{u}(X, Y, \bar{t})$.

5.2.2 A combined DC/AC driven EOF in an open-end rectangular microchannel

Different from the precedent section in which a sinusoidal electric field is applied along the channel, in this section, a DC/AC combined electric field is applied, *i.e.*, an AC electric field with a DC offset. The externally applied DC/AC combined electric field can be expressed as

$$E = E_1 + E_0 \sin(\omega t) \tag{5.18}$$

then the outer slip boundary velocity is determined by the Smoluchowski equation

$$u_{\mathrm{s}} = -\frac{\varepsilon_0 \varepsilon_{\mathrm{r}} \zeta}{\mu} E$$

$$= -\frac{\varepsilon_0 \varepsilon_r \zeta}{\mu} \left[E_1 + E_0 \sin(\omega t)\right] \tag{5.19}$$

Under the slip velocity approximation, the time- and frequency-dependent EOF is governed by the transient Stokes equation, which is expressed in a dimensionless form as

$$\frac{\partial \bar{u}}{\partial \bar{t}} = \frac{\partial^2 \bar{u}}{\partial X^2} + \frac{\partial^2 \bar{u}}{\partial Y^2} \tag{5.20}$$

The initial and boundary conditions applicable to Eq. (5.20) are

$$\bar{u}(X, Y, \bar{t})|_{\bar{t}=0} = 0 \tag{5.21}$$

$$\bar{u}\,\big|_{X=w/D_h} = \bar{u}_{s1} + \bar{u}_{s0} \sin(\bar{\omega}\bar{t}) \qquad \bar{u}\,\big|_{Y=h/D_h} = \bar{u}_{s1} + \bar{u}_{s0} \sin(\bar{\omega}\bar{t}) \tag{5.22}$$

$$\left.\frac{\partial \bar{u}}{\partial X}\right|_{X=0} = 0 \qquad \left.\frac{\partial \bar{u}}{\partial Y}\right|_{Y=0} = 0 \tag{5.23}$$

where $\bar{u}_{s1} = -\frac{\varepsilon_0 \varepsilon_r \zeta E_1}{\mu U}$ and $\bar{u}_{s0} = -\frac{\varepsilon_0 \varepsilon_r \zeta E_0}{\mu U}$. It is noted that two boundary conditions are non-homogeneous.

Letting $\bar{u}(X, Y, \bar{t}) = \bar{u}_1(X, Y, \bar{t}) + \bar{u}_0(X, Y, \bar{t})$, the solution of Eq. (5.20) can be obtained by solving two separated partial differential equations (I) and (II) for $\bar{u}_1$ and $\bar{u}_0$, respectively, as below

$$\text{(I)} \qquad \frac{\partial \bar{u}_1}{\partial \bar{t}} = \frac{\partial^2 \bar{u}_1}{\partial X^2} + \frac{\partial^2 \bar{u}_1}{\partial Y^2} \tag{5.24}$$

with initial and boundary conditions

$$\bar{u}_1(X, Y, \bar{t})|_{\bar{t}=0} = 0 \tag{5.25}$$

$$\bar{u}_1\,\big|_{X=w/D_h} = \bar{u}_{s1} \qquad \bar{u}_1\,\big|_{Y=h/D_h} = \bar{u}_{s1} \tag{5.26}$$

$$\left.\frac{\partial \bar{u}_1}{\partial X}\right|_{X=0} = 0 \qquad \left.\frac{\partial \bar{u}_1}{\partial Y}\right|_{Y=0} = 0 \tag{5.27}$$

$$\text{(II)} \qquad \frac{\partial \bar{u}_0}{\partial \bar{t}} = \frac{\partial^2 \bar{u}_0}{\partial X^2} + \frac{\partial^2 \bar{u}_0}{\partial Y^2} \tag{5.28}$$

with initial and boundary conditions

$$\bar{u}_0(X,Y,\bar{t})|_{\bar{t}=0} = 0 \tag{5.29}$$

$$\bar{u}_0\left|_{X=w/D_\mathrm{h}}\right. = \bar{u}_{\mathrm{s}0}\sin(\bar{\omega}\bar{t}) \qquad \bar{u}_0\left|_{Y=h/D_\mathrm{h}}\right. = \bar{u}_{\mathrm{s}0}\sin(\bar{\omega}\bar{t}) \tag{5.30}$$

$$\left.\frac{\partial\bar{u}_0}{\partial X}\right|_{X=0} = 0 \qquad \left.\frac{\partial\bar{u}_0}{\partial Y}\right|_{Y=0} = 0 \tag{5.31}$$

Using the separation of variable method, one can show that the solution to Eq. (5.24) is

$$\bar{u}_1(X,Y,\bar{t}) = \bar{u}_{\mathrm{s}1} - \frac{16\bar{u}_{\mathrm{s}1}}{\pi^2}\sum_{m=1}^{\infty}\sum_{n=1}^{\infty}\frac{(-1)^{m+n}\cos(\alpha_m X)\cos(\beta_n Y)\exp(-T_{mn}\bar{t})}{(2m-1)(2n-1)} \tag{5.32}$$

As for Eq. (5.28) with initial and boundary conditions, one can observe that it is identical to Eq. (5.1) of Case 1, and hence the solution is expressed as

$$\begin{aligned}\bar{u}_0(X,Y,\bar{t}) &= \bar{u}_{\mathrm{s}0}\sin(\bar{\omega}\bar{t})\\ &+\frac{4D_\mathrm{h}^2\bar{u}_{\mathrm{s}0}}{wh}\sum_{m=1}^{\infty}\sum_{n=1}^{\infty}\frac{(-1)^{m+n}\cos(\alpha_m X)\cos(\beta_n Y)}{\alpha_m\beta_n}\\ &\times\frac{-\bar{\omega}^2\sin(\bar{\omega}\bar{t}) - T_{mn}\bar{\omega}\cos(\bar{\omega}\bar{t}) + T_{mn}\bar{\omega}\exp(-T_{mn}\bar{t})}{T_{mn}^2+\bar{\omega}^2}\end{aligned} \tag{5.33}$$

Therefor, the complete solution of Eq. (5.20) is given by

$$\bar{u}(X,Y,\bar{t}) = \bar{u}_1(X,Y,\bar{t}) + \bar{u}_0(X,Y,\bar{t})$$

$$\begin{aligned}&= \bar{u}_{\mathrm{s}1} - \frac{16\bar{u}_{\mathrm{s}1}}{\pi^2}\sum_{m=1}^{\infty}\sum_{n=1}^{\infty}\frac{(-1)^{m+n}\cos(\alpha_m X)\cos(\beta_n Y)\exp(-T_{mn}\bar{t})}{(2m-1)(2n-1)}\\ &+\bar{u}_{\mathrm{s}0}\sin(\bar{\omega}\bar{t}) + \frac{4D_\mathrm{h}^2\bar{u}_{\mathrm{s}0}}{wh}\sum_{m=1}^{\infty}\sum_{n=1}^{\infty}\frac{(-1)^{m+n}\cos(\alpha_m X)\cos(\beta_n Y)}{\alpha_m\beta_n}\\ &\times\frac{-\bar{\omega}^2\sin(\bar{\omega}\bar{t}) - T_{mn}\bar{\omega}\cos(\bar{\omega}\bar{t}) + T_{mn}\bar{\omega}\exp(-T_{mn}\bar{t})}{T_{mn}^2+\bar{\omega}^2}\end{aligned} \tag{5.34}$$

It can be observed that the initial effect due to the terms with the factor $\exp(-T_{mn}\bar{t})$

decays with time. In fact, by keeping the slowest decaying terms with $m = n = 1$, the characteristic time of the electroosmotic flow can be estimated as (Marcos *et al.*, 2004a)

$$t_{\mathrm{c}} = \frac{4\rho}{\pi^2 \mu} \frac{w^2 h^2}{w^2 + h^2} \tag{5.35}$$

Beyond the characteristic time t_{c}, the initial effect decays fast, so the velocity field of the steadily oscillating EOF can be expressed as

$$\bar{u}\left(X, Y, \bar{t}\right) = \bar{u}_{\mathrm{s1}} + \bar{u}_{\mathrm{s0}} \sin\left(\bar{\omega}\bar{t}\right)$$

$$-\frac{4D_{\mathrm{h}}^2 \bar{u}_{\mathrm{s0}}}{wh} \sum_{m=1}^{\infty} \sum_{n=1}^{\infty} (-1)^{m+n} \frac{\cos\left(\alpha_m X\right) \cos\left(\beta_n Y\right)}{\alpha_m \beta_n} \frac{\bar{\omega}^2 \sin\left(\bar{\omega}\bar{t}\right) + T_{mn}\bar{\omega} \cos\left(\bar{\omega}\bar{t}\right)}{T_{mn}^2 + \bar{\omega}^2} \tag{5.36}$$

Eq. (5.36) shows that the solution consists of the constant velocity part (the first term) due to the DC electric field effect and the oscillating part (the second and third terms) due to the AC electric field effect.

5.3 Experimental Setup and Procedure

In the present work, the same micro-PIV system used in Chapter 3 was employed for imaging the velocity field. In order to synchronize the time control signals precisely, a microcontroller based sine wave generator (Optrobio Tech$^{\mathrm{TM}}$) was used in experiment. The wave generator has a function to adjust the frequency and amplitude, and can be triggered for synchronization at certain phases in a given AC cycle. The micro-PIV system is set in the internal triggering mode, under which an output signal (A8) from PCI card was used to synchronize the wave generator to the recording sequence. The time for triggering the wave generator prior to measurement is adjustable, and it is realized by changing the initial delay time in the control software (Davis 6.2, LaVision Inc.).

An AC amplifier (Optrobio Tech$^{\mathrm{TM}}$) was used for magnifying the signals from the sine wave generator. The AC amplifier has a function of providing a DC offset. Using the microcontroller based sine wave generator together with the AC amplifier and

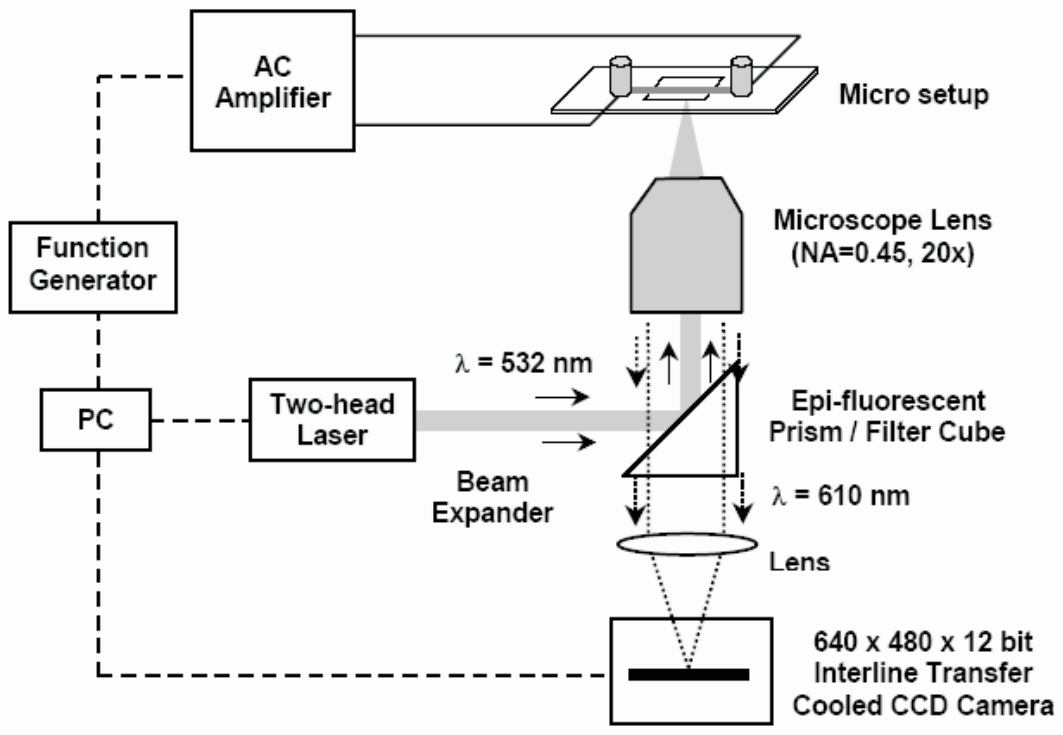

Figure 5.2 Schematic of the experimental setup.

adjusting the DC offset (E_1), one can apply a combined sinusoidal AC voltage with a DC offset to the platinum electrodes inserted into two reservoirs connecting the microchannel. The generated wave form is shown in Figure 5.3. First, by setting the offset value $E_1 = 0$, we measured the pure AC driven EOF in both open- and closed-end microchannels. Then with a DC offset, we measured the EOF under a DC/AC combined electric field.

The initial effect in the oscillating electroosmotic flow is present. However, due to its short duration, it has very limited influence on a microfluidic system. Thus we only measured the periodically steady-state electroosmotic flows. As the rectangular channel used in experiment has a cross section of $2w \times 2h = 300\,\mu\text{m} \times 300\,\mu\text{m}$, using Eq. (5.35) one can estimate the initial transient time $t_c = 5$ ms. In the measurements, the frequency of $20 \sim 50$ Hz is used, under which the initial effect was present during the first cycle. By adjusting the synchronization timing and focusing the objective lens on the mid-plane (*i.e.*, $y = 0$), we measured the four phases (namely, $\psi = \pi/2$, π, $3\pi/2$, and 2π) within the second or third cycle in order to avoid the initial transient

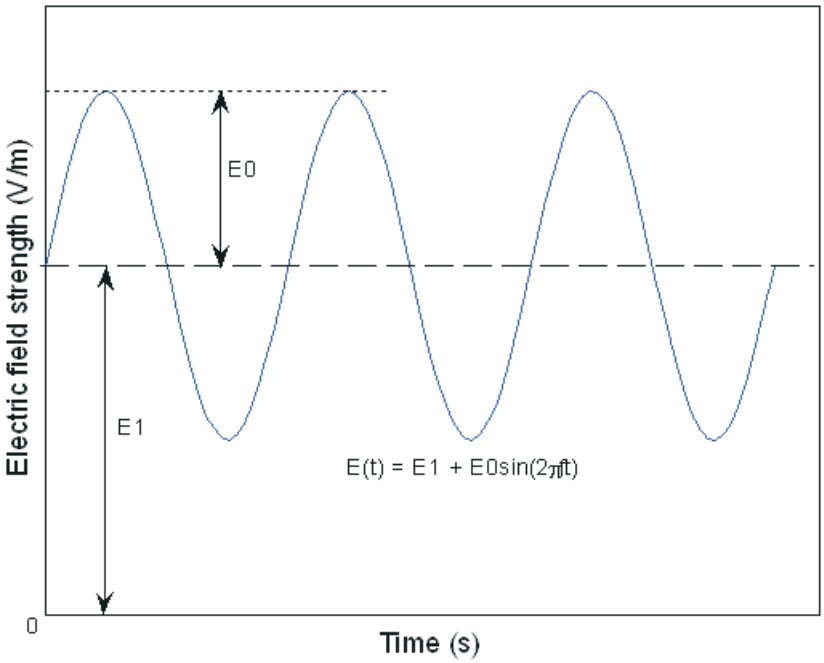

Figure 5.3 Electric field applied on the microchannel.

effect. The raw images aquired by the micro-PIV system were then processed by using PIVview software (PivTec GmbH). Because the tracer particles are charged in deionized water, we employed the method described in Chapter 4 to subtract the electrophoretic effect.

5.4 Results and Discussion

5.4.1 Frequency-dependent EOF velocity distribution in open- and closed-end channels

5.4.1.1 Open-end channel

For computing the steady-state velocity distribution in an open-end rectangular microchannel, we can use either Eq. (5.7) with neglecting decaying terms or Eq. (5.8) with the Frequency Domain Analysis. The latter provides an approach to calculate the amplitude of the velocity. Using Eq. (5.15), under the experimental conditions of $f = 50$ Hz, $E_1 = 0$ and $E_0 = 100$ V/cm, one can compute the velocity amplitude

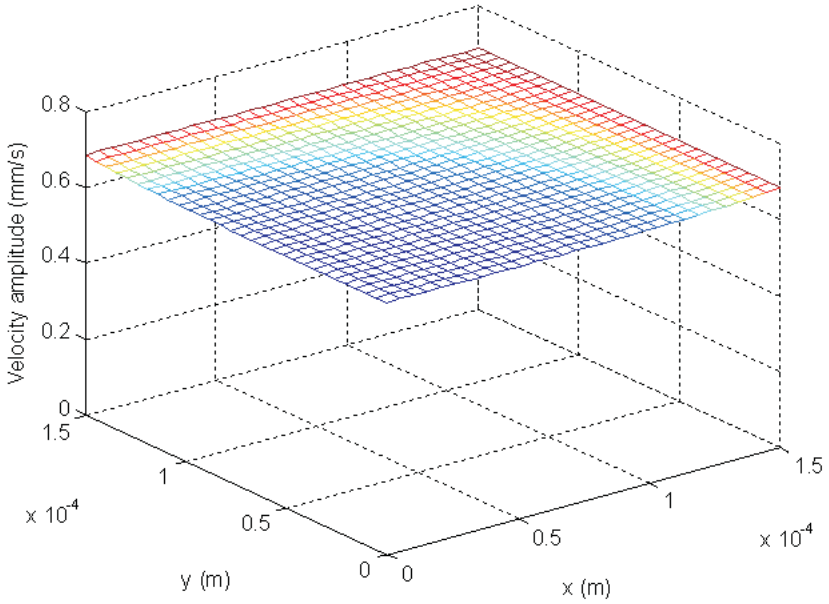

Figure 5.4 Velocity amplitude in an open-end rectangular channel ($f = 50$ Hz).

across one quarter of the channel, and the results are presented in Figure 5.4. It can be observed that under such a frequency, the amplitude distribution is also "plug-like". This fact can be explained that the period of an cycle is much larger than the characteristic time, *i.e.*, $1/f \gg t_c$, so the motion of the fluid near the channel wall has enough time to be extended to the center region of the channel. As a result, the flow velocity field exhibits a fully-developed state.

Using the micro-PIV technique, the velocity distributions on the middle plane of the channel were measured at four phases ($\psi = \pi/2$, π, $3\pi/2$, and 2π) in AC cycle. With the electrophoretic effect removed, the processed vector plots at different phases are shown in Figure 5.5. Extracting the velocity data and averaging the values along the flowing direction, we plot the averaged velocity values in Figure 5.6, from which a reasonable agreements between theory and experiment is found, suggesting the valid model presented in this study.

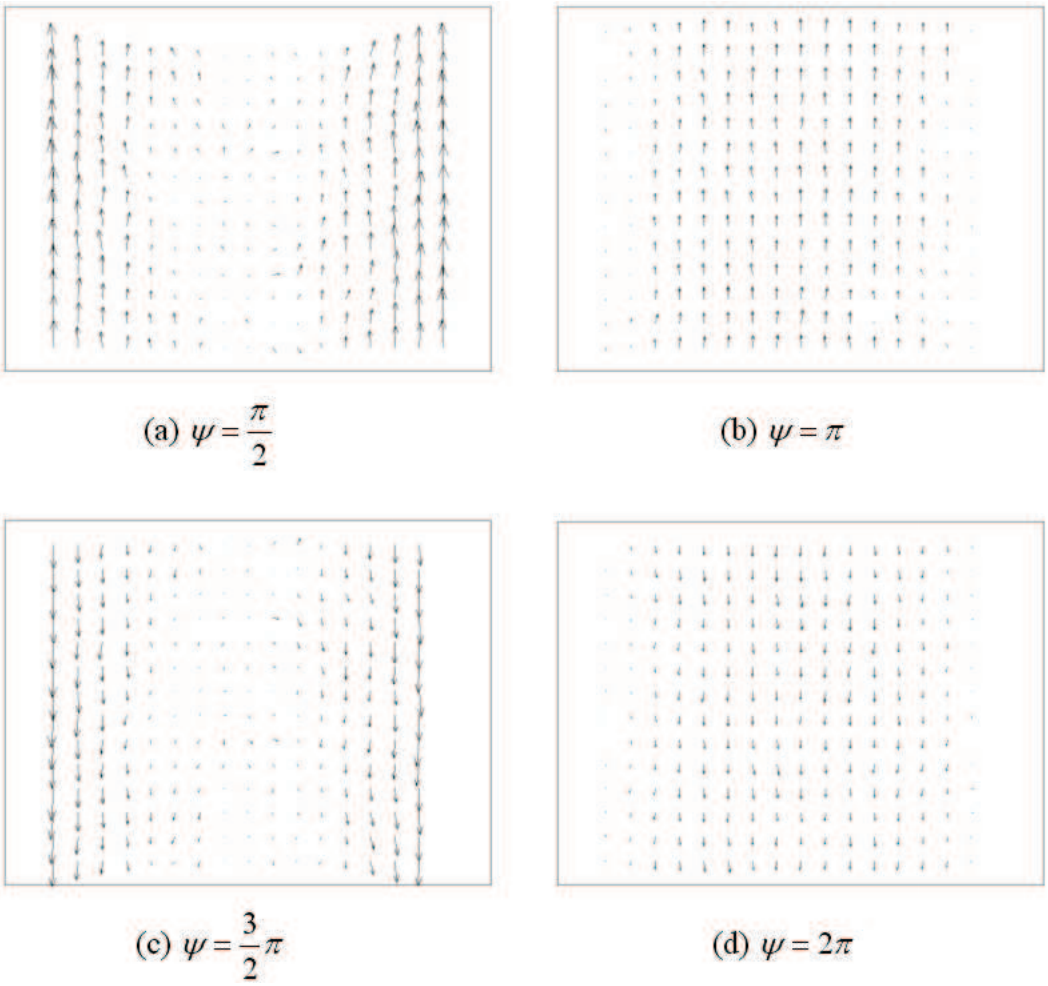

Figure 5.5 Micro-PIV measuremed velocity distributions of frequency-dependent EOF in an open-end channel at four phases during an AC cycle ($f = 50$ Hz).

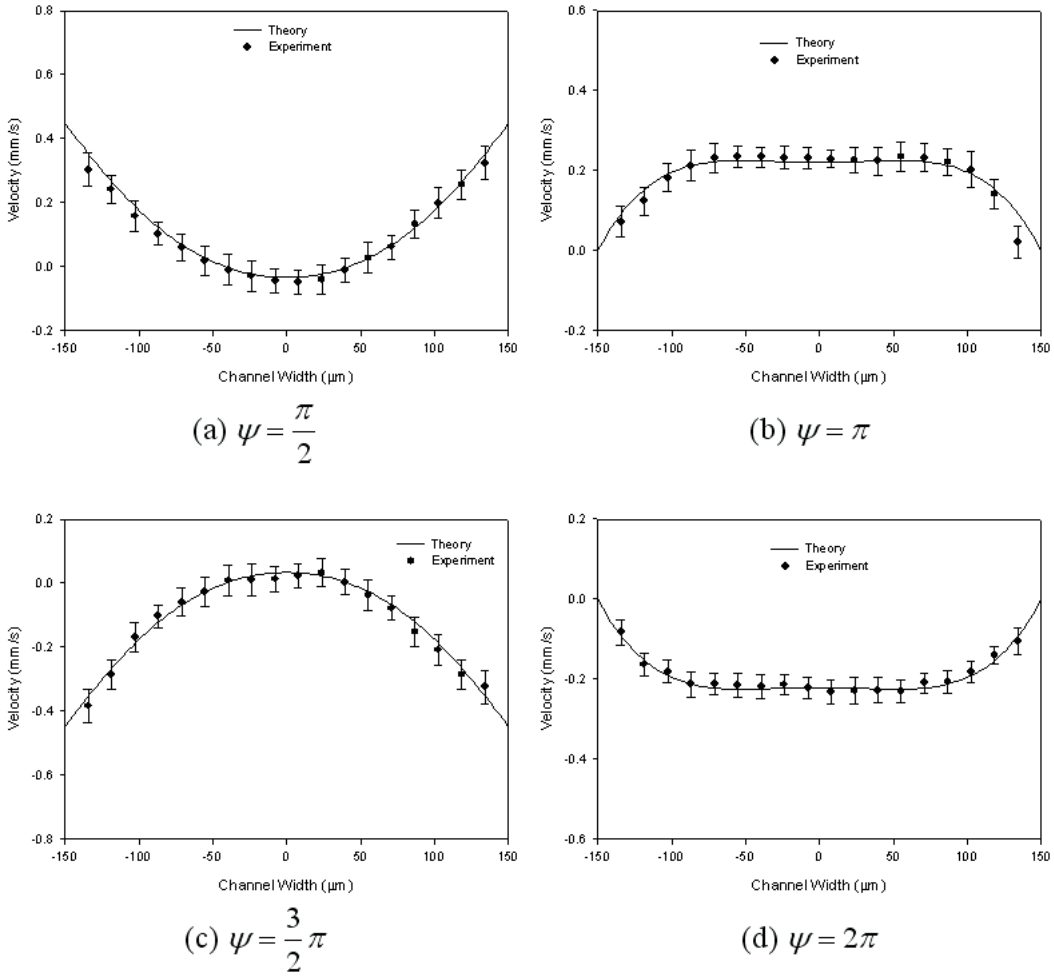

Figure 5.6 Plots for the velocity data of frequency-dependent EOF in an open-end channel at four phases during an AC cycle ($f = 50$ Hz).

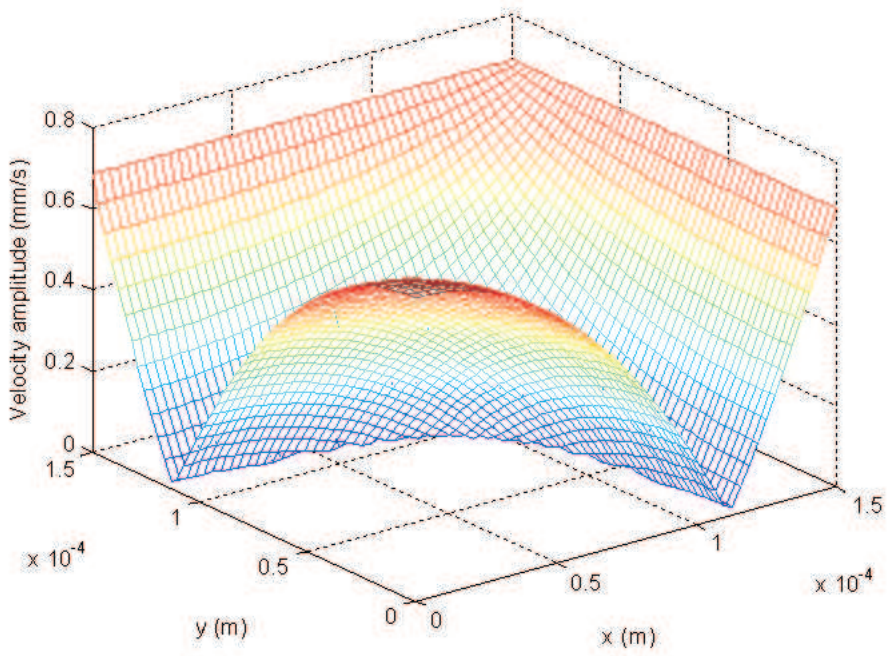

Figure 5.7 Velocity amplitude in a closed-end rectangular channel ($f = 20$ Hz).

5.4.1.2 Closed-end channel

Different from the EOF in an open-end channel, no analytical solution is available for the EOF velocity distribution in a closed-end channel. Based on Eqs. (5.12) and (5.13), one can utilize the numerical Laplace inversion to obtain the predicted velocity results. Alternatively, according to Section 5.2, we can use a more convenient method that is based on the Frequency Domain Analysis to obtain the velocity amplitude of the flow in steady state. Under the experimental conditions of $f = 20$ Hz, $E_1 = 0$ and $E_0 = 100$ V/cm, we computed the velocity amplitude distribution, and the results are shown in Figure 5.7. Very different from the case shown in Figure 5.4, it is noted that the amplitude distribution does not exhibit a plug-like profile; instead, in a narrow region between the channel wall and the center, velocity amplitude is small. This fact can be explained as below. Because of the closed-end structure an induced backpressure is developed to ensure a zero flow rate. The flow in fact is a superposition of and EOF near the channel wall and a backpressure-driven flow in the channel center region.

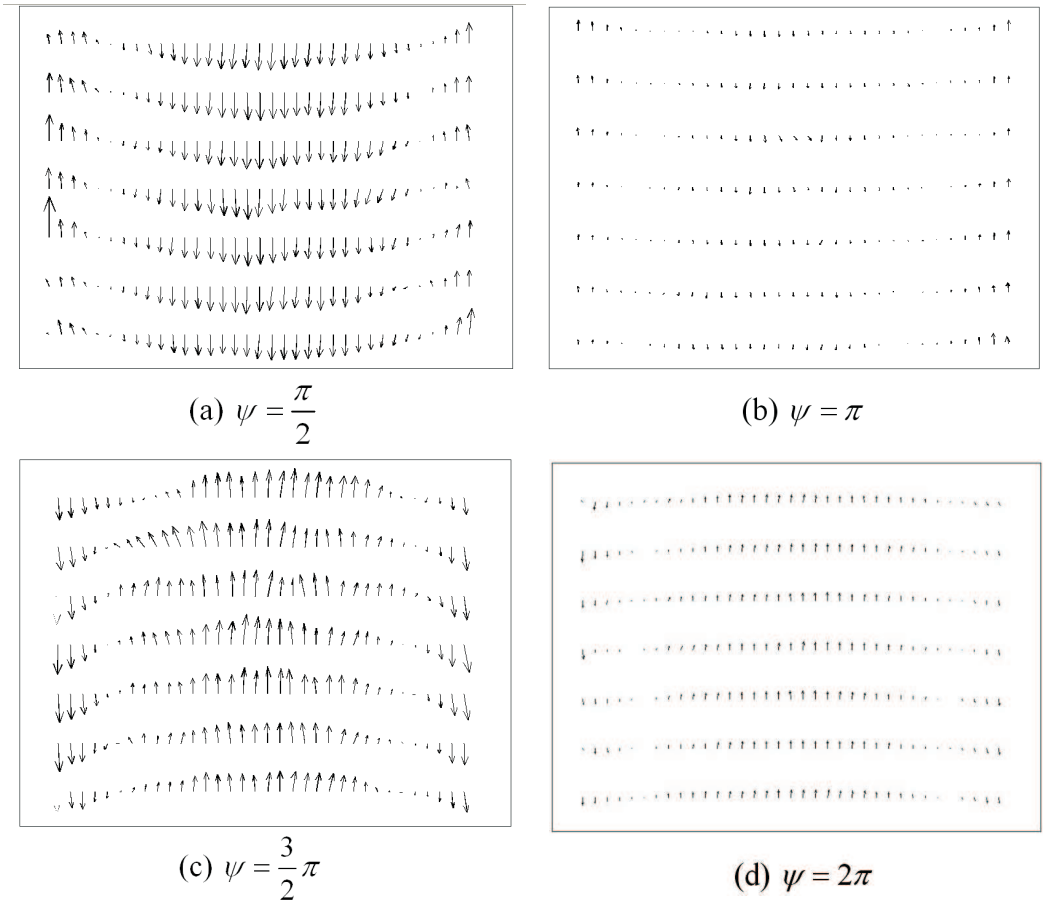

Figure 5.8 Micro-PIV measurements of the velocity distributions of frequency-dependent EOF in a closed-end channel at four phases during an AC cycle ($f = 20$ Hz).

The processed experimental results from the micro-PIV measurements are presented in Figure 5.8, from which it is observed that there is a narrow region where velocity amplitude is small at all the four phases. In fact, under low frequency, the position at which the amplitude is close to zero is just the stationary level occurred under the DC condition. The comparisons of experimental results and simulation are shown in Figure 5.9, and reasonable agreement is found.

5.4.2 Combined DC/AC driven EOF velocity distribution in an open-end channel

As shown in Eq. (5.30), the combined DC/AC driven EOF in an open-end channel in fact is a linear superposition of a DC EOF and an AC frequency-dependent EOF.

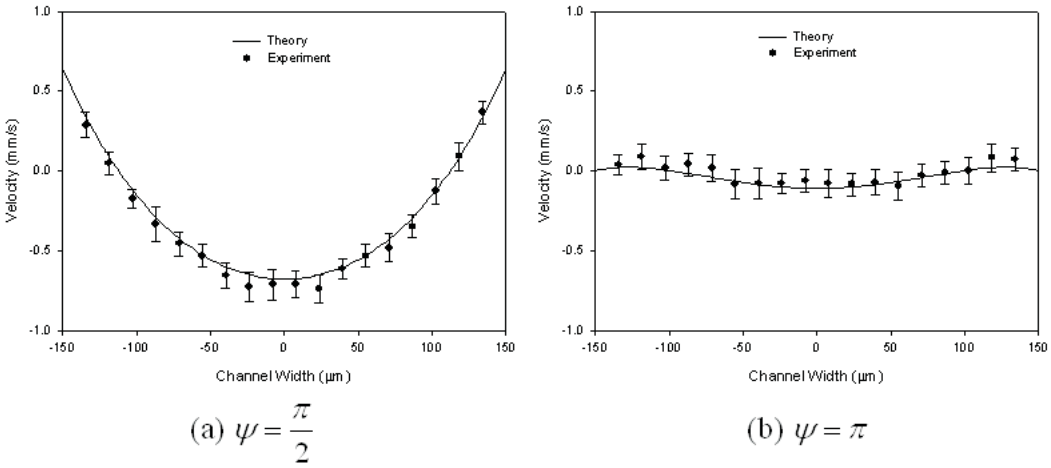

(a) $\psi = \frac{\pi}{2}$ (b) $\psi = \pi$

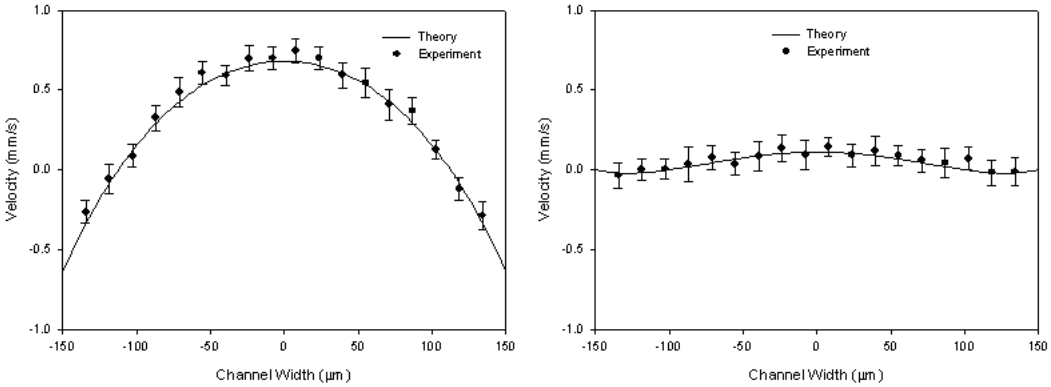

(c) $\psi = \frac{3}{2}\pi$ (d) $\psi = 2\pi$

Figure 5.9 Plots for the velocity data of frequency-dependent EOF in a closed-end channel at four phases during an AC cycle ($f = 20$ Hz).

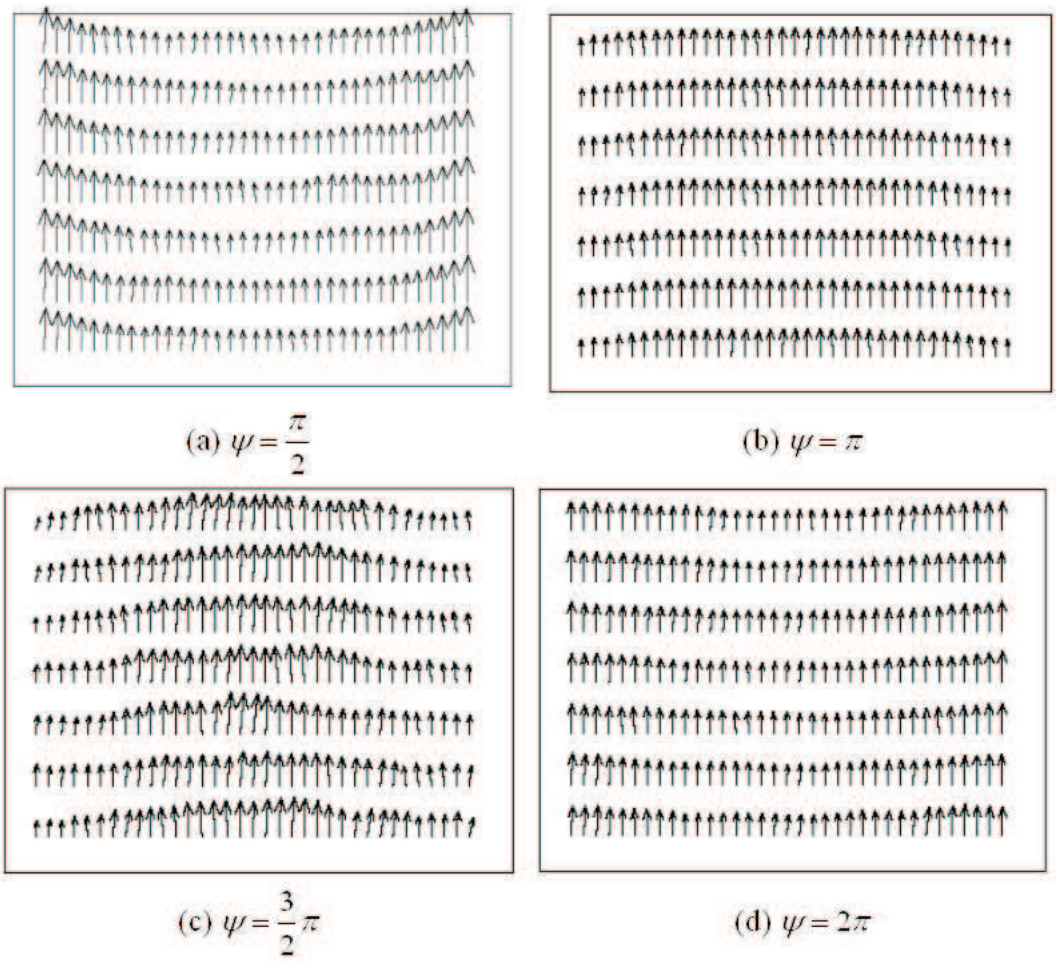

Figure 5.10 Micro-PIV measured velocity distributions of a DC/AC combined EOF in an open-end channel at four phases during a cycle (f = 20 Hz).

In the experiment, E_1 = 150 V/cm, E_0 = 75 V/cm and f = 20 Hz were chosen. The processed micro-PIV measurement results are shown in Figure 5.10. It can be seen that the velocity profile is in AC oscillating state but with a DC-driven main direction; this guarantees the pumping needs in practival applications. Because this flow pattern provides a possibility of pumping and oscillating the fluid simultaneously, it has potential application in a throughput micromixing system. Figure 5.11 shows a comparison of the experimental data and the simulation results.

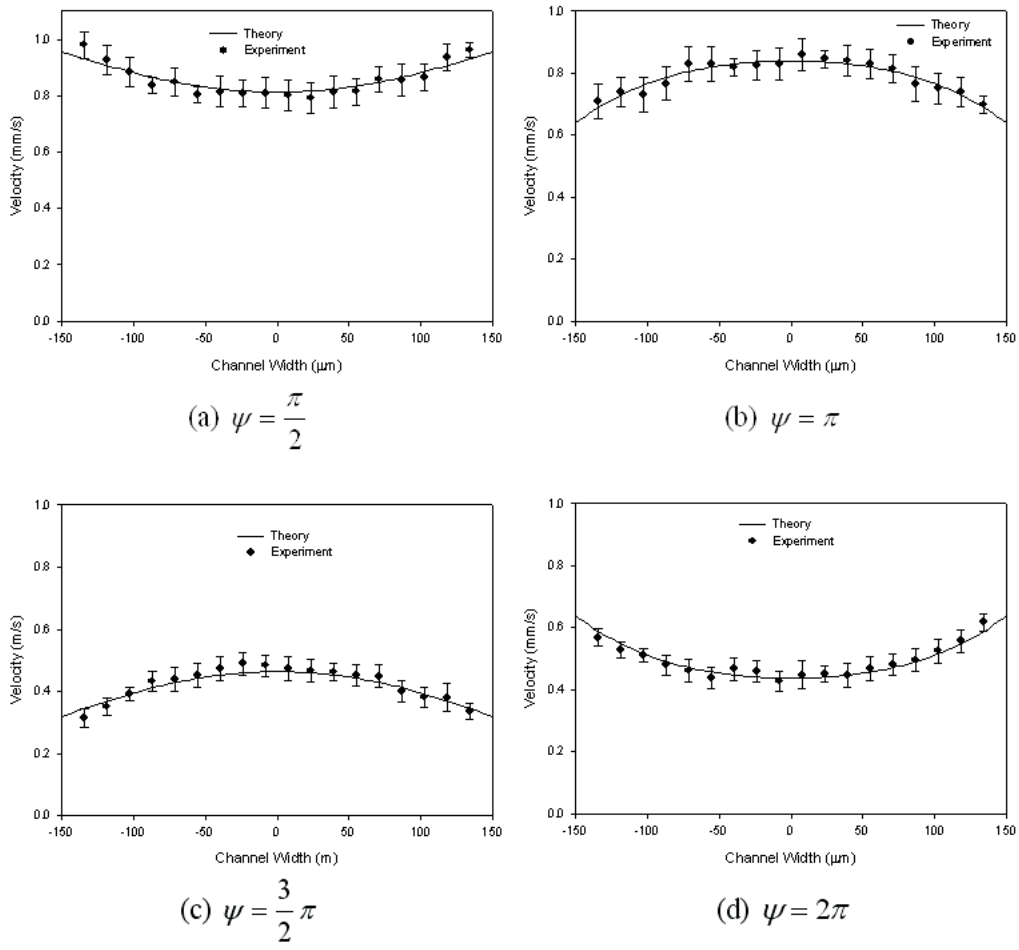

Figure 5.11 Plots for the velocity data of a DC/AC combined EOF in an open-end channel at four phases during a cycle ($f = 20$ Hz).

5.5 Summary

In this chapter, a method that combines the Laplace transform and Frequency Domain Analysis to analyze the EOFs in both open- and closed-end rectangular microchannels was presented. The obtained analytical solution can provide insight into the physical phenomena of the frequency-dependent EOF. Further, using the micro-PIV technique, the frequency-dependent electroosmotic flows in open- and closed-end microchannels were characterized. By precisely synchronizing equipment and removing electrophoretic velocity of the tracer particles, the velocity distributions of the frequency-dependent electroosmotic flows under various conditions were measured. A comparison of the experimental data and the simulation results shows a reasonable agreement. It should be noted that under low frequency (*e.g.*, 20 Hz used in experiment) the velocity profiles of EOFs in open- and closed-end microchannels present different characteristics; the velocity profile in open-end channel has a uniform amplitude, which means the oscillation of the flow is fully-developed across the channel. However, due to zero-net flow rate in the closed-end channel, the velocity profile has a non-uniform amplitude distribution, which shows a combined electroosmosis-driven flow near the channel wall and induced backpressure-driven flow on the central region of the channel. We also investigated the combined DC/AC driven EOF in open-end microchannels and observed the flow pattern which exhibits both a constant velocity and an oscillating component. Since the constant velocity can be used for fluid pumping and the oscillating part for convective mixing, this flow pattern may have potential microfluidic applications.

Chapter 6

Electrokinetic Micromixing Using Frequency-Dependent Electroosmotic Flow

6.1 Introduction

In Chapter 5, we have analyzed the frequency-dependent electroosmotic flows in microchannels and measured the oscillating velocity profiles. With the advantage of no moving parts in an electrokinetically-driven microfluidic system, a promising application of the frequency-dependent EOF is to utilize its fluctuating feature in electrokinetic micromixing. T-mixer is a widely used device in microfluidic applications, because it has a simple geometry and can perform mixing and sample transport simultaneously. Both theoretical and experimental studies on electrokinetic T-mixer have been reported in the literature (MacInnes, 2002, Johnson *et al.*, 2002, Glasgow *et al.*, 2004, and Lin *et al.*, 2004). In these studies, the researchers focused on either numerical analysis or experimental characterization.

The present study presents a systematical investigation on the performance and optimization of an electrokinetic T-mixer by analyzing the influences of the frequency and amplitude of the external electric field, EOF velocity distributions, and the channel

geometry with patterned blocks. Besides numerical simulations, experimental measurements were carried out using micro-PIV technique to determine the EOF velocity distribution and Rhodamine B visualization to characterize the mixing performance.

The current study mainly investigates two aspects of the electrokinetic T-mixer: (1) an active approach to utilize the frequency-dependent electroosmotic flow to increase the convective mixing effect in T-junction region; (2) a passive approach to enhance mixing by using the geometry effect of the microchannel with patterned blocks. In addition, a novel design of electrokientic micromixer is proposed using low frequency based AC electric field and fabricated electrode effects. Numerical simulations are performed to demonstrate the viability of the design.

6.2 Theory and Numerical Simulation

The electrokinetic micromixing is a complicated process involving electric field and mass and momentum transport. For a sophisticated channel geometry, it is almost impossible to obtain analytical solutions. However, computational fluid dynamics (CFD) has proven to be an effective tool for providing insightful analysis into the transport phenomena in microfluidic systems.

6.2.1 Mathematical formulation

In the present study, it is assumed that the fluid is incompressible with constant properties. The electrolyte solutions are dilute and the Joule heating effect is negligible. Because of the fact that a typical Debye layer thickness varies from a few to hundred nanometers, which is at least two to three orders smaller than the channel dimension of typical microfluidic devices, the slip velocity approach can be used. Thus, the fluid velocity at the wall can be prescribed using the Helmholtz-Smoluchowski equation (Santiago, 2001):

$$\boldsymbol{u}_{\mathrm{w}} = -\frac{\varepsilon \zeta_{\mathrm{w}}}{\mu} \boldsymbol{E} \tag{6.1}$$

where u_w is the fluid velocity at the wall, $\varepsilon = \varepsilon_r \varepsilon_0$ is the permittivity of the electrolyte solution, ζ_w is the zeta potential of the channel surface, μ is the dynamic viscosity of the fluid, $\boldsymbol{E}$ and is the local electric field vector at the wall. The electric field is obtained from the distribution of the electric potential, Φ, with

$$\boldsymbol{E} = -\nabla\Phi \tag{6.2}$$

Laplace equation determines the electric potential, which reads

$$\nabla^2\Phi = 0 \tag{6.3}$$

With the slip boundary conditions, the velocity flow field is governed by the continuity and Navier-Stokes equations:

$$\nabla \cdot \boldsymbol{V} = 0 \tag{6.4}$$

$$\rho\left[\frac{\partial \boldsymbol{V}}{\partial t} + (\boldsymbol{V}\cdot\nabla)\,\boldsymbol{V}\right] = -\nabla p + \mu\nabla^2\boldsymbol{V} \tag{6.5}$$

where ρ is the density of the fluid and p is the pressure. The Navier-Stokes equations can be non-dimensionalized by introducing

$$\bar{\boldsymbol{r}} = \boldsymbol{r}/W \qquad \bar{t} = t/\tau \qquad \overline{\boldsymbol{V}} = \boldsymbol{V}/U \tag{6.6}$$

$$\bar{p} = p/P_0 \qquad \overline{\nabla} = W\nabla \qquad \overline{\nabla}^2 = W^2\nabla^2 \tag{6.7}$$

where $\boldsymbol{r}$, t, $\boldsymbol{V}$, and p are the position vector, time, local velocity vector, and pressure, respectively. These quantities are normalized using W, $\tau = W/U$, U, and $P_0 = \mu U/W$, which are the width of the channel downstream from the T-junction, characteristic time scale, characteristic flow velocity, and characteristic pressure, respectively. Thus the continuity equation can be written down as

$$\overline{\nabla} \cdot \overline{\boldsymbol{V}} = 0 \tag{6.8}$$

and the Navier-Stokes equation,

$$\mathrm{Re}\left[\frac{\partial \overline{\boldsymbol{V}}}{\partial \bar{t}} + (\overline{\boldsymbol{V}} \cdot \overline{\nabla})\overline{\boldsymbol{V}}\right] = -\overline{\nabla}\bar{p} + \overline{\nabla}^2\overline{\boldsymbol{V}} \tag{6.9}$$

where $\mathrm{Re} = \rho UW/\mu$ is the Reynolds number, which represents the ratio of the inertial to viscous force.

Mass transfer is described by the species mass transport equation, which governs the convection and diffusion transport of individual species (without chemical reactions):

$$\frac{\partial c}{\partial t} + (\boldsymbol{V} \cdot \nabla)\, c = D\nabla^2 c \tag{6.10}$$

where c is the concentration of the species. By introducing the nondimensional concentration

$$\bar{c} = \frac{c}{c_{\max} - c_{\min}} \tag{6.11}$$

where $c_{\max}$ and $c_{\min}$ are the maximum and minimum of the concentrations at the two inlets (shown in Figure 6.1). Eq. (6.10) can be non-dimensionalized as

$$\frac{\partial \bar{c}}{\partial \bar{t}} + \left(\overline{\boldsymbol{V}} \cdot \overline{\nabla}\right) \bar{c} = \frac{1}{\mathrm{Pe}}\overline{\nabla}^2\bar{c} \tag{6.12}$$

where the coefficient Pe is the Peclet number defined as:

$$\mathrm{Pe} = \frac{UW}{D} \tag{6.13}$$

The Peclet number represents the ratio of mass transport due to convection to diffusion. With an assumption of uniform electrical conductivity throughout, the electric field is not influenced by the concentration field because of dilute solute concentrations.

For quantifying the degree of mixing effects from the numerical simulation results, we employ a method used by Jeon *et al.* (2000). This method is based on the standard deviation of the normalized concentration profile from that of the perfectly mixed case,

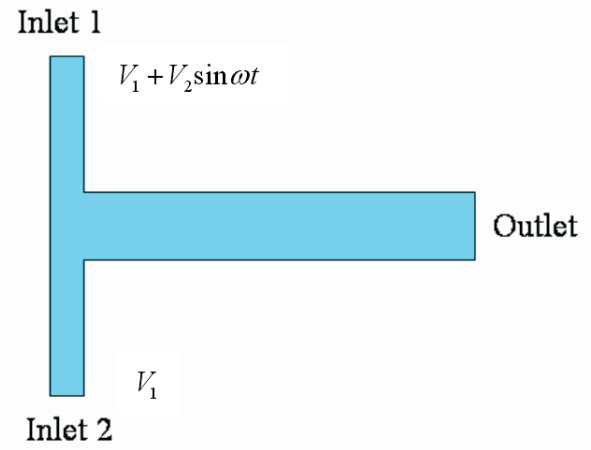

Figure 6.1 A T-mixer with two inlets and one outlet (not to scale).

under which 100% mixing is reached. The mixing efficiency σ is defined as

$$\sigma = 1 - \frac{\sqrt{\frac{1}{N}\sum_{i=1}^{N}(\bar{c}_i - \bar{c}_\infty)^2}}{\sqrt{\frac{1}{N}\sum_{i=1}^{N}(\bar{c}_{0i} - \bar{c}_\infty)^2}} \tag{6.14}$$

where N is the total number of points examined in the cross-stream direction, $\bar{c}_i$ is the normalized concentration at each point, $\bar{c}_{0i}$ is the normalized concentration at each point with no mixing taking place (value 0 or 1), and $\bar{c}_\infty$ is the normalized concentration in the complete mixing states (value 0.5).

6.2.2 Numerical method

In the present work, we have chosen COMSOL Multiphysics^{TM} software (User's Guide, 2006) for performing numerical simulations. COMSOL Multiphysics^{TM} is a general partial differential equation solver using the finite element method (FEM) and has several modes to solve microfluidic problems, such as MEMS and Chemical engineering Modules. One of the most important features of COMSOL Multiphysics^{TM} is that it can conveniently couple multiphysical models and then solve the problem effectively. In the present study, electrokinetic mixing in microfluidic microchannels involves time-dependent electric field, flow field, and concentration field. Using COM-

Table 6.1 Boundary settings in AC EK mixing.

Boundaries	Conductive Media DC (dc)	Incompressible Navier-Stokes (ns)	Convection and Diffusion (cd)
Inlet 1	Voltage: $V_1 + V_2 \sin(2\pi f t)$	Outflow/Pressure: 0	Concentration: c_1
Inlet 2	Voltage: V_1	Outflow/Pressure: 0	Concentration: c_0
Outlet	Voltage: Ground	Outflow/Pressure: 0	Convective flux
Channel surfaces	Electric insulation	Slip velocity	Insulation/Symmetry

SOL Multiphysics^{TM}, the problem can be solved by coupling three modes, which are "conductive media DC", "incompressible Navier-Stokes" and "convection and diffusion".

According to MacInnes' study (2002) on electrokinetic mixing in T-mixers, 2D simulations can provide very close results to that of 3D's. In fact, for low Reynolds number electroosmotic flow in microfluidic channels with uniform surface, the velocity field is similar to the electric field (Santiago, 2001). Hence we mainly employ 2D models to simulate the electrokinetic mixing processes.

With COMSOL Multiphysics^{TM}, three modes are used to set the boundary conditions for electrokinetic mixing in a T-mixer (Figure 6.1) as follows. In the mode of "conductive media DC", we set various potentials at the inlets, electric ground at the outlet, and electric insulation on the channel surfaces. In the mode of "incompressible Navier-Stokes", we set zero pressure at both the inlets and the outlet, and the slip boundary conditions on the channel surfaces (determined by Eq. (6.1)). For the mass transport mode of "convection and diffusion", we set boundary conditions of two inlets with constant concentrations (c_0 and c_1), insulation/symmetry on the channel surfaces, and convective flux at the outlet. In summary, the choice of boundary conditions for AC EK mixing is shown in Table 6.1. Using these treatments, we make the model in good match to the experimental conditions. Due to the time-dependent and frequency-dependent nature of the electrokinetic mixing process, time-dependent solver is used to do numerical simulations.

In the simulation, the physical properties are taken to be the same as those of

water, whose density, viscosity, conductivity and dielectric constant are 1000 kg m^{-3}, 9×10^{-4} N s m^{-2}, 5.5×10^{-6} S m^{-1} and 80, respectively. Rhodamine B is used, and its diffusion coefficient in water at room temperature is 3.6×10^{-6} cm^2 s^{-1} (Rani *et al.*, 2005). In addition, due to its electrically neutral property, the Rhodamine B can be treated as uncharged species. According to Ren *et al.* (2001), the electroosmotic mobility of the PDMS and the glass is $\mu_{mob} = 3.0 \times 10^{-4}$ cm^2 V^{-1} s^{-1}. The geometry and sizes of different channel designs will be described in the next experimental section.

6.3 Experimental Section

6.3.1 Design and fabrication of the microchannels

Three microchannel structures were designed in this work, namely T, T1 and T2, which are shown in Figure 6.2. All the channels have a depth of 100 μm. Design T is a straight rectangular channel with two inlets and one single outlet. This is a typical T-mixer design. Design T1 is a channel with two inlets and one single outlet. Along the mixing channel, the channel width is repeatedly constricted. The narrowing of the channel aims to achieve better mixing due to the shorter diffusion distance. Design T2 is a channel with two inlets and one single outlet. Along the mixing channel, the flow is repeatedly controlled to flow up and down around the bends, thus inducing lateral velocity and resulting in better mixing.

6.3.1.1 Fabrication techniques

The microchannels used in the experiment were fabricated by using rapid prototyping techniques, which include the photolithography technique for master fabrication and Soft Lithography technique for PDMS microchannels replication (Duff *et al.*, 1998).

Photolithography is the key technology in MEMS fabrication. Photolithography is the process of transferring geometric shapes on a mask to the surface of a material coated with photoresist, and it involves three sequential steps, as described below.

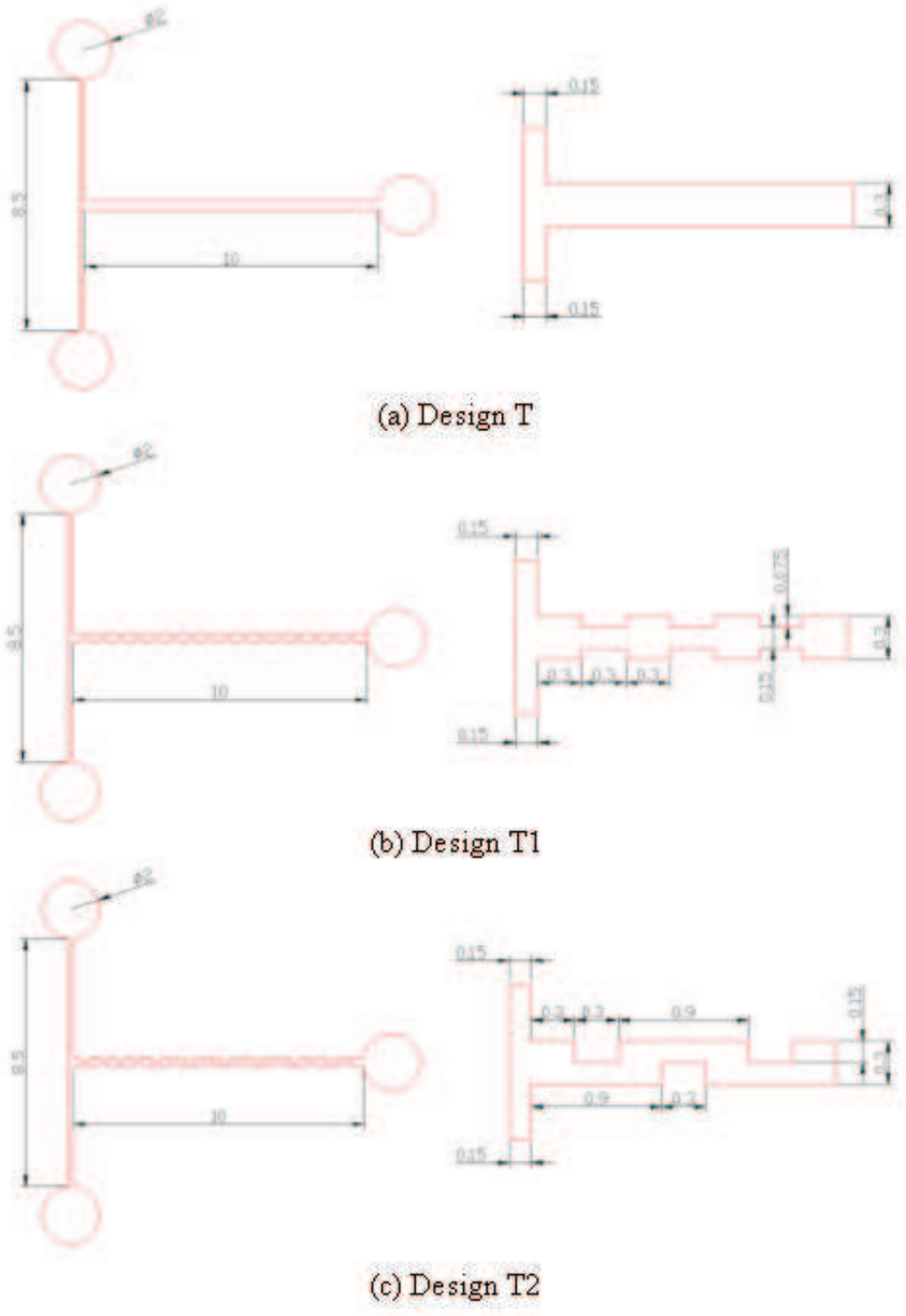

Figure 6.2 Dimensions of three designs and enlarged views at T-junction (Units: mm).

- Deposition of photoresist film onto the wafer by spin-coating;
- Optical exposure to print an image of the mask onto the resist;
- Immersion in an aqueous developer solution to dissolve the exposed resist and render visible the latent image.

Normally, two types of photoresists are available, namely, the positive and the negative types. For positive resists, the underlying material that is to be removed will be exposed to UV light. For these resists, exposure to the UV light changes the chemical structure of the resist hence, enabling it to become more soluble in the developer. The exposed resist is then washed away by the developer solution, leaving windows of the bare underlying material. The mask, therefore, contains an exact copy of the pattern that is to remain on the wafer. Negative resists behave in the opposite manner. Portions that are exposed to the UV light will result in polymerization of the photoresist, and hence these regions are more difficult to dissolve. Therefore, when immersed in the developer solution only the unexposed portions are removed and the negative resist remains on the surface wherever it is exposed. Masks used for negative photoresists, therefore, contain the inverse of the pattern that is to be transferred.

After a glass side has been coated with resist and suitably soft-baked, it was aligned to the corresponding mask for UV exposure to create a latent image in the photoresist. The degree of exposure was adjusted by controlling the light intensity and exposure time. In the fabrication process, the glass side was aligned properly on the OAI machine (Optical Associates Inc., Model J500-IR/VIS, Mask Aligner, see Figure 6.3), with the transparency mask placed above. Then the SU8 coated glass slide was exposed to UV light for 2 min and 20 sec at $350 \sim 400$ nm. Although SU8 is virtually transparent, it is insensitive to wavelength of light above 400 nm and has maximum absorption when wavelength is below 350 nm. However, excessive dose below 350 nm may, therefore, result in over exposure of the top portion of the resist hence, resulting in an exaggerated profile of the sidewall.

Soft Lithography, which represents an alternative set of techniques for fabricating

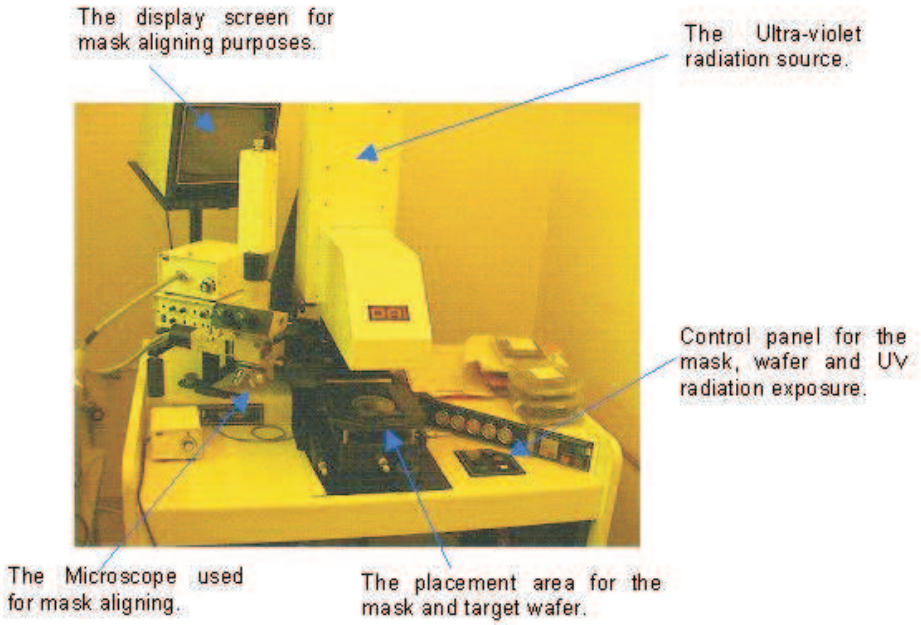

Figure 6.3 Photo of the exposure machine (Optical Associates Inc., Model J500-IR/VIS, Mask Aligner).

micro- and nanostructures, is a microfabrication process on which a soft polymer, such as poly (dimethylsiloxane) or other elastomers, is casted on a mold that contains a microfabricated relief or engraved pattern. That is, the elastomeric stamp is prepared by cast molding: whereby the pre-polymer of the elastomer is poured over the master having a relief structure on its surface, and then is cured and peeled off. Figure 6.4 outlines the process of PDMS casting.

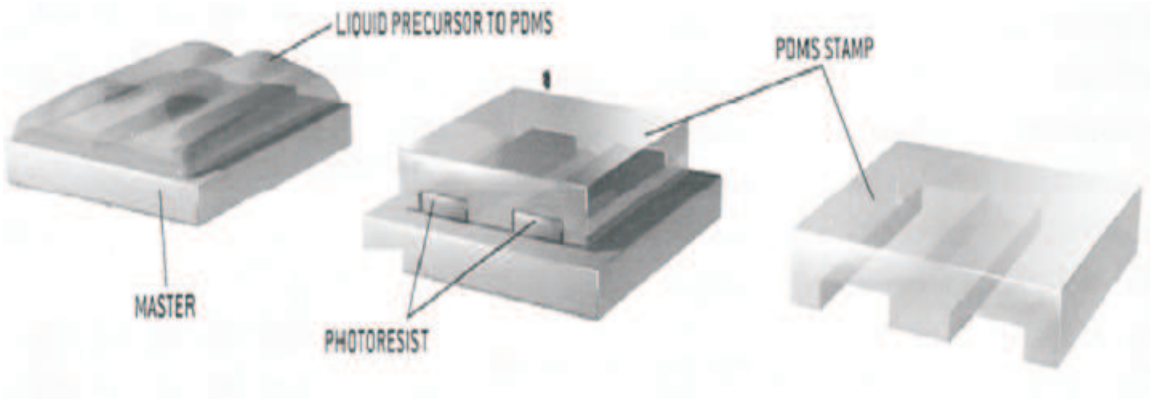

Figure 6.4 Illustration of PDMS casting.

6.3.1.2 Fabrication of the microchannels

The mask design is based on the concept and design of the microchannels used in the experiments. In this work, three kinds of mask patterns (*i.e.*, the designs of T, T1 and T2) were first designed using the AutoCAD software, and then the Auto CAD files were printed on a flexible transparency by using a commercial high-resolution printer.

The master is fabricated by using the photolithography techniques. To create the microchannel molds onto a Si wafer, negative photoresist SU8-50 (Microchem Corp.) is used. The PDMS microchannel was fabricated by using the Soft lithography techniques. Soft lithography was discovered by Duffy *et al.* (1998). It is a faster, cheaper and less specialized way of fabricating devices. The main sequential steps are described as follows.

a) PDMS replica molding of master

Liquid PDMS was prepared by thoroughly mixing the PDMS pre-polymer (SYLGARD 184 Silicone elastomer kit, Dow Corning, Midland, MI) and the curing agent, in the weight ratio of 10 : 1. Caution was used to avoid the contact of latex rubber (gloves) and liquid PDMS, as this would inhibit curing (Erickson *et al.*, 2003). The mixture was then left for about 1 hour to allow the air bubbles in the mixture to burst. Then the mixed liquid PDMS was poured over the master and cured at a temperature of 65 °C for 2 hours.

Then the PDMS replica of the master containing a negative relief of microchannels was peeled away from the master. The angle of the walls of the photoresist to the substrate is close to 90°, therefore the microchannels in the PDMS replica were essentially rectangular as shown in Figure 6.5, which presents the SEM images of the channels in PDMS created by the polymer against a positive relief of photoresist for the channels of different designs. The roughness in the side wall of the PDMS channels arises from the limited resolution of the transparency used as a mask in photolithography to create the positive relief of photoresist.

b) Oxidizing and Bonding the PDMS replica and flat slab (PDMS or glass slide)

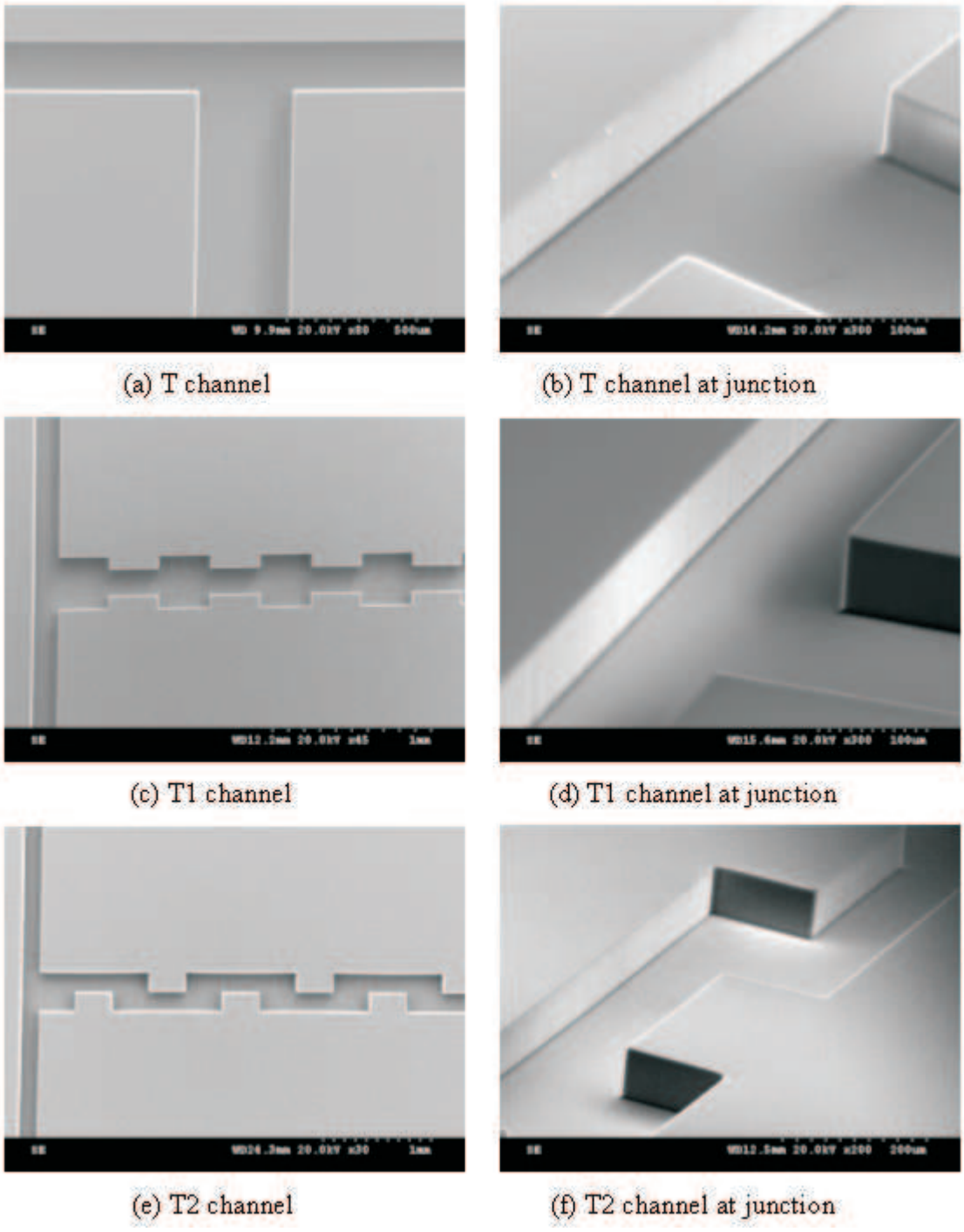

Figure 6.5 Scanning electron microscopic (SEM) images of the PDMS microchannels. (a) T channel, (b) T channel at junction, (c) T1 channel, (d) T1 channel at junction, (e) T2 channel, (f) T2 channel at junction.

After the PDMS channels were peeled off from the master, the reservoirs were punched through with a 1-hole puncher. To form enclosed microchannels, the PDMS replica containing the microchannel should be irreversibly bonded with a flat slab of PDMS or glass slide. According to Duffy *et al.* (1998), the oxidized PDMS has hydrophilic surface, and it is easy to fill the microchannels in their experiments by placing liquid in three of the reservoirs and apply vacuum on the fourth due to the strong bond of the oxidized PDMS. On the other hand, it is difficult to fill the microchannels defined by the hydrophobic, conformal contact between an untrated PDMS replica and flat by vacuum because two pieces of PDMS tended to be pulled apart by the force of suction since the untreated PDMS has a hydrophobic surface.

Chaudhury (1991) also pointed out that the bond between the two pieces of oxidized PDMS was sufficiently strong that the two substrates could not be peeled apart without failure in cohesion of the bulk PDMS.

During the process of microchannels fabrication, we also checked the hydrophobicity of the PDMS surface by measuring contact angles with FTA 200 instrument. A drop of deionised water was dropped onto both untreated and oxidized surfaces of two pieces of PDMS, and was later analyzed using the FTA software (see Figure 6.6). The figure demonstrates that the original PDMS (untreated) surface is hydrophobic, while the oxidized PDMS surface is hydrophilic.

In order to obtain strong bond between the substrate and the hydrophilic wall surface enclosing the microchannels, the PDMS replica and the flat slabs of PDMS or cleaned glass slides were undergone the Oxygen Plasma process using the RIE machine (TECHNICS, Micro-RIE, Series 900-11) as shown in Figure 6.7.

The O_2 plasma process, uses 150 W for power, at 84 mTorr, gas flow at 10 sccm. The specimens then undergo exposure of plasma for 2 min. During our fabrication, it was found that PDMS replica that were just removed from the master and cleaned glass slides, yielded the best bonding between the glass slide and the PDMS channel when subjected to O_2 plasma. After the PDMS was put onto the glass slide, leave it for about 15 minutes for completing the bonding process. The PDMS/glass microchannels

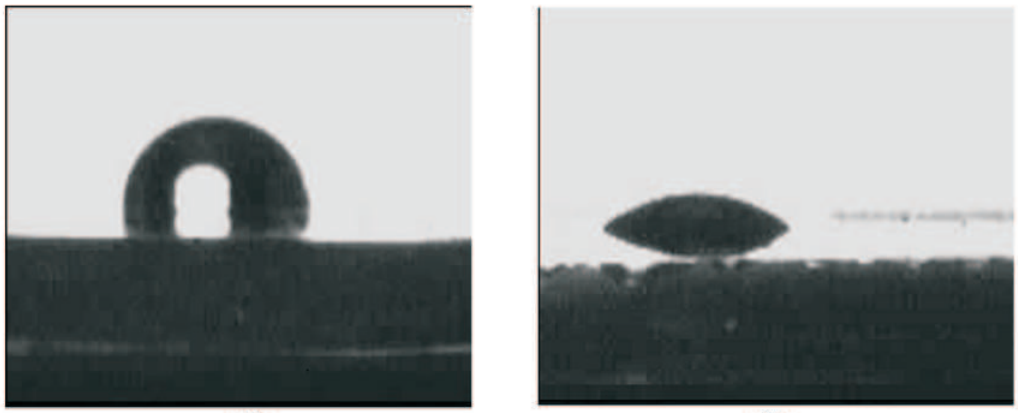

Figure 6.6 Test for the hydrophobicity of the PDMS surface: (a) before oxygen plasma treatment, and (b) after oxygen plasma treatment.

ready for measurements are shown in Figure 6.8.

6.3.2 Preparation of chemicals

Laser grade Rhodamine B dye (Acros Organics, Pittsburgh, USA) and DI water were used in the test. Rhodamine B is a water-soluble fluorescent dye, which can be excited by green light and emits red light (wavelength of 610 nm). The diffusion coefficient of Rhodamine B in water at room temperature is 3.6×10^{-6} cm^2 s^{-1} (Rani *et al.*, 2005). Rhodamine B was initially dissolved in DI water. The test solutions were filtered using a 0.2 μm syringe filter before the test.

For velocity measurement, the tracer particles were polystyrene fluorescent latex particles purchased from Duke Scientific. The particles of $d_p = 0.93$ μm in diameter have a maximum excitation wavelength of 540 nm (green) and a maximum emission wavelength of 610 nm (red). The number concentration of tracer particles was around 2×10^9 particles/ml.

6.3.3 Experimental techniques and image analysis

Both DC and AC tests were carried out to investigate how the electrokinetic flows will influence the mixing effects. In DC measurements, the voltage applied between

Figure 6.7 RIE machine used for oxygen plasma etching.

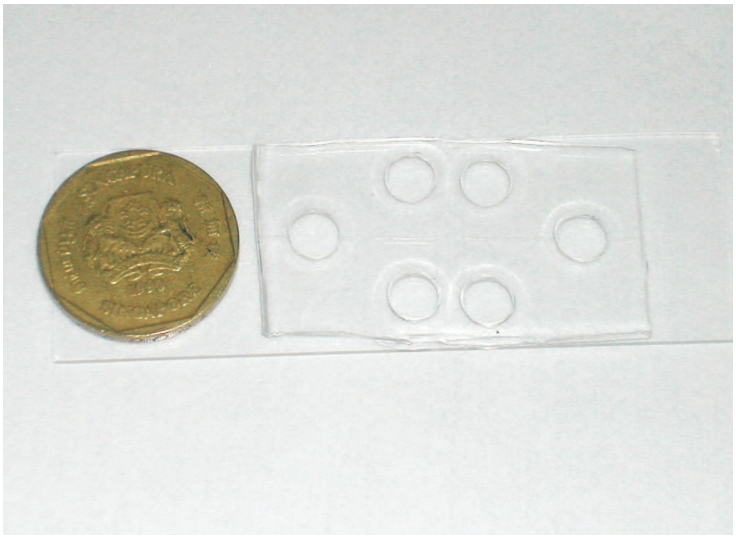

Figure 6.8 Bonded PDMS/Glass channel.

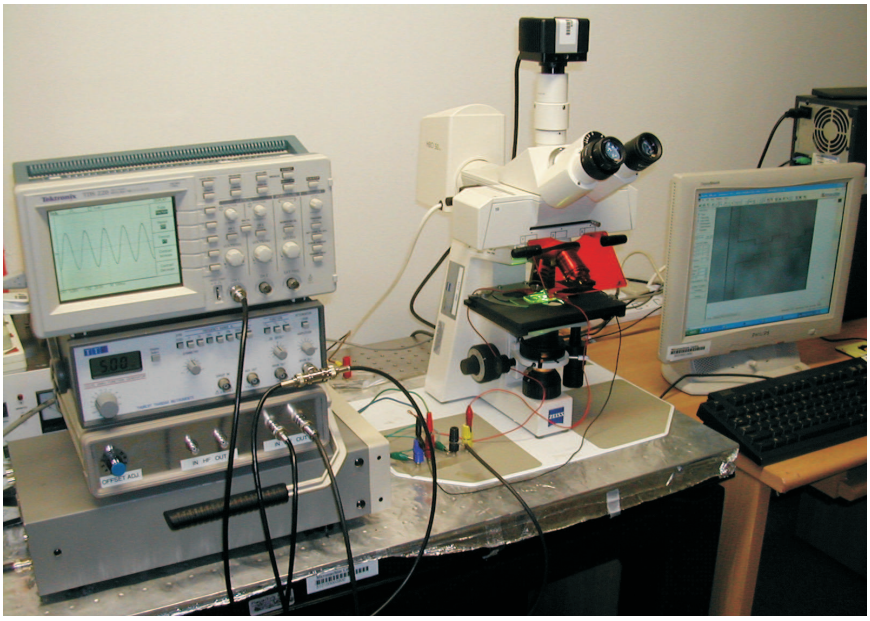

Figure 6.9 Experimental setup, including a function generator, an oscilloscope, a power amplifier, a DC high voltage power supply, a CCD camera, and a fluorescent microscope.

inlets and outlet was controlled by a high voltage power supply (Stanford Research). Electric field strength along the longitudinal direction was varied from 50 V/cm to 200 V/cm. In AC measurements, a power amplifier connected to a function generator was used to form the different waveforms so as to generate pulsed flows. An oscilloscope was used to monitor the wave forms of input and output signals. The electric field takes the form of a biased sinusoidal wave. The bias DC voltage is used to generate a base flow. The periodic component that varies at frequency of 0.1 Hz to 10 Hz produces the pulsed flow.

The experiment was performed with a fluorescence microscope (Zeiss). A mercury lamp (mbq 52 ac, Zeiss) was used for fluorescent excitation to view the Rhodamine B dye. The microscope has an appropriate filter set (excitation, 546 nm; emission, $>$ 590 nm) and objective lenses of 5×, 10× and 20×. A CCD camera was used to acquire the optical images, and a program, Sensovation SamBa EZ-series, IEEE 1394, recorded images at specified time intervals. A computer system was used to store and process images. The entire system is shown in Figure 6.9.

In the excitation intensity measurement, one reservoir contained deionized water

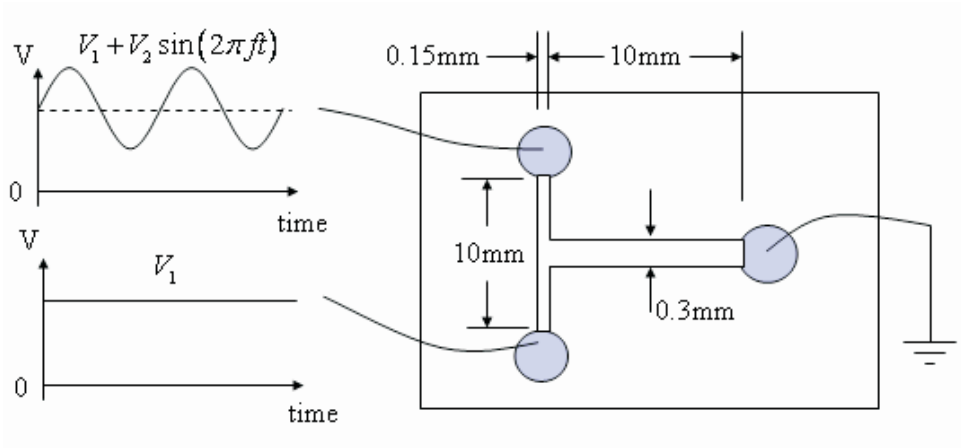

Figure 6.10 Schematic of voltage arrangement on the T-mixer.

and the other deionized water with a certain amount of Rhodamine B for visualization purpose. Platinum electrodes were inserted into both input reservoirs at the ends of the microchannel, and the output reservoir was connected with ground (see Figure 6.10). Before measurement, the reservoir fluid levels were carefully adjusted for balance so as to avoid reservoir-induced hydrodynamic backpressure.

For processing the images obtained from fluorescent measurement, a MATLAB based program was used to normalize the intensity and do the characterization. For a certain point in an image, the concentration c_i can be characterized as intensity value I_i, and the extreme values of concentration $c_{\max}$ and $c_{\min}$ correspond to $I_{\max}$ and $I_{\min}$, respectively. Similar to Eqs. (6.11) and (6.14), the fluorescent intensity I_i can be normalized as

$$\bar{I}_i = \frac{I_i}{I_{\max} - I_{\min}} \tag{6.15}$$

and the measured mixing efficiency is expressed as

$$\sigma_{\text{measured}} = 1 - \frac{\sqrt{\frac{1}{N}\sum_{i=1}^{N}\left(\bar{I}_i - \bar{I}_\infty\right)^2}}{\sqrt{\frac{1}{N}\sum_{i=1}^{N}\left(\bar{I}_{0i} - \bar{I}_\infty\right)^2}} \tag{6.16}$$

where N is the total number of points examined in the cross-stream direction, $\bar{I}_i$ is the normalized intensity at each point, $\bar{I}_{0i}$ is the normalized intensity at each point

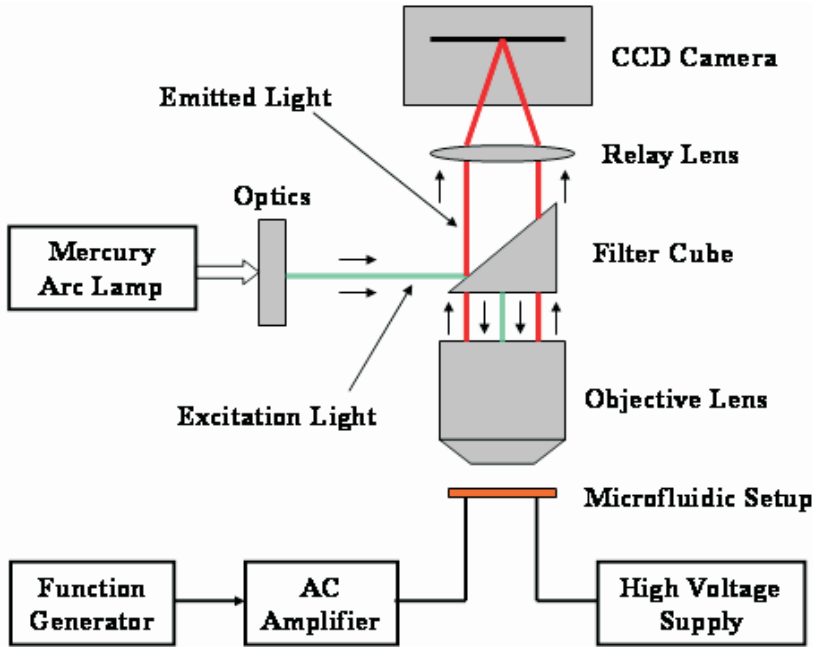

Figure 6.11 Schematic of the micro-PIV setup.

with no mixing taking place (value 0 or 1), and $\bar{I}_{\infty}$ is the normalized intensity in the complete mixing states (value 0.5).

For determining the velocity field in the mixing process, the fluorescent microscope with CCD camera and mercury lamp was also used as a micro-PIV system. The setup of micro-PIV consists of four main components: an illumination system, an optical system, a coupled charge device (CCD) camera and a control system. The control system and its corresponding software were implemented in a personal computer (PC). The PC can control and synchronize all actions related to illumination and image recording. The images obtained in measurements were evaluated with PIVview software (PivTec GmbH). The schematic of the micro-PIV setup is illustrated in Figure 6.11.

6.4 Results and Discussion

In general, there are several important factors that affect the electrokineitc micromixing in a T-mixer, and these factors are the frequency and amplitude of the external electric field, the channel size and channel geometry (straight or curved, patterned or not), and the velocity field. In this section, using the results obtained from

experiments and simulations, we will quantitatively compare and characterize the effects of these factors on electrokinetic micromixing in a T-mixer. Due to the low electric field strength applied ($\leq$ 200 V/cm) and low concentration of the electrolyte solution, the Joule heating effect was not considered in the present study (Tang *et al.*, 2003).

6.4.1 Effect of the electric field on mixing efficiency

Since the flow field is controlled by the electric field which can be adjusted by modulating its strength and frequency, in the following we will estimate the effective range of the strength and frequency of electric field.

6.4.1.1 Estimation of the effective range of the electric field strength

According to Johnson *et al.* (2002) and Lammertink *et al.* (2004), the diffusive mixing time of two co-laminar streams is proportional to the width of the channel, and the time required to obtain cross-stream mixing is in the scale of (Cussler, 1984)

$$\tau_{\text{diff}} \sim \frac{W^2}{2D} \tag{6.17}$$

where W is the channel width and D is the diffusion coefficient.

Another important time scale is the convective transport time, because in the current study one of our purposes is to improve mixing quality using convective effect. The convective transport time scale, τ_{conv}, is given by

$$\tau_{\text{conv}} \sim \frac{L}{u_{\text{eo}}} = \frac{L}{\mu_{\text{eo}} E} \tag{6.18}$$

where L is the channel length downstream from T-junction, u_{eo} is the fluid velocity at the channel wall, μ_{eo} is the electroosmotic mobility, and E is the electrical field strength. Due to the plug-like flow under DC electric field, the mixing performance only depends on pure molecular diffusion. In order to obtain rapid and full mixing at the exit, there is an optimum electric field strength, smaller than which the samples

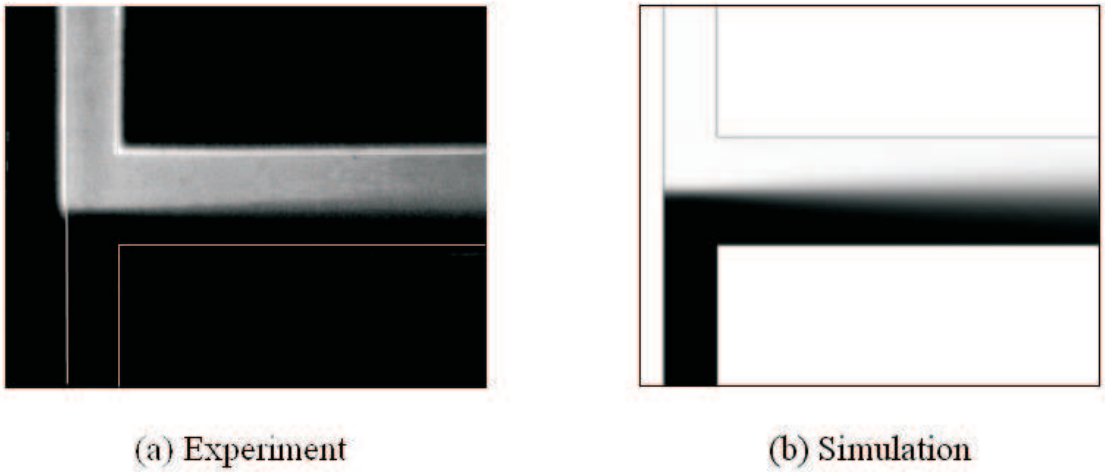

Figure 6.12 Electrokinetic mixing near T-junction under DC condition (V_1 = 150 V), (a) Experiment and (b) Simulation.

get fully mixed before reaching the exit, and larger than which the samples cannot get fully mixed when reaching exit. Obviously, the optimum electric field strength should meet $\tau_{\text{conv}} \sim \tau_{\text{diff}}$ which results in a simple relation for the optimum electric field strength in a DC electrokinetic T-mixer:

$$E_{\text{opt}} \sim \frac{2LD}{W^2 \mu_{\text{eo}}} \tag{6.19}$$

In experiment, $L = 1$ cm and $W = 0.3$ mm. If choosing $D = 3.6 \times 10^{-6}$ cm^2 s^{-1} (Rani *et al.*, 2005) and $\mu_{\text{eo}} = 3.0 \times 10^{-4}$ cm^2 V^{-1} s^{-1} (Ren *et al.*, 2001), the optimum electric field strength required for DC electrokinetic mixing is estimated to be 27 V/cm.

In both experiment and simulation, various base voltages (V_1) have been applied at the two inlets as 75 V, 150 V and 300 V, and correspondingly, the electric field strengths in the channel downstream of T-junction are 50 V/cm, 100 V/cm and 200 V/cm. Electric field strength higher than 200 V/cm was not utilized in order to avoid Joule heating effect, which can be significant in the case of long mixing time (Tang *et al.*, 2003). According to Figure 6.12, it can be observed that under DC condition the mixing is poor, but the comparison shows good agreement.

Figure 6.13 shows a comparison between simulation and experiment under effects of the DC field strength. In order to improve mixing quality and shorten the mixing

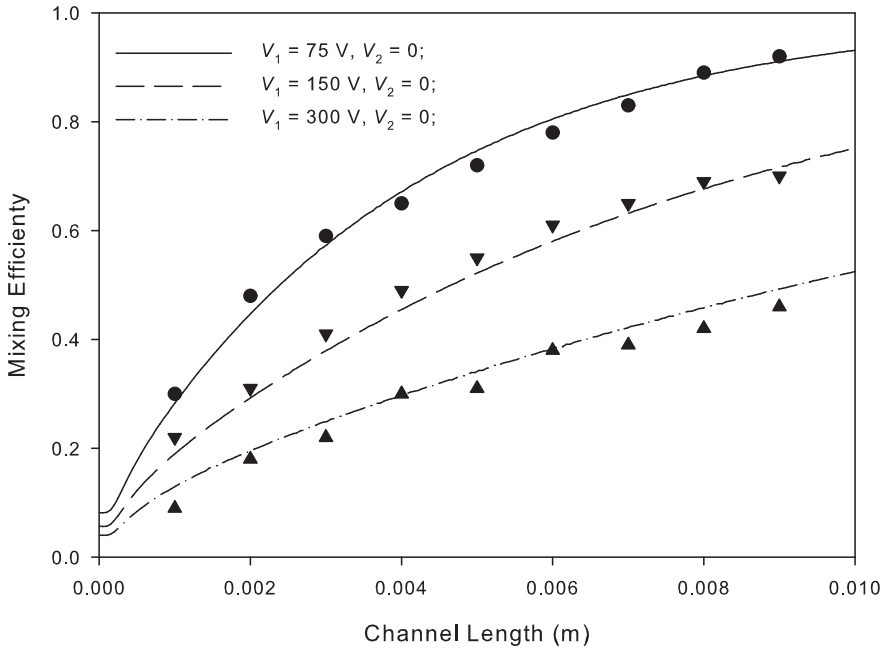

Figure 6.13 Simulated and experimental mixing efficiency under various electric field strengths. The lines represent the simulation results and the symbols denote the experimental data.

time, one effective method is to set the electric field close to E_{opt} so that the samples reach the exit and get fully mixed simultaneously. Extending the mixing channel while retaining high electric field strength is another option, under which high flow rates can be maintained, since the flow rate is proportional to the electric field strength. The extended channel length can be estimated using Eq. (6.19).

6.4.1.2 Estimation of the effective range of the oscillation frequency

One of the key issues of mixing is to increase the contact area between two initially segregated fluids (Ottino and Wiggins, 2003). Electrokinetic oscillating flow provides an effective way to increase the interfacial area for good mixing purpose. Under DC condition ($f = 0$), the flow velocity profile in the system is plug-like, and the two flows downstream are parallel. As a result, there is no convective effect on the sample solutes and thus the mixing mainly depends on molecular diffusion as shown in Figure 6.12. When the flow is driven by AC field, the flow becomes oscillatory and there will

be more contact area between two mixing streams. In addition, due to the nonuniform velocity field in the T-junction area, Taylor dispersion may be induced, which improves mixing effect.

The angular frequency of oscillation flow is relevant to the Strouhal number that is defined as

$$\mathrm{St} = \frac{\omega W}{U} \tag{6.20}$$

where ω is the angular frequency ($\omega = 2\pi f$). The Strouhal number represents the ratio of the residence time of a species to the time period of its disturbance in an active micromixer. Therefore, to exert an effective disturbance in the electrokinetic micromixer, the time period of the disturbance must be less than the residence time of a species; this gives

$$\frac{1}{\omega_{\mathrm{lower}}} < \frac{W}{U} \tag{6.21}$$

This leads to a criterion of lower frequency limit

$$\omega_{\mathrm{lower}} > \frac{U}{W} \qquad \text{or} \qquad \mathrm{St} > 1 \tag{6.22}$$

This criterion conveys the nature of the convection of the interface between the two fluids in the T-junction area, which means under a certain frequency the flow structure will be in banded composition in which the interface area between the two fluids is reduced and hence the mixing is poor. From experiments and simulations under low frequency, we also observed this phenomenon. So approximately, in the range of $0 < \mathrm{St} < 1$, the flow is in a parallel or a banded pattern, which is not good for improving mixing. In order to improve the mixing effect, we can increase the frequency (St), and thus the Strouhal number. However, from the discussions below, it will be found that there is an upper limit of the frequency beyond which the mixing effect is poor.

For the upper frequency limit, we notice that the frequency-dependent EOF in microchannels can be described as the Stokes' second problem. The Stokes penetration

depth (or Stokes layer thickness) is given by (Marcos *et al.*, 2004a)

$$\delta_s = \sqrt{\frac{\nu}{\omega}} \tag{6.23}$$

It can be observed that under very a large ω, the penetration depth is small, and the fluid in the channel cannot reach the full oscillation. Hence the penetration depth should be lager or in the same order of magnitude as the channel width, *i.e.*, $\delta_s \geq W$, and the estimation of the upper limit of the angular frequency is

$$\omega_{\text{upper}} \leq \frac{\nu}{W^2} \tag{6.24}$$

Rewriting the Eq. (6.23), one can obtain $\frac{\omega_{\text{upper}} W}{U} \leq \frac{\nu}{WU}$, which in fact can be rewritten as

$$\text{St} \leq \frac{1}{\text{Re}} \tag{6.25}$$

Therefore one can obtain an estimation for the effective frequency range

$$1 \leq \text{St} \leq \frac{1}{\text{Re}} \tag{6.26}$$

In most microfluidic systems, Re < 1, so Eq. (6.26) also can give a reasonable range of the Strouhal number (St). With the experimental conditions of $U = 1$ mm/s and $W = 300$ μm, one can obtain $1 \leq \text{St} \leq 3$, from which the effective range of the frequency of applied electric field is found to be between 0.5 and 2 Hz. Eq. (6.26) only provides an order of magnitude estimation. In fact, the actual frequency can be either lower or higher, because the optimum frequency is also related to other factors, such as the oscillation amplitude, geometry *etc.* Even so, the estimation from Eq. (6.26) provides a guide for further experimental and simulation studies.

Measurements were carried out using $V_1 = V_2 = 300$ V and various frequencies (0.5, 1 and 5 Hz). Figure 6.14 shows the mixing intensity from both experiment and simulation with the frequency of $f = 1$ Hz. Figure 6.15 presents the mixing efficiencies under different frequencies from both experimental and simulation results.

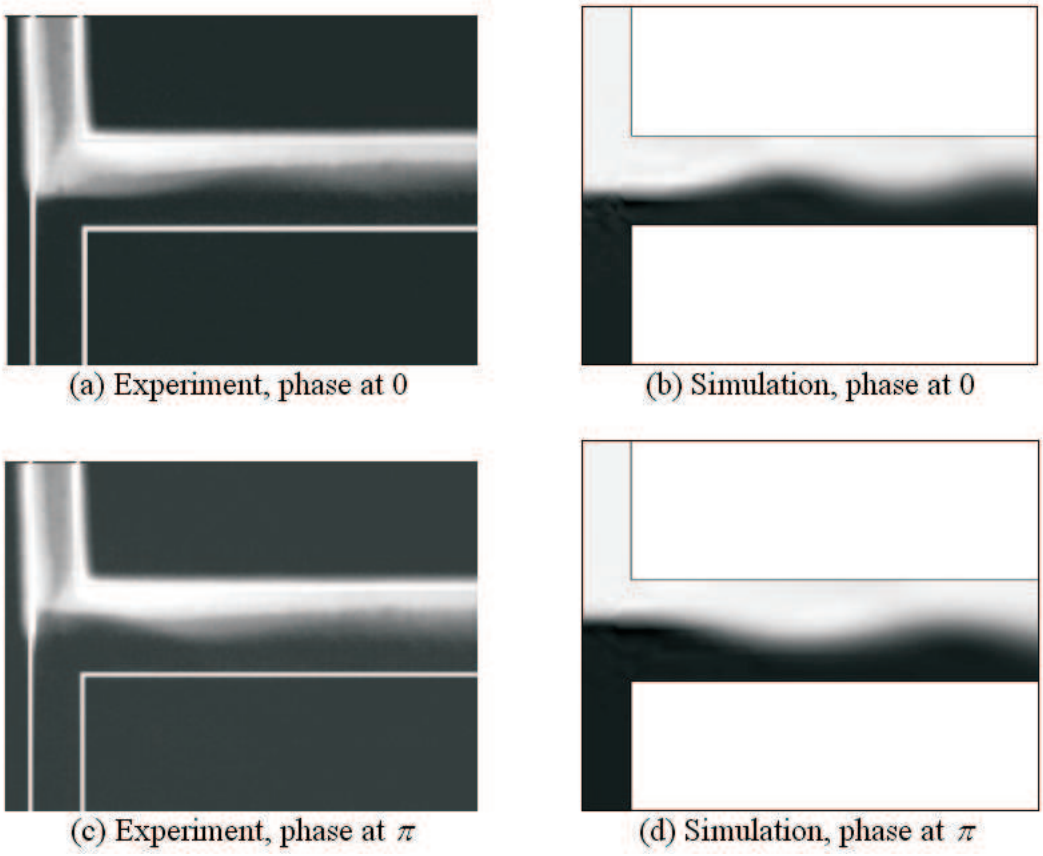

Figure 6.14 Comparisons of the mixing results between experiment and numerical simulations under $f = 1$ Hz and $V_1 = V_2 = 300$ V at different phases (0 and π).

The frequency range was chosen using Eq. (6.26). Under $f = 0.5$ Hz, the mixing in the channel presents a banded structure and the mixing efficiency also oscillates drastically along the channel downstream from T-junction. With $f = 5$ Hz, the mixing presents two parallel streams and there is almost no oscillating effects, resulting in almost the same quality as that under the DC condition. From Figure 6.15, it can be observed that among all the frequencies used, $f = 1$ Hz yields the highest mixing efficiency.

6.4.1.3 Velocity field in electrokinetic T-mixer

Using the micro-PIV technique, we measured the velocity field in the channel of T design at different phases. Figure 6.16 shows the experimental and simulation results of the flow fields in a T-mixer. It can be noted that the flow field exhibits a plug-like shape at different phases throughout the channel, except for the joint region. Due to the plug-like velocity profile, the mixing process in the channel is not subject to any

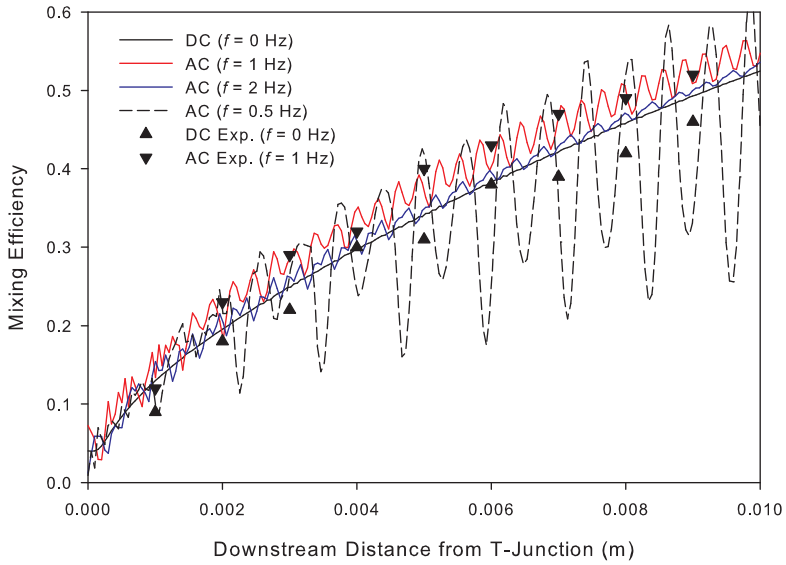

Figure 6.15 Mixing efficiency under different frequencies ($V_1 = V_2 = 300$ V). The lines represent the simulation results and the symbols denote the experimental data.

Taylor dispersion, and thus it mainly depends on molecular diffusion (Ghosal, 2006). Therefore, even if we employ certain oscillating electrokinetic flow to increase the contact interface area between two fluids, the improvement of mixing is still limited, as shown Figure 6.15.

6.4.2 Effect of channel geometry and AC electric field on the mixing efficiency

In order to improve mixing quality, one can consider some geometry inhomogeneity in the channel that may cause the EOF to deviate from the ideal plug flow profile, resulting in the presence of Taylor dispersion. One viable approach is to introduce turns and patterns in the microchannel so that the flow pattern can deviate from plug-like flow. In the present study, we design two types of T-mixers with patterned blocks, including T1 and T2 designs. T1 contains a series of converging-diverging sections; whereas T2 contains a serpentine structure. In addition, based on the design of patterned blocks, we apply AC electric field to introduce the oscillating flow and investigate the effect on mixing efficiency.

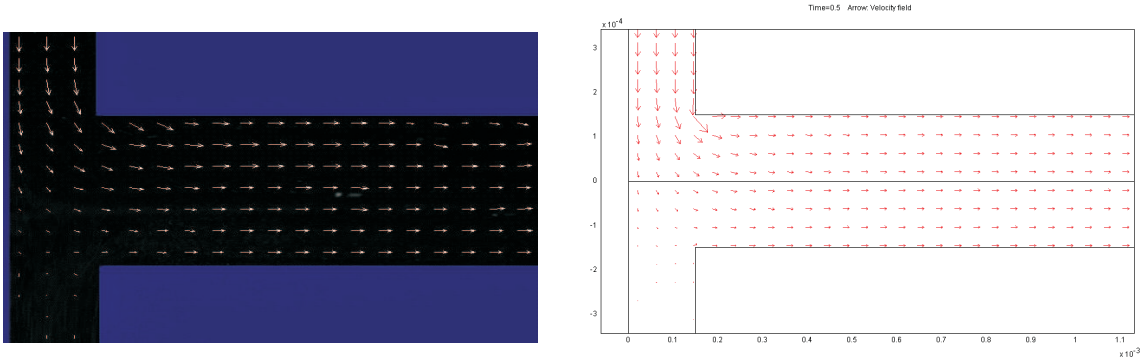

(a) Velocity distribution at phase π /2

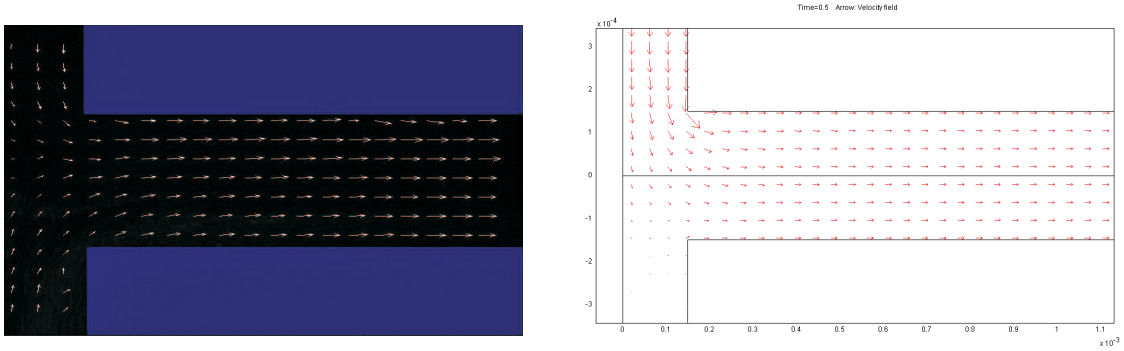

(b) Velocity distribution at phase π

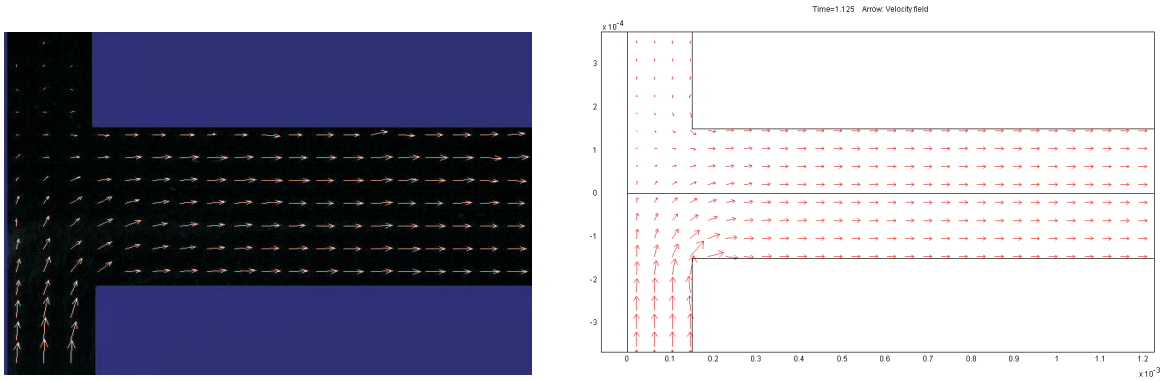

(c) Velocity distribution at phase 3π /2

Figure 6.16 EOF velocity distributions in a T-shaped channel at different phases, left: experiment; right: simulation ($V_1 = V_2 = 150$ V).

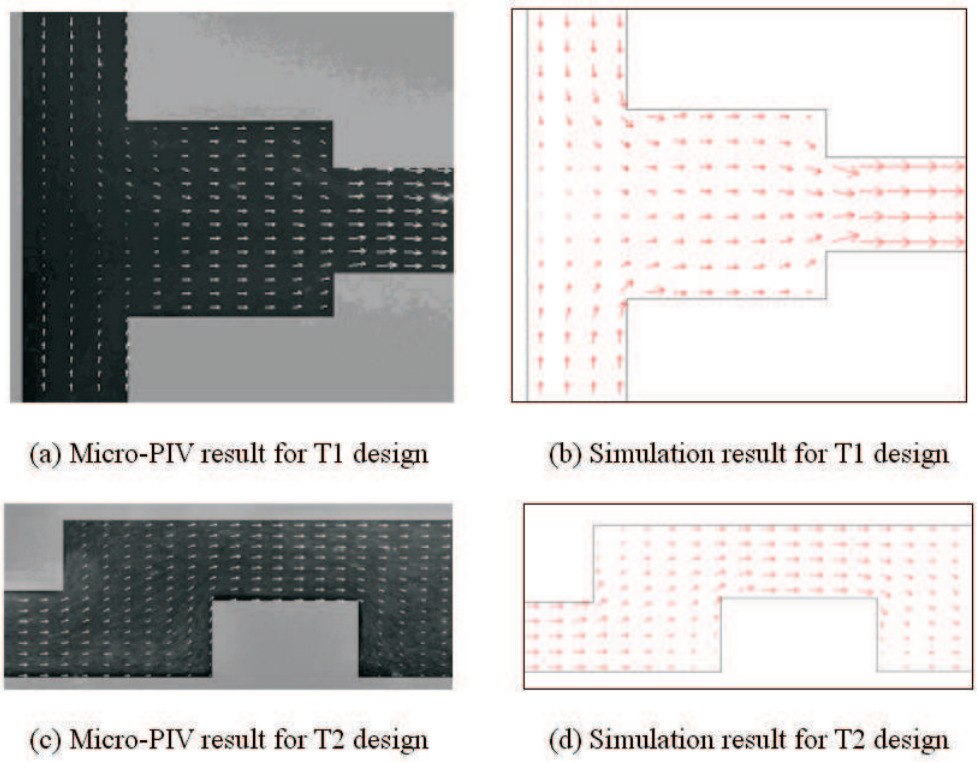

Figure 6.17 Micro-PIV measurement and simulation results of the flow fields for T1 and T2 designs ($V_1 = V_2 = 150$ V).

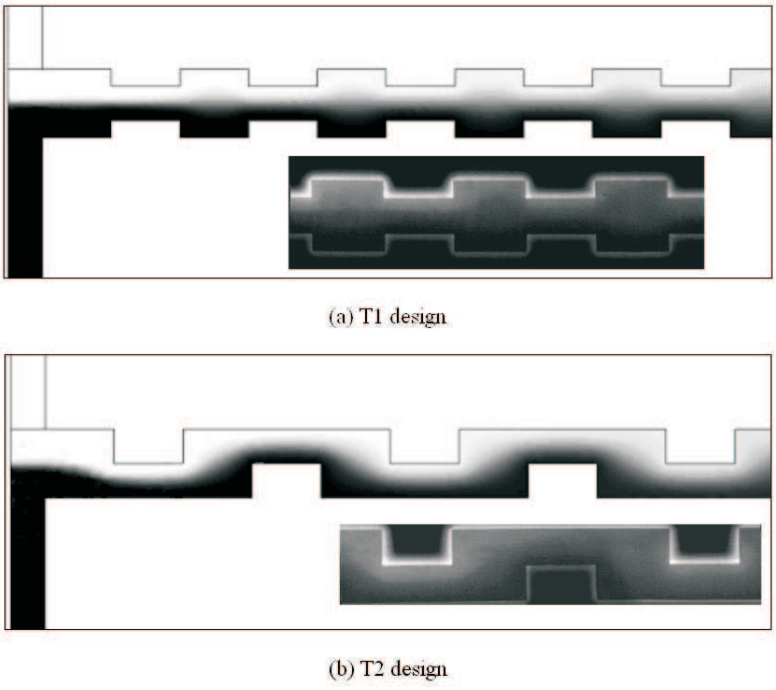

Figure 6.18 Comparison of the results of experimental and simulation mixing quality ($V_1 = V_2 = 150$ V). Long channel: simulation; Short channel: experiment.

Under DC condition, from the micro-PIV measurements and simulation results as shown in Figure 6.17, it can be seen that in the turns of the T2 design, there are non-plug flow pattern, and in the T1 design, near the diverging-converging part the velocity field also present non-plug profile. In the literature (Ghosal, 2006), the deviation of the sample blob in the channel curvature under electrokinetic effect is called "race track" effect. In electrochromatography and separation applications, this effect should be avoided, but in the micromixing applications, it offers an option to make use of the Taylor dispersion effect for improving micromixing. Hence, the non-plug flow pattern induces the "race track" effect and results in Taylor dispersion. Yariv *et al.* (2004) theoretically investigated the curvature-induced dispersion in electroosmotic serpentine flows. They found that with the channel curvature decreased, the effect of solute dispersion increases. Figure 6.18 shows the mixing effects (gray intensity) from both experiments and simulations in different designs. A comparison of the experiments and the simulations shows reasonable agreement.

Figure 6.19 shows the EOF velocity distributions at different phases in the T2-design channel, both from micro-PIV measurements and simulation results. The comparison of these results shows reasonable agreement. It also can be observed that the velocity field distribution near the T-junction is oscillating in a periodical manner. As a result, the fluid oscillation near the T-junction makes the contact area between the two streams increase, which will improve mixing. With more contact area, the two streams will mix further when flowing through the patterned channel.

Figure 6.20 presents the mixing efficiency under different conditions for T1 and T2 designs. It can be observed that the mixing is improved using the patterned channel under DC condition, and under AC electric field, the mixing is improved further. It is also observed that the mixing efficiency in T2 design is better than that in T1 design under both DC and AC conditions. The reason can be explained as follows: the turns in the T2 design induces stronger transverse flow (Figure 6.17 and Figure 6.19); however, only very limited non-plug flow happens near the diverge-converge region in the T1-design channel (Figure 6.17). Hence in the T2 design, there exists a stronger

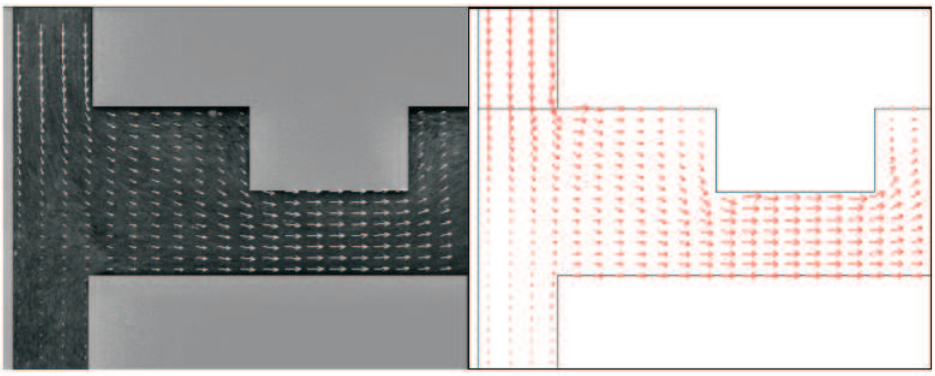

(a) Velocity distribution at phase $\pi/2$

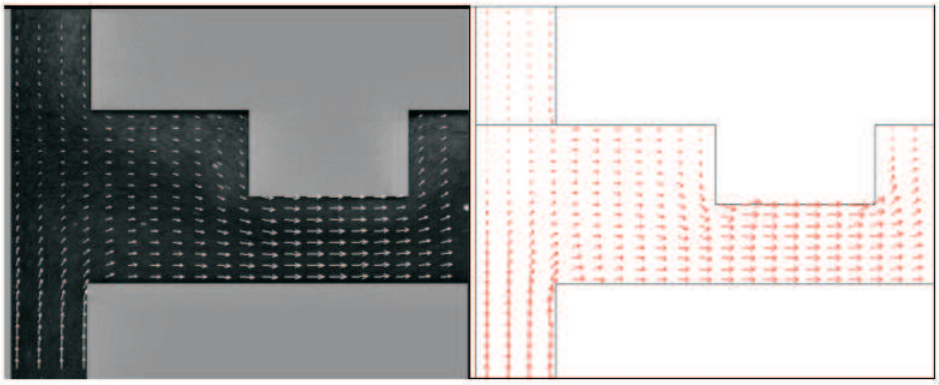

(b) Velocity distribution at phase $3\pi/2$

Figure 6.19 EOF velocity distributions in T2 designed channel at different phases, left: experiment; right: simulation ($V_1 = V_2 = 150$ V).

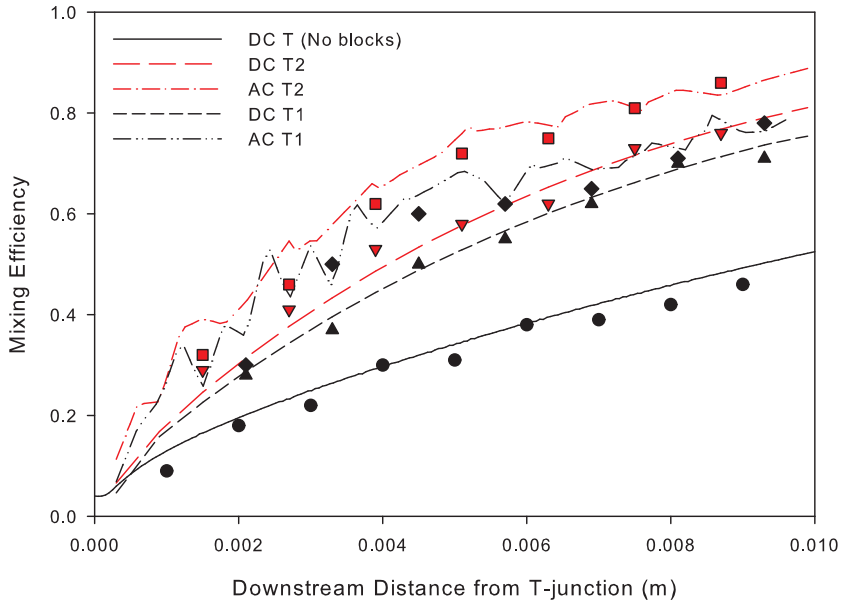

Figure 6.20 Mixing efficiency for the T, T1 and T2 designs (V_1 = 300 V, and V_2 = 300 V for AC conditions under f = 1 Hz). The lines represent the simulation results and the symbols denote the experimental data (circle: T design, up triangle: T1 design, down triangle: T2 design, square: T2 design, diamond: T1 design).

Taylor dispersion effect than that in the T1 design, and thus has a better mixing effect.

6.5 A Novel Design for Electrokinetic T-mixer Using Fabricated Electrodes

From the aforementioned experimental and numerical studies, it can be noted that using the AC driven flow oscillation cannot significantly enhance electrokinetic mixing. The reason is that even with the oscillating flow, the velocity profile is still plug-like in most regions of the T-mixer except for the T-junction, which neither induces transverse flow nor the Taylor dispersion effect. Hence if high mixing quality is demanded, one needs to utilize an AC electric field to induce transverse flow. In this section, a novel design is proposed for electrokinetic T-mixer using AC electric field generated by fabricated electrodes inside the channel. Due to time limit, only numerical simulations are carried out to demonstrate this design.

6.5.1 Background and description of the new design

Numerous studies have been conducted in EK mixing using surface heterogeneity (Erickson and Li, 2002, Qian and Bau, 2002, and Biddiss *et al.*, 2004). These methods use surface charge patterning, which results in different zeta potentials, and thus alters the local electroosmotic flow field to improve the mixing quality. These approaches are effective to some extent. However, there are some disadvantages, such as the patterning process is usually long and complicated; the patterned surfaces are sensitive to contaminants and may not work functionally if contaminated. In addition, after the patterning, these surfaces are out of control, and hence the mixing is totally "passive".

One viable way to overcome those disadvantages is to use fabricated electrodes with adjustable electrical potentials. Since electrode surface is conductive and can be controlled by applied electric potential, both the local electric field and flow field can be manipulated. By further adjusting the frequency and amplitude, one can make the EK mixer perform in an optimum condition.

The new design scheme is as follows. As shown in Figure 6.21 (not to scale), using the T design, we add a pair of two metal surfaces as electrodes fabricated on the channel near downstream of the T-junction. Then we connect these metal surfaces with an AC electric field (low frequency of several Hz, and low voltage of less than 10 V). The purpose is to induce transverse flow near the metal surface and hence improve mixing quality. Next, the design will be validated using numerical simulation.

6.5.2 Numerical simulation and discussion

In numerical simulation, we still use the same parameters as those used in Section 6.4.1, where $V_1 = V_2 = 150$ V. We use one pair or two pairs of metal surfaces, which are fabricated on the side walls of 0.5 mm and 1 mm downstream from the T-junction. When using two pairs, the AC electric field applied on each pair is assumed to have opposite phase angles. The metal surface is 10 μm long and its thickness is negligible. The AC electric field has the amplitude of 10 V and various frequencies.

For the choice of boundary conditions, special attentions should be paid to the

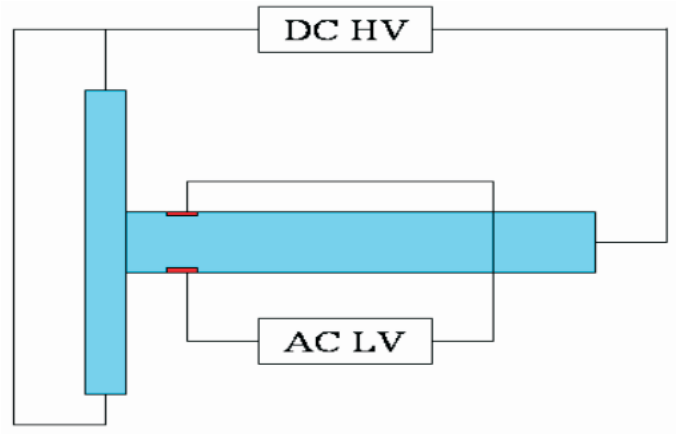

Figure 6.21 Sketch of the EK mixer design. HV is high voltage power supply and LV is low voltage power supply.

metal surface. It is known that the electrical potential on the surface is altered when an electric field is imposed. As the metal is in contact with electrolyte solution, the charged surface will interact with ions in the electrolyte, giving rise to re-distribution of the ions near the metal surface. Thus, and electric double layer (EDL) will be formed. Under low frequency of the external electric field (less than 10 Hz), the Gouy-Chapman model is still valid (Gunning *et al.*, 1995). The EDL near the metal surface is different from that near the dielectric channel surface, and the zeta potential is unknown. However, since metal surface is highly conducting, the surface can be treated to be isoelectric, and thus the local electric field vector is perpendicular to the surface. As a result, there is no electric field component along the surface, and there is no-slip velocity either. We therefore apply the no slip velocity boundary condition to the metal surfaces. In fact, based on the numerical simulation results shown below, if the length of the metal surface is short enough, its size has negligible effect on the flow field. In other words, the mixing effect is found not sensitive to the metal surface size if it is small.

Numerical simulations were carried to study the solute concentration distributions in an electrokinetic T-mixer for: 1) without any metal surfaces; 2) with one pair of metal surfaces; and 3) with two pairs of metal surfaces. In the simulation, the electric field frequency was chosen as $f = 1$ Hz. Figure 6.22 shows a comparison of the

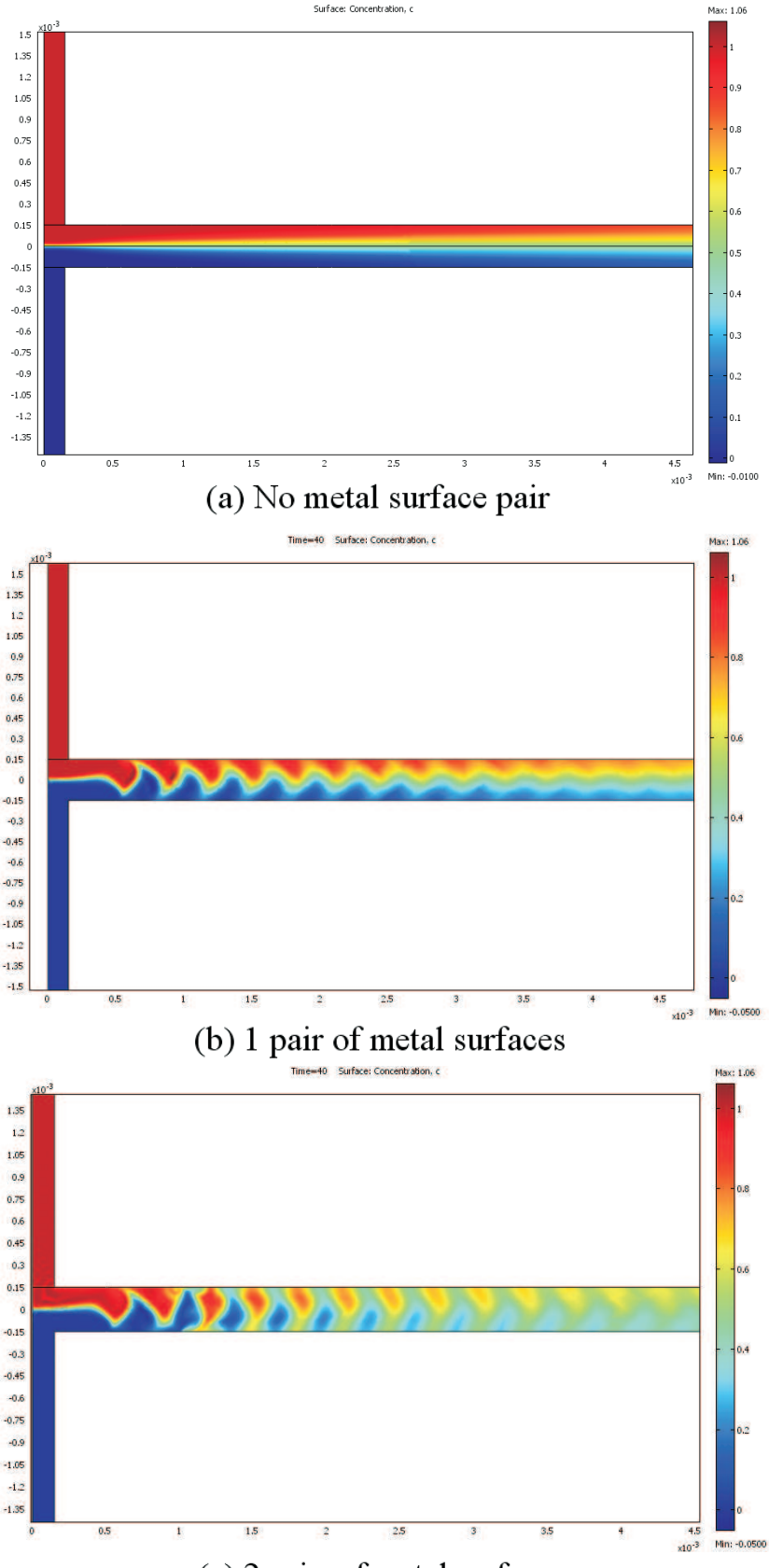

Figure 6.22 Simulation results of solute concentration distributions in electrokinetic T-mixer, (a) without metal surface, (b) with 1 pair of metal surfaces ($f = 1$ Hz), and (c) with 2 pairs of metal surfaces ($f = 1$ Hz).

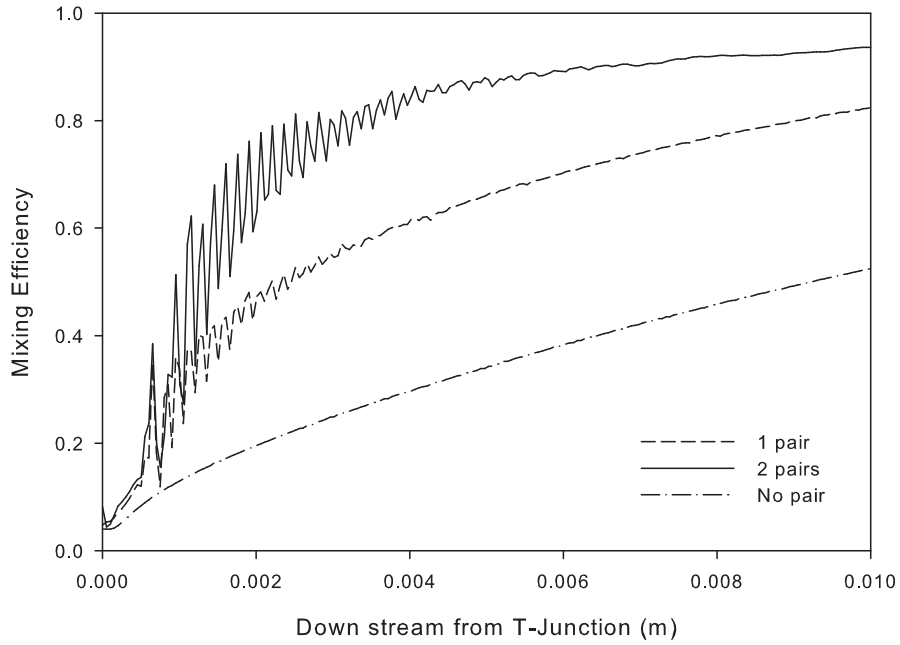

Figure 6.23 Comparisons of the mixing efficiency under three different conditions (No pair, 1 pair, and 2 pairs of metal surfaces).

concentration distributions under the 3 conditions mentioned above. It can be observed that with metal surfaces, the mixing quality has been improved significantly. The results displayed in Figure 6.23 show that the mixing efficiency is increased drastically with the metal surfaces effect. Figure 6.24 shows the electric potential distributions at four different phases. It can be noted that the electric potential distribution only changes in the region near the metal surfaces. Due to a change of the local electric field, the mixer also has an advantage that the flow field also keeps plug-like flow in most other parts of the channel, except for the small regions near the metal surfaces. This scenario is shown in Figure 6.25, from which we can observe that flow field keeps unchanged except for the small region near the metal surfaces. This advantage is useful, since in certain conditions a steady flow rate is required.

6.5.3 Suggestions on fabrication and operation

Due to the small size of the metal surfaces embedded at the channel walls, special micro fabrication technology is needed. One option is the silicon bulk micromachining

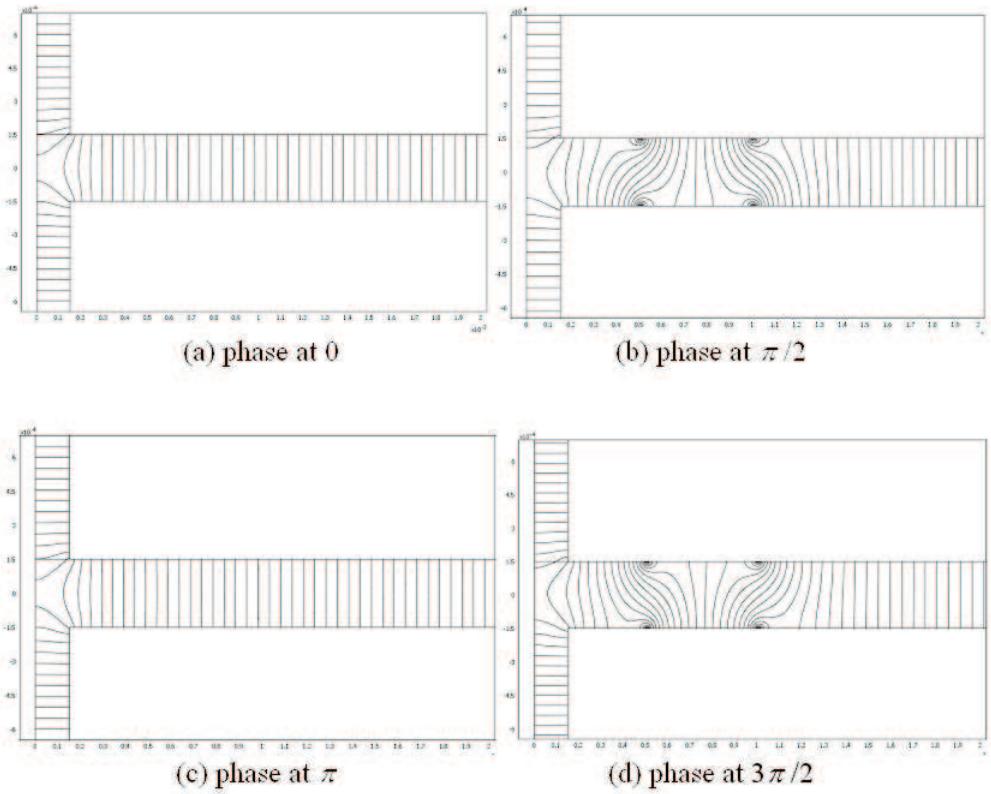

Figure 6.24 Electric potential distributions at different phases (2 pairs of metal surfaces).

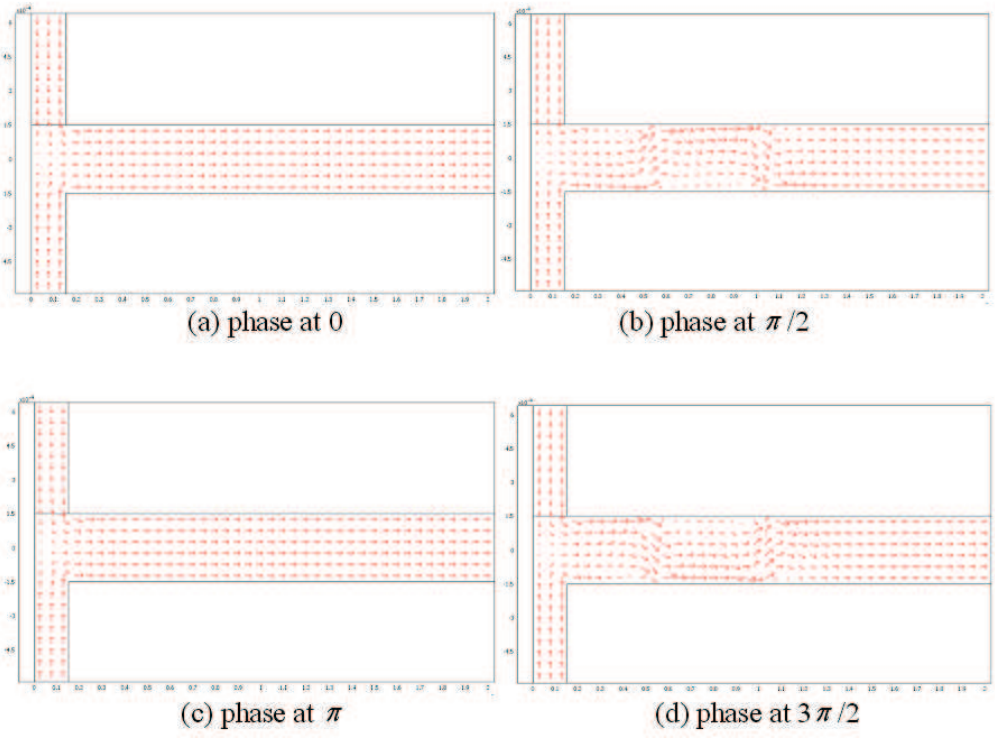

Figure 6.25 Velocity field at different phases (2 pairs of metal surfaces).

technology (Chen *et al.*, 2003; Zhang *et al.*, 2003). Using this technology, one can integrate the metal surfaces to the full depth of the channel. To avoid the electrolysis of water, platinum should be used as the material of the metal surfaces. Meanwhile, to avoid bubble generation around the metal surfaces, the AC voltage amplitude should not exceed 20 V and the buffer solution should have the lower concentration possible.

6.6 Summary

Mixing is a complicated phenomenon which involves physical processes including momentum and mass transfer. The mixing quality in an electrokinetic T-mixer is controlled by several factors, including the electric field frequency, the field amplitude, and the size or geometry of the channel. In the present study, these factors are systematically investigated using both numerical and experimental methods. It is found that under DC condition, the mixing quality in a traditional electrokinetic T-mixer is poor.

For enhancing the mixing efficiency, both active and passive schemes are proposed. The AC field driven flow provides an active way for improving mixing quality, whereas the patterned blocks in the channel offers a passive mechanism to introduce the "race track" effect to increase the Taylor dispersion, which is effective for improving micromixing. Because EOF in microfluidic channels exhibits a plug-like profile which is different from classical pressure-driven flows, the mass transport of solutes is not subjected to any Taylor dispersion in the bulk flow region. From the experimental results and simulation data, it is concluded that the electroosmotic oscillation in T-mixer has limited improvement in mixing quality. However, the electroosmotic oscillation in a channel with patterned blocks can enhance the mixing efficiency further.

In addition, a novel design is proposed for electrokinetic micromixer, which utilizes the metal surface effects to induce the transverse flow in microchannels. Using numerical simulation, the new design is validated. It is also concluded that the novel design guarantees high mixing efficiency and steady electroosmotic pumping.

Chapter 7

Conclusion and Future Studies

7.1 Contributions of This Study

Following the objectives of the present work, extensive and rigorous studies on the time-dependent and frequency-dependent electroosmotic flows in microchannels have been conducted using either the analytical or numerical approaches under various physicochemical conditions. Experiments for characterizing and verifying the theoretical models of the time-dependent and frequency-dependent EOF in microchannels have been carried out. Based on the extensive experimental data and simulation results, reasonable agreements have been obtained. An in-depth understanding of the time-dependent and frequency-dependent electroosmotic flows in microchannels has been achieved. As an important application, the electrokinetic micromixing has been systematically investigated. The experimental approaches used in the present work not only provides first-hand information or/and direct observations which form a basis for development of new theories, but also can generate an amount of data which allow for validation of existing models. Nonetheless, the major contributions made during the course of this study can be summarized as follows:

1. A method for simultaneously determining zeta potentials of both channel surfaces and tracer particles. Using the micro-PIV technique, we have characterized the steady-state EOF in open- and closed-end rectangular microchannels.

The typical plug-like flow pattern in open-end channel and parabolic velocity profile in closed-end channel have been demonstrated. A method is developed to simultaneously determine the zeta potentials of the channel surface and the tracer particles in aqueous solutions. The new method uses the micro-PIV technique to measure the steady velocity distributions of tracer particles in both open- and closed-end microchannels under the same water chemistry condition. As a result, the zeta potentials of the tracer particles and the channel surfaces can be determined using the least-square method to fit the micro-PIV measured velocity distributions of the tracer particles. Nonetheless, the new method avoids dealing with the problems associated with the stationary level in microelectrophoretic measurements, and allows for simultaneously determining the zeta potentials of the tracer particles and the microchannel surfaces using the micro-PIV technique.

2. Diagnosis of start-up transient electroosmotic flows in microchannels. A phase locking based micro-PIV technique has been developed to investigate the transient electroosmotic flow fields by using precise synchronization of different trigger signals for the laser, CCD camera, and in-house designed high-voltage switch. Experiments were conducted to measure the time evolution of electrokinetic flows in both open-end and closed-end rectangular microchannels. Utilizing such transient micro-PIV technique, a method has been proposed to determine the electrophoretic mobility of the tracer particles and the zeta potential of the channel wall. The method reported here allows for measuring the channel wall's zeta potential without dealing with the difficulty related to the so-called stationary level and is suitable for the situations where the Joule heating associated problems are severe. Using the measured channel zeta potential, the theoretical predictions of the transient electroosmotic velocity fields are validated with the experimental data. To our best knowledge, this study reports the first measurement of transient electroosmotic flow fields and the first experimental verification of analytical predictions of the temporal development of electroosmotic flows. The transient micro-PIV technique presented in this study can be a useful tool to study the dynamic characteristics of the electroosmotic velocity

field in microfluidic devices.

3. Characterization of the time-dependent electroosmotic flow in microchannels with finite reservoir size effect. With an order of magnitude analysis on a typical microfluidic system, an analytical model has been presented to describe the effect of the finite reservoir size on electroosmotic flow in a rectangular microchannel. Two important time parameters were introduced, including the effective pumping period and the reverse flow starting time to characterize the electroosmotic pumping, and both the effective pumping period and the reverse flow starting time can be determined using the analytical model developed in this study. Several parameters were studied to analyze the reservoir size effects on the EOF effective pumping, including the dimension of the reservoir's cross section, the length of the microchannel, and the cross-sectional area of the microchannel. It was found that the reservoir effect is stronger for smaller reservoir size, shorter channel length, and larger channel cross-sectional area.

4. Characterization of frequency-dependent electroosmotic flow in the microchannels. A method that combines the Laplace transform and Frequency Domain Analysis has been developed to analyze the EOFs in both open- and closed-end rectangular microchannels. This method provides insight into the underlying physics of the frequency-dependent EOF. Further, using the micro-PIV technique, frequency-dependent electroosmotic flows in microchannels were measured. It is observed that the combined DC/AC field driven EOF in microchannels presents a flow pattern consisting of a constant velocity component and an oscillating component. Since the constant velocity part can be used for fluid pumping and the oscillating part can be used for convective mixing, this flow pattern may have potential microfluidic mixing applications.

5. Study of the electrokinetic micromixing using frequency-dependent electroosmotic flow and patterned blocks in the microchannels. Numerical and experimental investigation has been carried out on the characterization and performance of an electrokinetic T-mixer. Several factors including the electric field

frequency, the electric field amplitude, and the size or shape of channels have been examined thoroughly to assess their effects on the mixing efficiency of the electrokinetic T-mixer. The electric oscillation gives an active way for improving mixing quality, whereas the patterned blocks in the channel offers a passive mechanism to induce the "race track" effect to increase the Taylor dispersion for micromixing enhancement. Based on the experimental data and simulation results, it is found that the electric oscillation has limited improvement in mixing quality, while the patterned designs can enhance the mixing effectively. In addition, a novel design for electrokinetic micromixer is proposed, which utilizes the fabricated electrodes to induce the transverse flow in the channel. Numerical simulation shows that the novel design provides a high mixing efficiency while guarantees steady electroosmotic pumping.

7.2 Recommendations for Future Studies

Based on the results presented in this study, some comments and recommendations are made as following for future research.

1. Measurements of the pressure gradients in the closed-end microchannels for micro actuation. Study of the time-dependent or frequency-dependent electrokinetic flows in closed-end channels is of special interest, since the flow velocity field is resulted from a combination of the electroosmosis and the induced backpressure gradient. From a practical viewpoint, a promising application of using the closed-end channel structure has been proposed for the development of electrokinetic microactuators (Marcos *et al.*, 2004b). However, in the present study, we only managed to measure the EOF velocity fields in closed-end microchannels using the micro-PIV technique. In the literature, Reppert and Morgan (2002) measured the pressure in a pseudo-closed system, where one end of the capillary was closed and the other end was attached to an infinite reservoir. However, these efforts are not enough to explore the micro actuation applications. Therefore, extensive data of the pressure measurements are needed for characterization of the micro actuation.

2. Experimental characterization of the electrokinetic micromixer using fabricated electrodes. In Chapter 6, a novel electrokinetic micromixer with aid of the fabricated electrodes is proposed. The numerical simulations show that the new design improves the mixing quality effectively. Hence, further experimental studies are suggested to include the fabrication and the experimental characterization of such electrokinetic micromixer. Due to the small size of the metal electrodes embedded on the channel walls, a suitable micro fabrication technology is needed. One option is the use of the silicon bulk micromachining technology, based on which, one can integrate the metal electrodes into the full depth of the channel. To avoid the electrolysis of water, platinum is suggested to be the material of the electrodes.

3. Systematic investigation of the biofluids and bioparticles under time- and frequency-dependent electric field. In the present study, we only used the dilute electrolytes and DI water as the working microfluidics. However, in various chemical analysis and biomedical diagnosis the test samples involve biofluids and bioparticles such as cells. On the one hand, biofluids may not behave as Newtonian liquids; on the other hand, electrokinetic properties of biofluids with bioparticles (*e.g.*, dielectric constant, electrical conductivity, zeta potential, *etc.*) are different from dilute electrolytes. Therefore, modeling and experimental investigation of such biofluid flow driven by time- and frequency-dependent electric field not only are of fundamental interest, but also are of importance to the design and optimum control of microfluidic devices.

Appendix A

Effect of Finite Reservoir Size on Electroosmotic Flow in Cylindrical Microchannels

In Chapter 4, we have discussed the effect of finite reservoir size on EOF in rectangular microchannels. However, the cylindrical microchannels are also widely used in various applications, such as the capillary electrophoresis. In the following, the effect of finite reservoir size on EOF in cylindrical microchannels will be analyzed.

A.1 Mathematical Model

Similar to the derivation in Chapter 4, we make the same assumptions and also use the slip velocity approximation. We can write the expression for the flow field in dimensional form as

$$u\left(r,t\right)=u_{\mathrm{eo}}+u_{\mathrm{p}}\left(r,t\right) \tag{A.1}$$

In Eq. (A.1), the electroosmotic flow field u_{eo} is steady, while the backpressure driven flow field $u_{\mathrm{p}}(r,t)$ is time-dependent because of the change of liquid level in the reservoirs with time. The EOF can be considered as a flow induced by a moving wall with a

velocity (slip velocity) given by Smoluchowski equation,

$$u_{\mathrm{eo}} = -\frac{\varepsilon_0 \varepsilon_{\mathrm{r}} \zeta E}{\mu} \tag{A.2}$$

Using the cylindrical coordinates system shown on the cylindrical channel, with assumption of the pseudosteady pressure-driven flow, the flow velocity profile is described by the well-known Poiseuille flow which in a cylindrical channel is expressed as (Papanastasiou *et al.*, 2000)

$$u_{\mathrm{p}}(r,t) = \frac{1}{4\mu}\frac{\Delta p(t)}{l}\left(a^2 - r^2\right) \tag{A.3}$$

where $\Delta p(t)$ is the time-dependent pressure drop induced by change of the liquid levels in the reservoirs, and a is the radius of the cylindrical channel. In order to compute the velocity profile expressed in Eq. (A.3), we will determine the induced backpressure $\Delta p(t)$ in the following section.

A.2 Determination of the Induced Backpressure Gradient

Similarly, the total flow rate in the channel also consists of two parts, the electroosmotic flow rate and the backpressure driven flow rate. Then according to Eq. (A.1), the total flow rate can be expressed as

$$q(t) = q_0 - q_{\mathrm{p}}(t) \tag{A.4}$$

where "−" sign indicates that the induced backpressure driven flow is always in opposite to the electroosmotic flow. q_0 is the electroosmotic flow rate and is expressed as

$$q_0 = u_{\mathrm{eo}} A_{\mathrm{cross}} = -\frac{\varepsilon_0 \varepsilon_{\mathrm{r}} \zeta E}{\mu}\pi a^2 \tag{A.5}$$

Integrating Eq. (A.3) over the cross-sectional area of the rectangular microchannel gives an expression for the volumetric flow rate in the induced pressure driven flow as

$$q_{\mathrm{p}}(t) = \frac{\pi a^4}{8\mu}\frac{\Delta p(t)}{l} \tag{A.6}$$

For two identical reservoirs, the radii are R, and the cross section area is $A = \pi R^2$. Thus, the induced backpressure drop resulted from the change of fluid levels in the two reservoirs can be related to the total quantity of liquid transported during the pumping period from time zero to time t, and the correlation then can be expressed as

$$\Delta p(t) = \rho g \frac{2Q(t)}{A} \tag{A.7}$$

where $Q(t)$ is the total quantity of liquid transported at given time t and can also be expressed as

$$Q(t) = \int_{\tau=0}^{t} q(\tau)\mathrm{d}\tau \tag{A.8}$$

Substituting Eq. (A.7) into Eq. (A.6), we can obtain

$$q_{\mathrm{p}}(t) = \frac{\pi \rho g a^4}{4\mu A l} Q(t) \tag{A.9}$$

Introducing a parameter,

$$C = \frac{\pi \rho g a^4}{4\mu A l} \tag{A.10}$$

we can write

$$q_{\mathrm{p}}(t) = CQ(t) \tag{A.11}$$

Using Eqs. (A.4), (A.8) and (A.11), we can show the expression for the total flow rate

$$q(t) = q_0 - C\int_{\tau=0}^{t} q(\tau)\mathrm{d}\tau \tag{A.12}$$

Eq. (A.12) is an integral equation. With the initial condition of $q(t=0) = q_0$, we can

solve it to obtain the time-dependent flow rate,

$$q(t) = q_0 \exp(-Ct) \tag{A.13}$$

Substituting Eq. (A.13) into Eq. (A.8) yields an expression for the total quantity of liquid transported during the period of time zero to time t:

$$Q(t) = \frac{q_0}{C}\left[1 - \exp(-Ct)\right] \tag{A.14}$$

Putting Eq. (A.14) into Eq. (A.7), we can show that the induced backpressure gradient along the channel can be expressed as

$$\frac{\Delta p(t)}{l} = \frac{2\rho g q_0}{CAl}\left[1 - \exp(-Ct)\right] \tag{A.15}$$

A.3 Two Important Time Parameters for Electroosmotic Pumping in a Cylindrical Tube

A.3.1 Effective pumping period

With the backpressure gradient obtained, by substituting Eqs. (A.3), (A.10) and (A.15) to Eq. (A.1), we obtain the velocity distribution in the capillary as

$$u(r,t) = u_{\text{eo}} - 2u_{\text{eo}}\left(1 - \frac{r^2}{a^2}\right)\left[1 - \exp(-Ct)\right] \tag{A.16}$$

It can be observed that the solution is one dimensional (only relevant to r and t) and more concise than that for rectangular channel.

For the estimation of effective pumping period, we can see the expression Eq. (A.13) for the flow rate has the same form of that for rectangular channel, except for the different value of the constant C. Hence, similar to the definition used in Chapter 4, if we still define the effective pumping period is the time to which the volumetric flow

rate reaches 95% of q_0, then the effective pumping period is

$$t_{\text{eff}} = -\frac{\log(0.95)}{C} \approx \frac{0.05}{C} \tag{A.17}$$

A.3.2 Reverse flow starting time

In order to compute the time when the reverse flow starts, we only need to solve

$$|u(r=0,t)| = |u_{\text{eo}}| \tag{A.18}$$

Substituting Eq. (A.18) to Eq. (A.16), readily we obtain

$$t_{\text{rev}} = \frac{\log 2}{C} \tag{A.19}$$

If we substitute Eq. (A.19) to Eq. (A.13), we can find at this time the volumetric flow rate is one half of the electroosmotic flow rate q_0.

In conclusion, we have presented an analysis of finite reservoir size effect on the EOF in cylindrical microchannels. For those applications using cylindrical tubes, these results can be used in microfluidic system design and optimization.

Appendix B

Frequency Domain Analysis Method

The transfer functions play an important role in describing and analyzing dynamic systems. In particular, we have the following relationships as shown in Figure B.1 and Eq. (B.1) (Ronald and Duncan, 2004):

$$Y(s) = G(s)\,U(s) \tag{B.1}$$

$$y(t) = \int_{\tau=0}^{t} g(t-\tau)u(\tau)\mathrm{d}\tau \tag{B.2}$$

$$g(t) = \mathcal{L}^{-1}[G(s)] \tag{B.3}$$

If the transfer function $G(s)$ is known, one first determines the impulse response which is expressed in Eq. (B.1). Then, for any input function, the desired response can be obtained via the convolution integral given in Eq. (B.2). Alternatively, one could di-

Figure B.1 An overall system with single input and single output.

rectly determine the inverse transform of Eq. (B.3) using the partial fraction expansion or the theory of residues.

An important input function is the sinusoid. The output response of a LTI (linear time-invariant) system resulting from a sinusoidal variation in a selected system input is termed as the frequency response of the system. As shown below, the output response is also a sinusoid of different magnitude, and it is shifted by a phase angle, ψ, relative to the input function. Thus, we have

$$u(t) = b\sin(\omega t) \tag{B.4}$$

The output of a system described by transfer function, $G(s)$ can be written as

$$y(t) = b\left|G(\mathrm{j}\omega)\right|\sin(\omega t + \psi) \tag{B.5}$$

where $\mathrm{j} = \sqrt{-1}$. To justify this statement, consider a SISO (single input and single output) system where the input is a simple sinusoid. For this case, the Laplace transform of the input function is given by

$$U(s) = \frac{b\omega}{s^2 + \omega^2} \tag{B.6}$$

and the Laplace transform of the output is the product of $G(s)$ and $U(s)$, or

$$Y(s) = G(s)\frac{b\omega}{s^2 + \omega^2} \tag{B.7}$$

Since $G(s)$ can be written as $Z(s)/P(s)$ which has n system poles (*i.e.*, the n roots of $P(s) = 0$), we can use the method of residues to determine the output response, or

$$y(t) = \mathcal{L}^{-1}[Y(s)] = \sum_{\text{all poles}} \text{residues of } \left[G(s)\frac{b\omega}{(s - \mathrm{j}\omega)(s + \mathrm{j}\omega)}\mathrm{e}^{st}\right]$$

$$= \left.\frac{G(s)\,b\omega\mathrm{e}^{st}}{s + \mathrm{j}\omega}\right|_{s=\mathrm{j}\omega} + \left.\frac{G(s)\,b\omega\mathrm{e}^{st}}{s - \mathrm{j}\omega}\right|_{s=-\mathrm{j}\omega} + \left.\frac{b\omega G(s)(s - s_1)\,\mathrm{e}^{st}}{s^2 + \omega^2}\right|_{s=s_1}$$

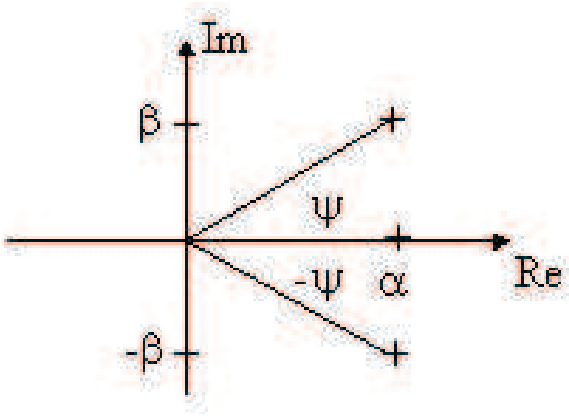

Figure B.2 Complex conjugates in imaginary plane.

$$+\left.\frac{b\omega G(s)(s-s_2)\,\mathrm{e}^{st}}{s^2+\omega^2}\right|_{s=s_2}+\cdots+\left.\frac{b\omega G(s)(s-s_n)\,\mathrm{e}^{st}}{s^2+\omega^2}\right|_{s=s_n} \tag{B.8}$$

where $s_i = s_1,\ s_2,\ s_3,\ \cdots,\ s_n =$ poles of $G(s)$.

For a stable system, all the s_i's have negative real parts. Therefore, after a sufficient time, all the terms containing $\mathrm{e}^{s_i t}$ are vanished and only the first two terms will remain. Therefore, the above expression reduces to

$$\begin{aligned} y(t) &= b\left\{\frac{G(\mathrm{j}\omega)\,\omega\mathrm{e}^{\mathrm{j}\omega t}}{2\mathrm{j}\omega}-\frac{G(-\mathrm{j}\omega)\,\omega\mathrm{e}^{-\mathrm{j}\omega t}}{2\mathrm{j}\omega}\right\} \\ &= b\left\{\frac{G(\mathrm{j}\omega)\,\mathrm{e}^{\mathrm{j}\omega t}-G(-\mathrm{j}\omega)\,\mathrm{e}^{-\mathrm{j}\omega t}}{2\mathrm{j}}\right\} \end{aligned} \tag{B.9}$$

Note that $G(\mathrm{j}\omega)$ and $G(-\mathrm{j}\omega)$ are simply complex numbers. In fact $G(\mathrm{j}\omega)$ and $G(-\mathrm{j}\omega)$ are complex conjugates. Also, note that any complex number can be written in terms of a magnitude and angle. Therefore,

$$G(\mathrm{j}\omega)=\alpha+\mathrm{j}\beta=|G(\mathrm{j}\omega)|\,(\cos\psi+\mathrm{j}\sin\psi)=|G(\mathrm{j}\omega)|\,\mathrm{e}^{\mathrm{j}\psi} \tag{B.10}$$

where $|G(\mathrm{j}\omega)|=\sqrt{\alpha^2+\beta^2}$ and $\psi=\tan^{-1}(\beta/\alpha)$, as shown in Figure B.2. Thus we show that $G(\mathrm{j}\omega)=|G(\mathrm{j}\omega)|\,\mathrm{e}^{\mathrm{j}\psi}$ and $G(-\mathrm{j}\omega)=|G(-\mathrm{j}\omega)|\,\mathrm{e}^{-\mathrm{j}\psi}=|G(\mathrm{j}\omega)|\,\mathrm{e}^{-\mathrm{j}\psi}$. Now we can write $y(t)$ as

$$y(t)=b\,|G(\mathrm{j}\omega)|\left\{\frac{\mathrm{e}^{\mathrm{j}(\omega t+\psi)}-\mathrm{e}^{-\mathrm{j}(\omega t+\psi)}}{2\mathrm{j}}\right\}=b\,|G(\mathrm{j}\omega)|\sin(\omega t+\psi) \tag{B.11}$$

Therefore, the frequency response of a system is in the same form as the input function; the magnitude is multiplied by $G(\mathrm{j}\omega)$ and the sinusoid is shifted by a phase angle ψ. These two quantities, $G(\mathrm{j}\omega)$ and ψ, define completely the response of a stable system to a sinusoidal input. The key point here is that these quantities can be obtained easily from the knowledge of the system transfer function $G(s)$,

$$|G(\mathrm{j}\omega)| = \sqrt{\mathrm{Real}\left[G(\mathrm{j}\omega)\right]^2 + \mathrm{Imag}\left[G(\mathrm{j}\omega)\right]^2} \tag{B.12}$$

$$\psi = \tan^{-1}\left\{\frac{\mathrm{Imag}\left[G(\mathrm{j}\omega)\right]}{\mathrm{Real}\left[G(\mathrm{j}\omega)\right]}\right\} \tag{B.13}$$

An important characteristic of frequency response analysis is that a simple link between the theoretical transfer function and the experimental frequency response exists. Frequency response testing allows one to determine easily the system transfer function. To compute the frequency response, one simply evaluates $G(s)$ and ψ at a large number of frequencies.

Appendix C

Numerical Inversion of Laplace Transform Using the Fixed-Talbot (FT) Method

Numerical inversion of the Laplace transform is very useful in solving the governing equations for many practical problems. Because now researchers have easy access to multi-precision computing software, such as Matlab, by using a simple algorithm one can obtain the numerical inversion with high precision. In this appendix, we provide a brief introduction to the fixed-Talbot (FT) method, which is a simple but very effective algorithm.

The FT algorithm is substantial simplification of the original Talbot procedure which employs deforming the standard contour in the Bromwich inversion integral. For more information, please refer to the work by Abate and Valko (2004). Here we only present the formulations and the program written in Matlab. First, we introduce $\mathrm{j} = \sqrt{-1}$, and define the following:

$$\theta_k = \frac{k\pi}{M} \tag{C.1}$$

$$r = \frac{2M}{5t} \tag{C.2}$$

$$s(\theta) = r\theta(\cot\theta + \mathrm{j}) \tag{C.3}$$

$$\sigma(\theta) = \theta + (\theta\cot\theta - 1)\cot\theta \tag{C.4}$$

In Eqs. (C.1) and (C.2), M is the number of terms to be summed, which should be equal to the number of precision decimal digits to meet the precision requirement.

Using the trapezoidal rule with step size π/M, and $\theta_k = k\pi/M$, one can approximate the value of the numerical inversion of Laplace transform $F(s)$ as below

$$f(t, M) = \frac{r}{M}\left\{\frac{1}{2}\mathrm{e}^{rt}F(r) + \sum_{k=1}^{M-1}\mathrm{Real}\left[\mathrm{e}^{ts(\theta_k)}F(s(\theta_k))(1 + \mathrm{j}\sigma(\theta_k))\right]\right\} \tag{C.5}$$

where $F(s) = \mathcal{L}[f(t)]$. Using Eqs. (C.1) – (C.5), the algorithm can be realized in a short program written in Matlab (attached below), in which the function "F" is the Laplace transform whose numerical inversion is wanted. By adjusting the value of M, one can set the precision of the numerical inversion.

```
function value = inverse_FT(t)
j = sqrt(-1);
M = 32;
digits(M);            % Setting MATLAB precision (32);
r = 2*M./(5.*t);
temp = 0;
    for k = 1:M-1
        theta_k = pi*k/M;
        s_theta_k = r*theta_k*(cot(theta_k)+j);
        sigma_theta_k = theta_k+(theta_k*cot(theta_k)-1)...
                        *cot(theta_k);
        temp = temp + real(exp(t.*s_theta_k).*F(s_theta_k)...
                *(1+j*sigma_theta_k));
    end
value = r./M.*(0.5*F(r).*exp(r.*t)+temp);
```

Appendix D

Poiseuille Flow in a Tube of Rectangular Cross Section

Consider an incompressible Newtonian liquid in an infinitely long tube of rectangular cross section of width $2w$ and height $2h$, as shown in Figure 2.1. Assume a steady pressure-driven flow in fully-developed situation which is governed by the Stokes equation,

$$\frac{\partial^2 u_z}{\partial x^2} + \frac{\partial^2 u_z}{\partial y^2} = \frac{1}{\mu}\frac{\partial p}{\partial z} \tag{D.1}$$

Due to the symmetry with respect to the planes $x = 0$ and $y = 0$, the flow can be modeled only in the first quadrant in $x - y$ plane. The boundary conditions are specified as follows:

$$\left.\begin{array}{lll} \frac{\partial u_z}{\partial x} = 0 & \text{on} & x = 0 \\ u_z = 0 & \text{on} & x = w \\ \frac{\partial u_z}{\partial y} = 0 & \text{on} & y = 0 \\ u_z = 0 & \text{on} & y = h \end{array}\right\} \tag{D.2}$$

Eq. (D.1) can be transformed into the Laplace equation by using

$$u_z(x, y) = -\frac{1}{2\mu}\frac{\partial p}{\partial z}\left(h^2 - y^2\right) + u_z'(x, y) \tag{D.3}$$

Note that the first term in the right-hand side of Eq. (D.3) is just the Poiseuille flow profile between two infinite plates placed at $y = \pm h$. Substituting Eq. (D.3) into Eqs. (D.1) and (D.2), we obtain

$$\frac{\partial^2 u_z'}{\partial x^2} + \frac{\partial^2 u_z'}{\partial y^2} = 0 \tag{D.4}$$

which is subject to the following boundary conditions:

$$\left.\begin{array}{lll} \dfrac{\partial u_z'}{\partial x} = 0 & \text{on} & x = 0 \\ u_z' = \dfrac{1}{2\mu}\dfrac{\partial p}{\partial z}\left(h^2 - y^2\right) & \text{on} & x = w \\ \dfrac{\partial u_z'}{\partial y} = 0 & \text{on} & y = 0 \\ u_z' = 0 & \text{on} & y = h \end{array}\right\} \tag{D.5}$$

Using the separation of variables method, we can solve Eq. (D.4) and obtain $u_z'(x, y)$. Substituting $u_z'(x, y)$ into Eq. (D.3) gives the final solution as:

$$u_z(x, y) = -\frac{h^2}{2\mu}\frac{\partial p}{\partial z}\left[1 - \left(\frac{y}{h}\right)^2 + 4\sum_{k=1}^{\infty}\frac{(-1)^k}{\alpha_k^3}\frac{\cosh\left(\dfrac{\alpha_k x}{h}\right)}{\cosh\left(\dfrac{\alpha_k w}{h}\right)}\cos\left(\frac{\alpha_k y}{h}\right)\right] \tag{D.6}$$

Appendix E

Publication List

Journal papers

1. **Yan, D.G.**, Yang, C., Nguyen, N.T., and Huang, X.Y. (2007), 'Diagnosis of Transient Electrokinetic Flow in Microflidic Channels', ***Phys. Fluids.***, Vol. 19, 017114(1-10).

2. **Yan, D.G.**, Yang, C., and Huang, X.Y. (2007), 'Effect of Finite Reservoir Size on Electroosmotic Flow in Microchannels', ***Microfluid. Nanofluid.***, Vol. 3, 333-340.

3. **Yan, D.G.**, Nguyen, N.T., Yang, C., and Huang, X.Y. (2006), 'Visualizing the transient electroosmotic flow and measuring the zeta potential of microchannels with a micro-PIV technique', ***J. Chem. Phys.***, Vol. 124, 021103(1-4).

4. **Yan, D.G.**, Yang, C., Nguyen, N.T., and Huang, X.Y. (2006), 'A method for simultaneously determining the zeta potentials of the channel surface and the tracer particles using microparticle image velocimetry technique', ***Electrophoresis***, Vol. 27, 620-627.

5. Tang, G.Y., **Yan, D.G.**, Yang, C., Gong, H.Q., Chai, J.C., and Lam, Y.C. (2006), 'Assessment of Joule heating and its effects on electroosmotic flow and electrophoretic transport of solutes in microfluidic channels', ***Electrophoresis***, Vol. 27, 628-639.

Conference papers

1. **Yan, D.G.**, Gan H.Y., Yang, C., Nguyen, N.T., Huang, X.Y., and Lam, Y.C. (2006), 'Use Micro-PIV to Measure Transient Electroosmotic Flow and Zeta Potential of Channel Wall', *The 10th International Conference on Miniaturized Systems for Chemistry and Life Sciences (μTAS2006)*, November 5-9, 2006, Tokyo, Japan, 89-91.

2. **Yan, D.G.**, Yang, C., Nguyen, N.T., and Huang, X.Y. (2006), 'Measurement of transient electrokinetic flow in microchannels using micro-PIV technique', *4th International Conference on Nanochannels, Microchannels and Minichannels*, June, 2006, Ireland.

3. **Yan, D.G.**, Yang, C., Nguyen, N.T., and Huang, X.Y. (2006), 'Diagnosis of time and frequency dependent electroosmotic flows in microfluidic channels', *ELKIN 2006 (International Electrokinetics Conference)*, June, 2006, France.

4. **Yan, D.G.**, Yang, C., Nguyen, N.T., and Huang, X.Y. (2006), 'Electrokinetic Flow in Microchannels with Finite Reservoir Size Effects', *International MEMS Conference 2006*, May, 2006, Singapore. Also published in: ***Journal of physics: Confrerence Series***, Vol. 34, 385-392.

5. Tang, G.Y., **Yan, D.G.**, Yang, C., Gong, H.Q., Chai, C., and Lam, Y.C. (2006), 'Joule heating and its effects on electroosmotic flow and electrokinetic transport of solutes in microfluidic channels', *Asia-Pacific Conference of Transducers and Micro-Nano Technology APCOT2006*, June, 2006, Singapore.

6. Tang, G.Y., Yang, C., **Yan, D.G.**, Gong, H.Q., Chai, C., and Lam, Y.C. (2006), 'Joule heating induced heat transfer in electrokinetic flow through microfluidic channels', *13th International Heat Transfer Conference*, August, 2006, Australia.

Bibliography

Abate, J. and Valko, P.P. (2004), 'Multi-precision Laplace transform inversion', *Int. J. Numer. Meth. Engng.*, Vol. 60, 979-993.

Aris, R. (1956), 'On the dispersion of a solute in a fluid flowing through a tube', *Proc. Roy. Soc. London Sect. A*, Vol. 235, 67-77.

Auroux, P.A., Iossifidis, D., Reyes, D.R., and Manz, A. (2002), 'Micro Total Analysis System. 2. Analytical Standard Operations and Applicatoins', *Anal. Chem.*, Vol. 74, 2637-2652.

Bazant, M.Z., Thornton, K., and Ajdari, A. (2004), 'Diffuse-charge dynamics in electrochemical systems', *Physical Review E*, Vol. 70, 021506(1-24).

Bhattacharyya, A., Masliyah, J.H., and Yang, J. (2003), 'Oscillating laminar electrokinetic flow in infinitely extended circular microchannels', *J. Colloid Interface Sci.*, Vol. 261, 12-20.

Biddiss, E., Erickson, D., and Li, D. (2004), 'Heterogeneous Surface Charge Enhanced Micromxing for Electrokinetic Flows', *Anal. Chem.*, Vol. 76, 3208-3213.

Brian, J.K. and Hasselbrink, E.F. (2004a), 'Zeta potential of microfluidic substrates: 1. Theory, experimental techniques, and effects on separations', *Electrophoresis*, Vol. 25, 187-202.

Brian, J.K. and Hasselbrink, E.F. (2004b), 'Zeta potential of microfluidic substrates: 2. Data for polymers', *Electrophoresis*, Vol. 25, 203-213.

Burgreen, D. and Nakache, F.R. (1964), 'Electrokinetic flow in ultrafine capillary slits', *J. Phys. Chem.*, Vol. 68, 1084-1091.

Chang, C.C. and Yang, R.J. (2004), 'Computational analysis of electrokinetically driven flow mixing in microchannels with patterned blocks', *J. Micromech. Microeng.*, Vol. 14, 550-558.

Chang, H.C. (2006), 'Electro-kinetics: a Viable Micro-fluidic Platform for Miniature Dagnostic Kits', *The Canadian Journal of Chemical Engineering*, Vol. 84, 1-15.

Chaudhury, M.K. and Whitesides, G.M. (1991), 'Direct measurement of interfacial interactions between semispherical lenses and flat sheets of poly (dimethylsiloxane) and their chemical derivatives', *Langmuir*, Vol. 7, 1013-1025.

Chen, C.H., Lin, H., Lele, S.K., and Santiago, J.G. (2005), 'Convective and absolute electrokinetic instability with conductivity gradient', *J. Fluid Mech.*, Vol. 524, 263-303.

Chen, H., Zhang, Y.T., Mezic, I., Meinhart, C.D., and Petzold, L.R. (2003), 'Numerical Simulation of an Electroosmotic Micromixer', *Proceedings of Microfluidics 2003 ASME IMECE*, Washington DC, November 2003.

Coleman, J.T. and Sinton, D. (2005), 'A sequential injection microfluidic mixing strategy', *Microfluid. Nanofluid.*, Vol. 1, 319-327.

Coleman, J.T., McKechnie, J., and Sinton, D. (2006), 'High-efficiency electrokinetic micromixing through symmetric sequential injection and expansion', *Lab Chip*, Vol. 6, 1033-1039.

COMSOL Multiphysics™ User's Guide (2006), product of COMSOL AB Inc., http://www.comsol.com

Crabtree, H.J., Cheong, E.C.S., Tilroe, D.A., and Backhouse, C.J. (2001), 'Microchip Injection and Separation Anolmlies Due to Pressure Effects', *Anal. Chem.*, Vol. 73, 4079-4086.

Cummings, E.B., Griffiths, S.K., Nealson, R.H., and Paul, P.H. (2000), 'Conditions for similitude between the fluid velocity and electric field in electroosmotic flow', *Anal. Chem.*, Vol. 72, 2526-2532.

Cussler, E.L. (1984), *Diffusion Mass Transfer in Fluid Systems*, Cambridge University Press, New York.

Debesset, S., Hayden, C.J., Dalton, C., Eijkel, J.C.T., and Manz, A. (2004), 'An AC electroosmotic micropump for circular chromatographic applications', *Lab Chip*, Vol. 4, 396-400.

Deen, W.M. (1998), *Analysis of Transport Phenomena*, Oxford University Press, New York.

Devasenathipathy, S. and Santiago, J.G. (2002), 'Particle tracking techniques for electrokinetic microchannel flows', *Anal. Chem.*, Vol. 74, 3704-3713.

Doetsch, G. and Nader, W. (1970), *Introduction to the Theory and Application of the Laplace Transformation*, Springer Verlag, New York.

Duffy, D.C., McDonald, C., Schueller, O.J.A., and Whitesides, G.M. (1998), 'Rapid prototyping of microfluidic systems in poly (dimethylsiloxane)', *Anal. Chem.*, Vol. 70, 4974-4984.

Dukhin, S.S., Zimmermann, R., and Werner, C. (2001), 'A concept for the generalization of the standard electrokinetic model', *Colloid and Surfaces A*, Vol. 195, 103-112.

Dutta, P. and Beskok, A. (2001), 'Analytical solution of time periodic electroosmotic flows: Analogies to Stokes' second problem', *Anal. Chem.*, Vol. 73, 5097-5102.

Einstein, A. (1905), *Theory of Brownian Movement*, Dover, New York.

Erickson, D., Li, D., and Werner, C. (2000), 'An Improved Method of Determining The -Potential and Surface Conductance', *J. Colloid Interface Sci.*, Vol. 232, 186-197.

Erickson, D. and Li, D. (2002), 'Influence of Surface Heterogeneity on Electrokinetically Driven Microfluidic Mixing', *Langmuir*, Vol. 18, 1883-1892.

Erickson, D. and Li, D. (2003), 'Analysis of alternating current electroosmotic flows in a rectangular channel', *Langmuir*, Vol. 19, 5421-5430.

Erickson, D., Sinton, D., and Li, D. (2003), 'Joule heating and heat transfer in poly (dimethylsiloxane) microfluidic sytems', *Lab Chip*, Vol. 3, 141-149.

Erickson, D. and Li, D. (2004), 'Integrated microfluidic devices', *Analytica Chimica Acta*, Vol. 507, 11-26.

Fan, Z.H. and Harrison, J.D. (1994), 'Micromachining of capillary electrophoresis injectors and separators on glass chips and evaluation of flow at capillary intersections', *Anal. Chem.*, Vol. 66, 177-184.

Fu, L.M., Yang, R.J., Lin, C.H., and Chien, Y.S. (2005), 'A novel microfluidic mixer utilizing electrokinetic driving forces under low switching frequency', *Electrophoresis*, Vol. 26, 1814-1824.

Gaš, B. (1997), 'Peak broadening in capillary zone electrophoresis', *Electrophoresis*, Vol. 18, 2123-2133.

Gaš, B. and Kenndler, E. (2002), 'Peak broadening in microchip electrophoresis: a discussion of the theoretical background', *Electrophoresis*, Vol. 23, 3817-3826.

Ghosal, S. (2006), 'Electrokinetic Flow and Dispersion in Capillary Electrophoresis', *Annual Review of Fluid Mechanics*, Vol. 38, 309-338.

Glasgow, I., Batton, J., and Aubry, N. (2004), 'Electroosmotic mixing in microchannels', *Lab Chip*, Vol. 4, 558-562.

Gu, Y. and Li, D. (2000), 'The zeta-potential of glass surface in contact with aqueous solutions', *J. Colloid Interface Sci.*, Vol. 226, 328-339.

Gunning, J., Chan, Y.C., and White, L.R. (1995), 'The Impedance of the Planar Diffuse Double Layer: An Exact Low-Frequency Theory', *J. Colloid Interface Sci.*, Vol. 170, 522-537.

Gravesen, P., Branebjerg, J., and Jensen, O.S. (1993), 'Microfluidics – a review', *J. Micromech. Microeng.*, Vol. 3, 168-182.

Hanna, W.T. and Osterle, J.F. (1968), 'Transient Electro-osmosis in Capillary Tubes', *J. Chem. Phys.*, Vol. 49, 4062.

Ho, C.M. and Tai, Y.C. (1998), 'Micro-electro-mechanical-systems (MEMS) and fluid flows', *Annu. Rev. Fluid Mech.*, Vol. 30, 579-612.

Huang, P. and Breuer, K.S. (2003), 'Performance and Scaling of an Electro-osmotic Mixer', *The 12th International Conference on Solid State Sensors, Actuators and Microsystems*, Boston, June 8-12, 2003.

Huang, X., Gordon, M.J., and Zare, R.N. (1988), 'Current-Monitoring Method for Measuring the Electroosmotic Flow Rate in Capillary Zone Electrophoresis', *Anal. Chem.*, Vol. 60, 1837.

Hunter, R.J. (1981), *Zeta Potential in Colloid Science*, Academic Press, London.

Ivory, C.F. (1983), 'Transient Electroosmosis: the Momentum Transfer Coefficient', *J. Colloid Interface Sci.*, Vol. 96, 296-298.

Jacobson, S.C., Hergenröder, R., and Koutny, L.B. (1994), 'High-speed separations on a microchip', *Anal. Chem.*, Vol. 66, 1114-1118.

Jacobson, S.C., Culbertson, C.T., Daler, J.E., and Ramsey, J.M. (1998), 'Microchip structures for submillisecond electrophoresis', *Anal. Chem.*, Vol. 70, 3476-3480.

Jacobson, S.C., McKnight, T.E., and Ramsey, J.M. (1999), 'Microfluidic Devices for Electrokinetically Driven Parallel and Serial Mixing', *Anal. Chem.*, Vol. 71, 4455-4459.

Jeon, N.L., Dertinger, K.W., Chiu, D.T., Choi, I.S., Stroock, A.D., and Witersiedes, G.M. (2000), 'Generation of solution and surface gradients using microfluidic systems', *Langmuir*, Vol. 16, 8311-8316.

Johnson, T.J., Ross, D., and Locascio, L.E. (2002), 'Rapid Microfluidic Mixing', *Anal. Chem.*, Vol. 74, 45-51.

Kang, Y.J., Yang, C., and Huang, X.Y. (2002), 'Dynamic aspects of electroosmotic flow in a cylindrical microcapillary', *Int. J. Eng. Sci.*, Vol. 40, 2203-2221.

Kang, Y.J., Yang, C., and Huang, X.Y. (2004), 'AC electroosmosis in microchannels packed with a porous medium', *J. Micromech. Microeng.*, Vol. 14, 1249-1257.

Keh, H.J. and Anderson, J.C. (1985), 'Boundary effects on electrophoretic motion of colloidal spheres', *J. Fluid Mech.*, Vol. 153, 417-439.

Keh, H.J. and Tseng, H.C. (2001), 'Transient Electrokinetic Flow in Fine Capillaries', *J. Colloid Interface Sci.*, Vol. 242, 450-459.

Kim, M.J., Beskok, A., and Kihm, K.D. (2002), 'Electro-osmosis-driven microchannel flows: A comparative study of microscopic particle image velocimetry measurements and numerical simulations', *Exp Fluids*, Vol. 33, 170-180.

Kim, M.J. and Kihm, K.D. (2004), 'Microscopic PIV Measurements for Electroosmotic Flows in PDMS Microchannels', *J. Visualization*, Vol. 7, 111-118.

Lammertink, R.G.H., Schlautmann, S., Besselink, G.A.J., and Schasfoort, R.B.M. (2004), 'Recirculation of Nanoliter Volumes within Microfluidic Channels', *Anal. Chem.*, Vol. 76, 3018-3022.

Lastochkin, D., Zhou, R., Wang, P., Ben, Y., and Chang, H.C. (2004), 'Electrokinetic micropump and micromixer design based on ac fradaic polarization', *J. App. Phys.*, Vol. 96, 1730-1733.

Lee, C.Y., Lee, G.B., Fu, L.M., Lee, K.H., and Yang, R.J. (2004), 'Electrokinetically driven active micro-mixers utilizing zeta potential variation induced by field effect', *J. Micromech. Microeng.*, Vol. 14, 1390-1398.

Li, D. (2004), *Electrokinetics in Microfluidics*, Academic Press, Toronto.

Lin, C.H., Fu, L.M., and Chien, Y.S. (2004), 'Microfluidic T-Form Mixer Utilizing Switching Electroosmotic Flow', *Anal. Chem.*, Vol. 76, 5265-5272.

Lin, H., Storey, B.D., Oddy, M.H., Chen, C.H., and Santiago, J.G. (2004), 'Instability of electrokinetic microchannel flows with conductivity gradients', *Phys. Fluids*, Vol. 16, 1922-1935.

MacInnes, J.M. (2002), 'Computation of reacting electrokinetic flow in microchannel geometries', *Chemical Engineering Science.*, Vol. 57, 4539-4558.

MacInnes, J.M., Du, X., and Allen, R.W.K. (2003), 'Prediction of electrokinetic and pressure flow in a microchannel T-junction', *Phys. Fluids.*, Vol. 15, 1992-2005.

Marcos, Yang, C., Wong, T.N., and Ooi, K.T. (2004a), 'Dynamic aspects of electroosmotic flow in rectangular micorchannels', *Int. J. Eng. Sci.*, Vol. 42, 1459-1481.

Marcos, Yang, C., Ooi, K.T., Wong, T.N., and Masliyah, J.H. (2004b), 'Frequency-dependent laminar electroosmotic flow in a closed-end rectangular microchannel', *J. Colloid Inerface Sci.*, Vol. 275, 679-698.

Marcos, Ooi, K.T., Yang, C., Chai, J.C., and Wong, T.N. (2005), 'Developing electroosmotic flow in closed-end micro-channels', *Int. J. Eng. Sci.*, Vol. 43, 1349-1362.

Masliyah, J.H. (1994), *Electrokinetic Transport Phenomena*, AOSTRA Technical Publication Series No. 12, AOSTRA, Edmonton.

Meinhart, C.D. and Zhang, H. (2000), 'The Flow Structure Inside a Microfabricated Inkjet Printhead', *J. Microelectromech. Syst.*, Vol. 9, 67-75.

Meinhart, C.D., Wereley, S.T., and Santiago, J.G. (2000), 'A PIV Algorithm for Estimating Time-Averaged Velocity Fields', *J. Fluids Eng.*, Vol. 122, 285-289.

Meinhart, C.D., Wang, D., and Turner, K. (2003), 'Measurement of AC electrokinetic Flows', *Biomedical Microdevices*, Vol. 5:2, 139-145.

Minor, M., van der Linder, A.J., van Leeuwen, H.P., and Lyklema, J. (1997), 'Dynamic aspects of electrophoresis and electroosmosis: a new fast method for measuring particle mobilities', *J. Colloid Interface Sci.*, Vol. 189, 370-375.

Mishchuk, N.A. and Gonzalez-Caballero, F. (2006a), 'Nonstationary electroosmotic flow in open cylindrical capillaries', *Electrophoresis*, Vol. 27, 650-660.

Mishchuk, N.A. and Gonzalez-Caballero, F. (2006b), 'Nonstationary electroosmotic flow in closed cylindrical capillaries', *Electrophoresis*, Vol. 27, 661-671.

Moctar, A.O.E., Aubry, N., and Batton, J. (2003), 'Electro-hydrodynamic microfluidic mixer', *Lab Chip*, Vol. 3, 273-280.

Morgan, H. and Green, N.G. (2003), *AC electrokinetics: colloids and nanoparticles*, Research Studies Press, England.

Ng, A.S.W., Hau, W.L.W., Lee, Y.K., and Zohar, Y. (2004), 'Electrokinetic generation of microvortex patterns in a microchannel liquid flow', *J. Micromech. Microeng.*, Vol. 14, 247-255.

Nguyen, N.T. and Huang, X.Y. (2005), 'Mixing in microchannels based on hydrodynamic focusing and time-interleaved segmentation: modeling and experiment', *Lab Chip*, Vol. 5, 1320-1326.

Nguyen, N.T. and Wereley, S.T. (2002), *Fundamentals of Microfluidics*, Boston, London: Artech House.

Nguyen, N.T. and Wu, Z. (2005), 'Micromixers – a review', *J. Micromech. Microeng.*, Vol. 15, R1-R16.

Oddy, M.H., Santiago, J.G., and Mikkelsen, J.C. (2001), 'Electrokinetic Instability Mciromixing', *Anal. Chem.*, Vol. 73, 5822-5832.

Oddy, M.H. and Santiago, J.G. (2003), 'A method for determining electrophoretic and electroosmotic mobilities using AC and DC electric field particle displacements', *J. Colloid Interface Sci.*, Vol. 269, 192-204.

Ohshima, H. (1994), 'A Simple Expression for Henry's Function for the Retardation Effect in Electrophoresis of Spherical Colloidal Particles', *J. Colloid Inerface Sci.*, Vol. 168, 269-271.

Oka, K. and Furusawa, K. (1998), in: Ohshima, H., Furusawa, K. (Eds.), *Electrical Phenomena at Interfaces*, Marcel Dekker, New York.

Ottino, J.M. and Wiggins, S. (2004), 'Introduction: mixing in microfluidics', *Phil. Trans. R. Soc. Lond. A.*, Vol. 362, 923-935.

Ozisik, M.N. (1993), *Heat Conduction*, 2nd Edn., Wiley, New York.

Papanastasiou, T.C., Georgiou, G.C., and Alexandrou, A.N. (2000), *Viscous Fluid Flow*, CRC Press, Boca Raton.

Probstein, R.F. (1994), *Physicochemical Hydrodynamics*, 2nd ed., Butterworths, Boston.

Qian, S. and Bau, H.H. (2002), 'A Chaotic Electroosmotic Stirrer', *Anal. Chem.*, Vol. 74, 3616-3625.

Rani, S.A., Pitts, B., and Stewart, P.S. (2005), 'Rapid Diffusion of Fluorescent Tracers into Staphylococcus epidermidis Biofilms Visualized by Time Lapse Microscopy', *Antimicrob Agents Chemother*, Vol. 49, 728-732.

Ren, X., Bachman, M., Sims, C., Li, G.P., and Allbritton, N. (2001), 'Electroosmotic properties of microfluidic channels composed of poly(dimethylsiloxane)', *Journal of Chromatography B*, Vol. 762, 117-125.

Reppert, P.M. and Morgan, F.D. (2002), 'Frequency-dependent electroosmosis', *J. Colloid Interface Sci.*, Vol. 254, 372-383.

Reppert, P.M. and Khan, T. (2005), 'A finite element formulation of frequency-dependent electroosmosis', *J. Colloid Interface Sci.*, Vol. 290, 574-581.

Reyes, D.R., Iossifidis, D., Auroux, P.A., and Manz, A. (2002), 'Micro Total Analysis System. 1. Introduction, Theory, and Technology', *Anal. Chem.*, Vol. 74, 2623-2636.

Rice, C.L. and Whitehead, R. (1965), 'Electrokinetic flow in narrow cylindrical capillaries', *J. Phys. Chem.*, Vol. 69, 4017-4023.

Ronald, L.A. and Duncan, W.M. (2004), *Signal Analysis: TIME, FREQUENCY, SCALE, AND STRUCTURE*, John Wiley & Sons Inc., New York.

Ross, D., Gaitan, M., and Locascio, L.E. (2001), 'Temperature measurement in microfluidic systems using a temperature-dependent fluorescent dye', *Anal. Chem.*, Vol. 73, 4117-4123.

Russel, W.B., Saville, D.A., and Schowalter, W.R. (1999), *Colloidal Dispersions*, Cambridge University Press.

Sadr, R., Yoda, M., Zheng, Z., and Conlisk A.T. (2004), 'Electro-osmotic flow in two-dimensional charged micro- and nanochannels', *J. Fluid Mech.*, Vol. 506, 357-367.

Santiago. J.G., Wereley, S.T., Meinhart, C.D., Beebe, D.J., and Adrian, R.J. (1998), 'A particle image velocimetry system for microfluidics', *Exp. Fluids*, Vol. 25, 316-325.

Santiago, J.G. (2001), 'Electroosmotic flows in microchannels with finite inertial and pressure forces', *Anal. Chem.*, Vol. 73, 2353-2365.

Shaw, D.J. (1980), *Introduction to Colloid and Surface Chemistry*, 3rd ed., Butterworths, London.

Söderman, O. and Jonsson, B. (1996), 'Electro-osmosis: Velocity profiles in different geometries with both temporal and spatial resolution', *J. Chem. Phys.*, Vol. 105, 10300-10311.

Stone, H.A., Stroock, A.D., and Ajdari, A. (2004), 'Engineering flows in small devices: microfluidics toward a Lab-on-a-Chip', *Annu. Rev. Fluid Mech.*, Vol. 36, 381-411.

Strook, A.D., Dertinger, S.K.W., Ajdary, A., Mezic, I., Stone, H.A., and Whitesides, G.M. (2002), 'Chaotic Mixer for Microchannels', *Science*, Vol. 295, 647-651.

Sundaram, N. and Tafti, D.K. (2004), 'Evaluation of Microchamber Geometries and Surface Conditions for Electrokinetic Driven Mixing', *Anal. Chem.*, Vol. 76, 3785-3793.

Suresh, V. and Homsy, G.M. (2004), 'Stability of time-modulated electroosmotic flow', *Phys. Fluids*, Vol. 16, 2349-2356.

Tang, G.Y., Yang, C., Chai, J.C., and Gong, H.Q. (2003), 'Modeling of electroosmotic flow and capillary electrophoresis with the Joule heating effect: the Nernst-Plank equation versus Boltzmann distribution', *Langmuir*, Vol. 19, 10975-10984.

Tang, Z.L., Hong, S., Djukic, D., Modi, V., West, A.C., Yardley, J., and Osgood, R.M. (2002), 'Electrokinetic flow control for composition modulation in a microchannel', *J. Micromech. Microeng.*, Vol. 12, 870-877.

Taylor, G.I. (1953), 'Dispersion of soluble matter in solvent flowing slowly through a tube', *Proc. Roy. Soc. London Sect. A*, Vol. 219, 186-203.

Taylor, J.A. and Yeung, E.S. (1993), 'Imaging of Hydrodynamic and Electrokinetic Flow Profiles in Capillaries', *Anal. Chem.*, Vol. 65, 2928-2932.

Telionis, D.P. (1981), *Unsteady Viscous Flow*, Springer-Verlag, New York.

Tikhomolova, K.P. (1993), *Electro-Osmosis*, Ellis Horwood, New York.

Unni, H.N. and Yang, C. (2005), 'Brownian dynamic simulation and experimental study of colloid particle deposition in a microchannel flow', *J. Colloid Interface Sci.*, Vol. 291, 28-36.

Wang, D., Sigurdson, M., and Meinhart, C.D. (2005), 'Experimental analysis of particle and fluid motion in ac electrokinetics', *Exp. Fluids*, Vol. 38, 1-10.

Wang, S.C., Lai, Y.W., Ben, Y., and Chang, H.C. (2004), 'Microfluidic Mixing by dc and ac Nonlinear Electrokinetic Vortex Flows', *Ind. Eng. Chem. Res.*, Vol. 43, 2902-2911.

Wereley, S.T., Gui, L., and Meinhart, C.D. (2002), 'Advanced algorithms for microscale particle image velocimetry', *AIAA Journal.*, Vol. 40, 1047-1055.

Whitesides, G.M. (2006), 'The origins and the future of microfluidics', *Nature*, Vol. 442, 368-373.

Xuan, X.Y. and Li, D. (2005), 'Electroosmotic flow in microchannels with arbitrary geometry and arbitrary distribution of wall charge', *J. Colloid Interface Sci.*, Vol. 289, 291-303.

Yang, C., Li, D., and Masliyah, J.H. (1998), 'Modeling forced liquid convection in rectangular microchannels with electrokinetic effects', *Int. J. Heat Mass Transfer*, Vol. 41, 4229-4249.

Yang, C. (2002), *in Microfluidics and BioMEMS*, edited by F. Tay, Kluwer, Academic, Boston.

Yang, C., Ng, C.B., and Chan, V. (2002), 'Transient Analysis of Electroosmotic Flow in a Slit Microchannel', *J. Colloid Interface Sci.*, Vol. 248, 524-527.

Yang R.J., Tseng, T.I., and Chang, C.C. (2005), 'End effects on electro-osmotic flows in microchannels', *J. Micromech. Microeng.*, Vol. 15, 254-262.

Yang, J., Bhattacharyya, A., Masliyah, J.H., and Kwok, D.Y. (2003), 'Oscillating laminar electrokinetic flow in infinitely extended rectangular microchannels', *J. Colloid Interface Sci.*, Vol. 261, 21-31.

Yariv, E., Brenner, H., and Kim, S. (2004), 'Curvature-induced Dispersion in Electro-osmotic Serpentine Flows', *SIAM J. APPL. MATH.*, Vol. 64, 1099-1124.

Zhang, Y., Gu, X.J., Barber, R.W., and Emerson D.R. (2004), 'An analysis of induced pressure fields in electroosmotic flows through micorchannels', *J. Colloid Interface Sci.*, Vol. 275, 670-678.

Zhang, Y.T., Follman, D., Chen, H., Mezic, I., Meinhart, C.D., Petzold, L.R., and MacDonald N.C. (2003), 'Design and Fabrication of a Ring Electrokinetic Chaotic Micromixer (RECM) with Intergrated Electrodes', *Proceedings of Microfluidics 2003 ASME IMECE*, Washington DC, November 2003.